Research Article

Planck On-Ground Attitude Estimation Algorithms

Mark Tuttlebee
VCS AG at ESA/ESOC, Robert-Bosch-Str. 5, 64293 Darmstadt, Germany
mark.tuttlebee@esa.int

Gottlob Gienger
ESA/ESOC, Robert-Bosch-Str. 5, 64293 Darmstadt, Germany
gottlob.gienger@esa.int
Submitting author

Abstract

On-ground attitude processing algorithms for the Planck mission are treated comprehensively. From attitude telemetry, ESA Flight Dynamics provides daily attitude history files to the Planck data processing centres to reconstruct the inertial pointing of all bolometers as they sweep the sky. The baseline ground-processing algorithm solely uses star tracker attitude telemetry. Post-launch experience and refined requirements lead to four improved attitude estimation algorithms:

1. Use Planck's fibre optic gyro package as spacecraft dynamic model replacement.
2. Use a dynamic model to filter star tracker attitude during routine slews and to estimate thruster pulse torques.
3. Use rigid body dynamic model to filter star tracker attitude during scientific pointings.
4. Use rigid body dynamic model with slowly varying inertia tensor. Estimate the spacecraft inertia tensor with a sufficient level of nutation.

Capabilities and estimation accuracy all algorithms are validated with a high-precision simulator and in-flight attitude telemetry. Better estimation algorithms result in more accurate CMB maps.

Notation and Conventions

Following [1], we adopt the following notation and conventions for vectors and quaternions. A 3-vector, $\underline{v}$, is defined as:-

$$\underline{v} = \begin{bmatrix} v_1 \\ v_2 \\ v_3 \end{bmatrix}$$

A quaternion, $\underset{\sim}{q}$, and it's complex conjugate (inverse) are defined as:-

$$\underset{\sim}{q} = \begin{bmatrix} \underline{q} \\ q_4 \end{bmatrix} = \begin{bmatrix} q_1 \\ q_2 \\ q_3 \\ q_4 \end{bmatrix}, \quad \underset{\sim}{q}^{-1} = \begin{bmatrix} -\underline{q} \\ q_4 \end{bmatrix} = \begin{bmatrix} -q_1 \\ -q_2 \\ -q_3 \\ q_4 \end{bmatrix}$$

where the quaternion satisfies the norm constraint:-

$$q_1^2 + q_2^2 + q_3^2 + q_4^2 = 1$$

A 3-vector, $\underline{v}$, expressed as a quaternion is defined as:-

$$\underset{\sim}{v} = \begin{bmatrix} \underline{v} \\ 0 \end{bmatrix} = \begin{bmatrix} v_1 \\ v_2 \\ v_3 \\ 0 \end{bmatrix}$$

Quaternion multiplication can be expressed as matrix-vector multiplication as follows:-

$$\underset{\sim}{p} \otimes \underset{\sim}{q} = [\underset{\sim}{p}]_L \underset{\sim}{q} = [\underset{\sim}{q}]_R \underset{\sim}{p}$$

where

$$[\underset{\sim}{q}]_L = \begin{bmatrix} q_4 & q_3 & -q_2 & q_1 \\ -q_3 & q_4 & q_1 & q_2 \\ q_2 & -q_1 & q_4 & q_3 \\ -q_1 & -q_2 & -q_3 & q_4 \end{bmatrix}, [\underset{\sim}{q}]_R = \begin{bmatrix} q_4 & -q_3 & q_2 & q_1 \\ q_3 & q_4 & -q_1 & q_2 \\ -q_2 & q_1 & q_4 & q_3 \\ -q_1 & -q_2 & -q_3 & q_4 \end{bmatrix}$$

The vector product of two 3-vectors is given by:-

$$\underline{p} \wedge \underline{q} = -[[\underline{p}]]\underline{q} = [[\underline{q}]]\underline{p}$$

where

$$[[\underline{q}]] = \begin{bmatrix} 0 & q_3 & -q_2 \\ -q_3 & 0 & q_1 \\ q_2 & -q_1 & 0 \end{bmatrix}$$

The $\Omega(\underline{v})$ and $\Theta(\underline{\tilde{q}})$ that arise from the quaternion multiplication operation are given by:-

$$\Omega(\underline{v}) = \begin{bmatrix} 0 & v_3 & -v_2 & v_1 \\ -v_3 & 0 & v_1 & v_2 \\ v_2 & -v_1 & 0 & v_3 \\ -v_1 & -v_2 & -v_3 & 0 \end{bmatrix}, \Theta(\underline{\tilde{q}}) = \begin{bmatrix} q_4 & -q_3 & q_2 \\ q_3 & q_4 & -q_1 \\ -q_2 & q_1 & q_4 \\ -q_1 & -q_2 & -q_3 \end{bmatrix}.$$

1 Introduction

On 14 May 2009 the European Space Agency launched two space observatories: Herschel (with a 3.5 m mirror it is the largest space telescope ever) and the cosmic microwave survey mission Planck [2]. [3] describes the history and main performance elements of the Planck satellite during its first year of life.

The Planck Mission Operations Centre resides at ESA's European Space Operations Centre ESOC at Darmstadt, Germany; it includes the Planck Flight Dynamics System [4]. From Planck attitude telemetry, Flight Dynamics provides daily raw and reconstructed attitude history files (AHF) to the Planck Science Office based at the European Astronomy Centre at Villafranca, Spain, and to and the Planck HFI and LFI data processing centres, containing the inertial attitudes of the spacecraft attitude control axes frame with a frequency of 4 Hz or 8 Hz. The data processing centres use these AHFs to reconstruct the inertial direction of each of the 36 HFI radio receiver feed horns and of the 11 LFI bolometer feed horns at each time instance, from which the all-sky scan maps are build. The LFI and HFI instrument data processing is described in [5], [6]. The quality of the reconstructed AHFs therefore directly influences the quality of the reconstructed scan maps.

The baseline ground-processing algorithm (Algorithm#0) essentially consists of a star tracker dynamic model based filter using frequency domain methods. It was developed and validated by Sener 2003-2006 [7], [8]. The behaviour of the Planck attitude and orbit control system in commissioning phase is described [9]. Post-launch experience and refined requirements lead to several improved attitude filtering resp. estimation algorithms.

This article documents the work to provide and assess new star tracker attitude quaternion measurement filtering algorithms. All filters use a batch least squares approach, since this is a postprocessing task for regular daily intervals. In contrast, for the Wilkinson Microwave Anisotropy Probe WMAP and many other projects, pointing and beam determination is done with Kalman filters [10].

Also provided are the results of a complete end-to-end validation of the current filtering algorithm, used within the AHF generation software, with the aid of the Planck High Precision Test Data Generator (HPTDG). The new filters that do not use the fibre optic gyro measurements have also been assessed using the HPTDG.

Chapter 2 gives a high level description of the current baseline algorithms and processing used to support the Planck mission. Also referenced are related star tracker attitude data processing algorithms, that are used to estimate the spacecraft inertia tensor. Also presented is a formulation of the prediction and measurement models for the new filtering algorithms, which are listed as follows:-

- Algorithm#1 was the initial motivation for the work and consists of using data from the fibre optic gyro package as a spacecraft dynamic model replacement. This estimator can be used to filter star tracker attitude quaternion data when the spacecraft is performing nominal reorientation slews in HCM and stable pointings in SCM.
- Algorithm#2 makes use of a dynamic model, that can be used to filter star tracker attitude quaternion data when the spacecraft is performing nominal reorientation slews in HCM. Also estimated are the thruster torques from the 3 pulses that are commanded in order to carry out the slew manoeuvre.
- Algorithm#3 makes use of a dynamic model of the spacecraft, which is assumed to be a rigid body. This dynamic model has also been extended to account for effects observed on the X-axis rotational motion, which are known to be due to internal disturbances caused by the Sorption cooler. This estimator can be used to filter star tracker attitude quaternion data during pointings in SCM.
- Algorithm#4 uses a dynamic model of the spacecraft, which is assumed to be a rigid body with a slowly varying inertia tensor. This estimator can be used to estimate the spacecraft inertia tensor during actuation free periods in OCM where a sufficient level of nutation is present.

Chapter 3 provides a high level description of the Planck HPTDG test environment, which was used to generate simulated real world kinematics and dynamics, together with realistic ACMS telemetry [11]. These data were used to perform a complete end-to-end test of the current AHF generation estimation algorithm and the new SCM mode STR-dynamic model based estimation algorithm. The commands used to run the simulation were generated from a complete set of ACMS command parameter files for OD 0390. In addition, the sensitivity of the current estimator and the new SCM mode STR-dynamic model based estimator, to various types of time varying STR alignment errors is also presented. A validation of the HCM nominal reorientation slew mode STR-Dynamic model based estimator has also been performed. Finally, the dynamic model based estimation algorithm, used to estimate the complete inertia tensor was also tested, the results of which are compared with actual values simulated within the HPTDG dynamic model and the estimation results achieved using the current spacecraft inertia ten-

sor estimation algorithm.

Chapter 4 presents the results obtained using in-flight sensor data, together with a comparison between the current filter and the two new filters. This has been done for single pointings in science mode before and after the updates to the thermal controller were made, in order to show the positive effect that this has brought to attitude reconstruction. After the thermal controller updates, agreement between the current filter and the new filters is very good, including the STR-dynamic model based filter, which also accounts for X-axis disturbances resulting from internal torques created by the Sorption cooler. In terms of auxiliary results such as disturbance torque and nutation angle estimation, the results are comparable between all filters. Also shown are the results of frequency analyses, of star tracker and fibre optic gyro measurement data, which will be used to identify actual effects that affect the spacecraft dynamics and other effects that are the result of thermoelastic distortions that disturb the mounting of the star tracker and fibre optic gyro package. These frequency analyses were performed using data taken from a long pointing (> 2 days) during ODs 0077 to 0079 in the CPV phase, which was prior to updates of the thermal controller. Also provided for comparison, is an analysis of data taken from a long pointing (~8 hours) after the thermal controller updates. Also presented are the results of current algorithm and new dynamic model based algorithm, used to estimate the spacecraft inertia tensor, which also show good agreement. Finally, some results are presented to show how the filters perform when used to filter star tracker attitude quaternion data taken during a period where a nominal reorientation slew in HCM has been commanded.

Chapter 5 presents the conclusions of this work, which summarises clearly the advantages and disadvantages and capabilities of each estimator.

2 Attitude Data Processing Algorithms

This chapter gives an overview of current algorithms used to filter star tracker attitude quaternion data, which form part of the current attitude history file (AHF) generation software. A complete description of the AHF contents and their interpretation can be found in [12]. In addition, algorithms to perform periodic calibrations of the spacecraft inertia tensor are also described.

Also presented is a formulation of new estimation algorithms, that are used to filter star tracker attitude quaternion measurements and estimate the spacecraft inertia tensor. The first of these new algorithms uses the fibre optic gyro (FOG) angular rate measurements as a dynamic model replacement and the second uses a spacecraft dynamic model, assumed to be a rigid body including a model of the sorption cooler internal disturbance torques.

2.1 Star Tracker Attitude Quaternion Filter

This section contains a brief outline of the current estimation algorithm used within the operational AHF generation software. This is well documented in Chapter 5 of [8] and so only a high level description of the steps involved, including some new additional features and details where applicable, will be given here in order to show the various assumptions that have been made in deriving this algorithm.

1. Compute sequence of raw angular velocities in body axes and corresponding time stamps from the measured STR quaternions and associated on-board time labels. The alignment quaternion is used to refer the star tracker reference frame to the spacecraft body reference frame.
2. Convert the inertial to body transformation represented as a quaternion into a DCM.
3. The raw angular momentum vector in the spacecraft body reference system together with their on-board time labels are first computed using the spacecraft body angular rates and an assumed value of the spacecraft inertia tensor. This raw body angular momentum vector is then transformed into the inertial reference system using the inertial to body transformations (DCMs) computed in step 2.
4. Assuming that the external torques expressed in the inertial reference system are constant, perform a linear least squares fit to the inertial angular momentum vectors computed previously in step 3, to compute the inertial angular momentum vector at the time sequence origin together with the slope, which gives a measure of the external torques expressed in the inertial reference system.
5. Using the previously obtained linear law for the inertial angular momentum vector, evaluate the linear fit at the quaternion measurement on-board time labels and compute a (3-2-1) Euler angle sequence, that can be used to construct a DCM that transforms from, the inertial reference system to a rotating angular momentum reference system, also taking into account that the spacecraft spin rate increases as a result of the application of external environmental disturbance torques. The speed of rotation of this rotating system is at the inertial nutation rate.
6. Solve for by least squares, the parameters of a model for the spacecraft body transverse axes angular rates. These parameters account for the offset and drift of the principal X-axis with respect to the spacecraft body X-axis. In addition, it also takes into account any residual nutation based on an assumed pre-estimated value of the nutation to spin rate ratio.
7. Using only the model parameters that account for the offset and drift of the principal X-axis with respect to the spacecraft body X-axis, evaluate the model of the spacecraft transverse body axes angular rates, at the quaternion measurement on-board time labels. In addition, perform a linear least squares fit to the body x-axis angular rate. Then using this, compute a (3-2-1) sequence of Euler angles, that can be used to construct a DCM that transforms from the spacecraft body reference system to a rotating pseudo-principal axis reference system. The speed of rotation of this pseudo-principal axis reference system is at the body nutation rate.
8. Combine the DCMs computed in steps 2, 5 and 7 above to compute the transformation from the rotating angular momentum reference system to the pseudo-principal axis reference system and convert this DCM to a quaternion. The components of this quaternion are processed to ensure that they are continuous without any wrap around.
9. Compute a 5^{th} order[1] polynomial required to detrend the components of the previously computed quaternion.

10. Compute the DFT of the components of the previously detrended quaternion and cut the high frequency components greater than a user selectable cut-off frequency[2] and then perform the Inverse DFT of the resulting truncated frequency spectrum.
11. Reconstruct the filtered rotating angular momentum reference system to pseudo-principal axis reference system quaternion transformation by adding back in the detrending polynomial computed in step 9.
12. Convert the quaternion in step 11 to a DCM and combine this with the DCMs computed in steps 5 and 7 above, to compute the filtered inertial to body transformation matrix (DCM). Convert the resulting DCM back to a quaternion.

2.2 Spacecraft Inertia Tensor Calibration

The current spacecraft inertia tensor estimation algorithm is described in Section 3.3.9 (FCP-P-D-MAINT procedure) of [13]. An alternative derivation is presented in Appendix A.

2.3 STR/FOG Inter-calibration

When FOG angular rate measurements are used as a spacecraft dynamic model replacement, it is necessary to have the best possible a priori estimate of the transfer function parameters, that relate the FOG angular rate measurements to the angular rates derived from the STR quaternion measurements at 8 Hz in SCM and 4 Hz in OCM. The calibration algorithm formulation is documented in Chapter 2 of [14]. The analysis and performance assessment of the algorithm is presented in Chapter 3 of [14].

2.4 Fibre Optic Gyro Based Estimation Algorithm

The following section presents the state prediction and measurement models, that are used within a batch least squares algorithm. This algorithm is used to estimate the state vector at a specified epoch by processing all the star tracker measurements, rejecting outliers based on thresholds computed using the statistics of the observation residuals. The general implementation of the batch least squares algorithm implementation is described in Appendix C.

This algorithm will be used to filter STR attitude quaternion data during nominal reorientation slews in HCM as well as data during stable pointing phases in SCM.

2.4.1 State Prediction Model

The state prediction model uses a model of the spacecraft kinematics together with a measurement of the spacecraft body angular rates provided by processing the measured FOG angular rate data. Referring to Section 2.2 of [14] the spacecraft body angular rates can be computed using the following equation:-

$$\underline{\omega}_B \;=\; T_{GB}^{+}(I_4 + \Delta K)^{-1}(\underline{\omega}_G - \underline{b}_G) - \underline{b} - \underline{\eta} \;=\; \underline{\omega}_B{}' - \underline{b} - \underline{\eta} \tag{1}$$

where the following parameters were estimated by processing data taken during the large Delta-V manoeuvre performed in OD 0035.

ΔK is the gyro scale factor error matrix of dimension 4×4

T_{GB} is the body-to-gyro sensitive axis transformation matrix of dimension 4×3

T_{GB}^{+} is the pseudo-inverse of T_{GB} of dimension 3×4

$\underline{b}_G$ is the gyro rate biases 4-vector

and

1. During LEOP and Commissioning it was found that the linear detrending suggested in [8] was insufficient to cover the trends that were observed during long pointings
2. Set to 0.03 Hz as recommended by industry

$\underline{\omega}_B$ is the true angular rate vector expressed in spacecraft body axes

$\underline{\omega}_G$ is the measured angular rate 4-vector along gyro sensitive axes

$\underline{\omega}_B'$ is the FOG derived angular rate vector expressed in spacecraft body axes

$\underline{b}$ is the residual gyro rate bias vector expressed in spacecraft body reference system

$\underline{\eta}$ is the angular rate measurement noise vector expressed in the spacecraft body reference system. Assumed zero mean and Gaussian.

In order to account for FOG residual rate biases, the constant 3-vector $\underline{b}$ is included within the state vector to be estimated. Also, effects due to uncertainties in the components of the FOG transfer function, (residual scale factor and misalignment errors), are accounted for by including the constant 3-vector $\dot{\underline{b}}$ within the state vector to be estimated. The justification for this is that one needs to account for spin rate variations scaled by uncertainties in FOG transfer function parameters. The variation in the spin rate during an actuation free pointing in science mode, results from external environmental disturbance torques and venting torques acting on the spacecraft. This variation in the spin rate is approximately linear.

The spacecraft kinematics in terms of quaternions is therefore given as:-

$$\dot{\underline{q}} = \frac{1}{2}\Omega(\underline{\omega}_B' - \underline{b} - \underline{\eta})\underline{q} = \frac{1}{2}\Theta(\underline{q})(\underline{\omega}_B' - \underline{b} - \underline{\eta}) = \frac{1}{2}\underline{\omega} \otimes \underline{q} \tag{2}$$

where $\Omega(\underline{v})$ and $\Theta(\underline{q})$ are defined earlier in the section on Notation and Conventions.
Taking the expectation of (2), the complete state prediction model can be approximated as follows:-

$$\frac{d}{dt}\begin{bmatrix}\hat{\underline{q}}\\ \hat{\underline{b}}\\ \dot{\hat{\underline{b}}}\end{bmatrix} = \begin{bmatrix}\frac{1}{2}\Omega(\hat{\underline{\omega}})\hat{\underline{q}}\\ \dot{\hat{\underline{b}}}\\ \underline{0}\end{bmatrix} = \begin{bmatrix}\frac{1}{2}\Omega(\underline{\omega}_B' - \hat{\underline{b}})\hat{\underline{q}}\\ \dot{\hat{\underline{b}}}\\ \underline{0}\end{bmatrix} = \begin{bmatrix}\frac{1}{2}\Omega(\underline{\omega}_B')\hat{\underline{q}} - \frac{1}{2}\Theta(\hat{\underline{q}})\hat{\underline{b}}\\ \dot{\hat{\underline{b}}}\\ \underline{0}\end{bmatrix} \tag{3}$$

For the rest of the formulation we follow the approach detailed in [15]. The covariance matrix for the state vector in (3) is singular, due to the quaternion norm constraint. For this reason, in order to linearise the system given by (2), we use the body-fixed covariance representation.

Defining the error quaternion as:-

$$\delta\underline{q} = \underline{q} \otimes \hat{\underline{q}}^{-1} \tag{4}$$

and the rate bias error as:-

$$\delta\underline{b} = \underline{b} - \hat{\underline{b}} \tag{5}$$

It can be shown that:-

$$\begin{aligned}\delta\dot{\underline{q}} &= [[\hat{\underline{\omega}}]]\delta\underline{q} - \frac{1}{2}\delta\underline{b}\\ \delta\dot{q}_4 &= 0\\ \delta\ddot{\underline{b}} &= \underline{0}\end{aligned} \tag{6}$$

or in matrix form, the linearised state prediction model can be written:-

$$\frac{d}{dt}\begin{bmatrix}\delta\underline{q}\\ \delta\underline{b}\\ \delta\dot{\underline{b}}\end{bmatrix} = \begin{bmatrix} F_A & F_B & 0_{3\times3}\\ 0_{3\times3} & 0_{3\times3} & I_3\\ 0_{3\times3} & 0_{3\times3} & 0_{3\times3}\end{bmatrix}\begin{bmatrix}\delta\underline{q}\\ \delta\underline{b}\\ \delta\dot{\underline{b}}\end{bmatrix} \tag{7}$$

where the sub-matrices in the linearised system in (7) are given as follows:-

$$\begin{aligned} F_A &= [[\hat{\underline{\omega}}]]\\ F_B &= -\frac{1}{2}I_3 \end{aligned} \tag{8}$$

2.4.2 Measurement Model

The measurement model is linear since the star tracker provides directly a measurement of the attitude quaternion. Combining this with the alignment of the star tracker with respect to the body reference system yields the measured inertial to body transformation.

The measured quaternion is then given by:-

$$\underset{\sim}{q}_{STR} = \underset{\sim}{q}_{\nu} \otimes \underset{\sim}{q} \tag{9}$$

where $\underset{\sim}{q}_{\nu}$ is measurement noise represented as a quaternion which can be approximated as:-

$$\underset{\sim}{q}_{\nu} = \begin{bmatrix}\dfrac{\underline{\nu}}{\sqrt{1-\|\underline{\nu}\|^2}}\end{bmatrix} \approx \begin{bmatrix}\underline{\nu}\\ 1\end{bmatrix} \tag{10}$$

where the measurement errors $\underline{\nu}$ are assumed to be zero mean and Gaussian.

The linearised measurement equation in terms of the vector part of the error quaternion defined in (4) is then given by:-

$$\delta\underline{q}_{STR} = H\begin{bmatrix}\delta\underline{q}\\ \delta\underline{b}\\ \delta\dot{\underline{b}}\end{bmatrix} + \delta\underline{\nu} = \delta\underline{q} + \delta\underline{\nu} \tag{11}$$

where

$$H = \begin{bmatrix}H_q & H_b & H_{\dot{b}}\end{bmatrix} = \begin{bmatrix}I_3 & 0_{3\times6}\end{bmatrix} \tag{12}$$

2.5 Dynamic Model Based Estimation Algorithm (HCM)

The following section presents the state prediction and measurement models, that are used within a batch least squares algorithm. This algorithm is used to estimate the state vector at a specified epoch by processing all the star tracker measurements, rejecting outliers based on thresholds computed using the statistics of the observation residuals. The general implementation of the batch least squares algorithm implementation is described in Appendix C.

This algorithm will be used to filter STR attitude quaternion data during nominal reorientation slews in HCM. A complete description of the on-board HCM controller is given in Section 5.6 and Annex D of [16].

2.5.1 State Prediction Model

In this case, the general state prediction model uses a model of the spacecraft kinematics and dynamics. The time evolution of all the state variables is given by:-

$$\begin{aligned}
\dot{\underset{\sim}{q}} &= \frac{1}{2}\Omega(\underline{\omega}_B)\underset{\sim}{q} = \frac{1}{2}\Theta(\underset{\sim}{q})\underline{\omega}_B = f_q(\underset{\sim}{q}, \underline{\omega}_B) \\
\dot{\underline{\omega}}_B &= J_B^{-1}(\underline{\tau}_{B_i} + [[\underline{\omega}_B]]J_B\underline{\omega}_B) = f_\omega(\underline{\omega}_B, \underline{\tau}_{B_i}) \\
\dot{\underline{\tau}}_{B_i} &= \underline{0}
\end{aligned} \tag{13}$$

where:-

$\underset{\sim}{q}$ is the true attitude quaternion

$\underline{\omega}_B$ is the true angular rate vector expressed in spacecraft body axes

$\underline{\tau}_{B_i}$ is the true external torque vector expressed in spacecraft body reference system during the i^{th} interval of the nominal HCM reorientation slew timeline (see Figure 1).

J_B is the spacecraft inertia tensor

and $\Omega(\underline{\nu})$ and $\Theta(\underset{\sim}{q})$ are defined in section Notation and Conventions

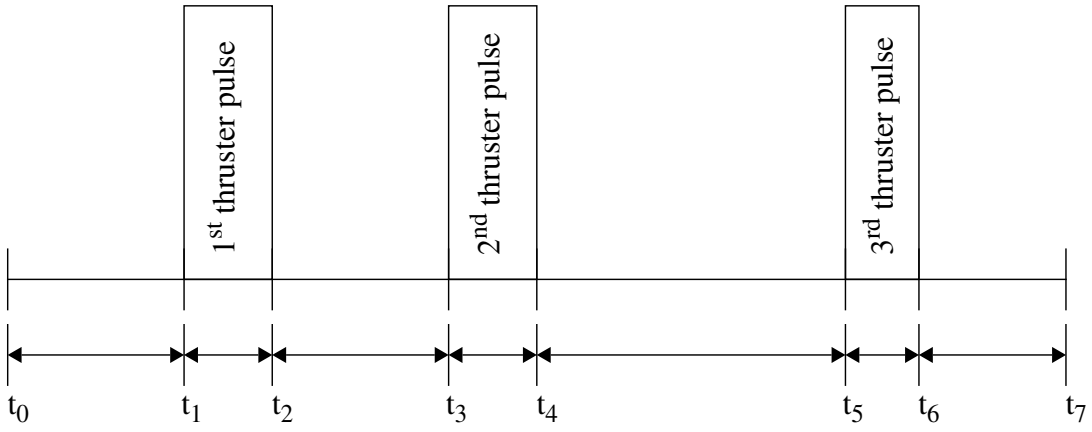

FIGURE 1: Nominal re-orientation slew in HCM timeline

Referring to the timeline shown in Figure 1, the nominal values for the applied torques during the various time intervals are given as follows:-

$$\begin{aligned}
t_0 \le t < t_1, \underline{\tau}_{B_1} &= \underline{0} \qquad t_1 \le t \le t_2, \underline{\tau}_{B_2} = \underline{\tau} \\
t_2 < t < t_3, \underline{\tau}_{B_3} &= \underline{0} \qquad t_3 \le t \le t_4, \underline{\tau}_{B_4} = \underline{\tau} \\
t_4 < t < t_5, \underline{\tau}_{B_5} &= \underline{0} \qquad t_5 \le t \le t_6, \underline{\tau}_{B_6} = \underline{\tau} \\
t_6 < t \le t_7, \underline{\tau}_{B_7} &= \underline{0}
\end{aligned} \tag{14}$$

It is noted that no assumptions about thrust level repeatability within the estimator formulation have been made. An independent torque vector, expressed in the spacecraft body reference system, is estimated for each part of the timeline as identified in (15). The justification for this is due to uncertainties in the applied thruster force, resulting from time delays (leading and trailing edge of commanded thruster pulse), time response to reach steady-state thrust and a random impulse bit component.

Taking the expectation of (13), the complete state prediction model can be approximated as follows:-

$$\frac{d}{dt}\begin{bmatrix}\hat{\underset{\sim}{q}}\\ \hat{\underline{\omega}}_B\\ \hat{\underline{\tau}}_{B_i}\end{bmatrix} = \begin{bmatrix}\frac{1}{2}\Omega(\hat{\underline{\omega}}_B)\hat{\underset{\sim}{q}}\\ J_B^{-1}[[\hat{\underline{\omega}}_B]]J_B\hat{\underline{\omega}}_B + \sum_{i=1}^{7} F_i\hat{\underline{\tau}}_{B_i}\\ \underline{0}\end{bmatrix} = \begin{bmatrix}f_q(\hat{\underset{\sim}{q}}, \hat{\underline{\omega}}_B)\\ f_\omega(\hat{\underline{\omega}}_B, \hat{\underline{\tau}}_{B_i})\\ \underline{0}\end{bmatrix} \tag{15}$$

where the matrices F_i are set according to the HCM nominal reorientation slew timeline (see Figure 1), according to the following logic:-

$$\begin{aligned}&IF(t_{i-1} < t < t_i)THEN\\ &\quad F_i = J_B^{-1}\\ &ELSE\\ &\quad F_i = 0_{3\times 3}\\ &ENDIF\end{aligned} \tag{16}$$

As before, the rest of the formulation follows the approach detailed in [15].

Defining the error quaternion as in (4), then it can be shown that:-

$$\begin{aligned}\delta\dot{\underline{q}} &= [[\hat{\underline{\omega}}_B]]\delta\underline{q} + \frac{1}{2}\delta\underline{\omega}\\ \delta\dot{q}_4 &= 0\\ \delta\dot{\underline{\omega}} &= J_B^{-1}([[\hat{\underline{\omega}}_B]]J_B - [[J_B\hat{\underline{\omega}}_B]])\delta\underline{\omega} + \sum_{i=1}^{7} F_i\delta\underline{\tau}_i\\ \delta\dot{\underline{\tau}}_i &= \underline{0}\end{aligned} \tag{17}$$

or in matrix form, the linearised state prediction model can be written:-

$$\frac{d}{dt}\begin{bmatrix}\delta\underline{q}\\ \delta\underline{\omega}\\ \delta\underline{\tau}_1\\ \delta\underline{\tau}_2\\ \delta\underline{\tau}_3\\ \delta\underline{\tau}_4\\ \delta\underline{\tau}_5\\ \delta\underline{\tau}_6\\ \delta\underline{\tau}_7\end{bmatrix} = \begin{bmatrix}F_A & F_B & 0_{3\times3} & 0_{3\times3} & 0_{3\times3} & 0_{3\times3} & 0_{3\times3} & 0_{3\times3} & 0_{3\times3}\\ 0_{3\times3} & F_C & F_1 & F_2 & F_3 & F_4 & F_5 & F_6 & F_7\\ 0_{3\times3} & 0_{3\times3} & 0_{3\times3} & 0_{3\times3} & 0_{3\times3} & 0_{3\times3} & 0_{3\times3} & 0_{3\times3} & 0_{3\times3}\\ 0_{3\times3} & 0_{3\times3} & 0_{3\times3} & 0_{3\times3} & 0_{3\times3} & 0_{3\times3} & 0_{3\times3} & 0_{3\times3} & 0_{3\times3}\\ 0_{3\times3} & 0_{3\times3} & 0_{3\times3} & 0_{3\times3} & 0_{3\times3} & 0_{3\times3} & 0_{3\times3} & 0_{3\times3} & 0_{3\times3}\\ 0_{3\times3} & 0_{3\times3} & 0_{3\times3} & 0_{3\times3} & 0_{3\times3} & 0_{3\times3} & 0_{3\times3} & 0_{3\times3} & 0_{3\times3}\\ 0_{3\times3} & 0_{3\times3} & 0_{3\times3} & 0_{3\times3} & 0_{3\times3} & 0_{3\times3} & 0_{3\times3} & 0_{3\times3} & 0_{3\times3}\\ 0_{3\times3} & 0_{3\times3} & 0_{3\times3} & 0_{3\times3} & 0_{3\times3} & 0_{3\times3} & 0_{3\times3} & 0_{3\times3} & 0_{3\times3}\\ 0_{3\times3} & 0_{3\times3} & 0_{3\times3} & 0_{3\times3} & 0_{3\times3} & 0_{3\times3} & 0_{3\times3} & 0_{3\times3} & 0_{3\times3}\end{bmatrix}\begin{bmatrix}\delta\underline{q}\\ \delta\underline{\omega}\\ \delta\underline{\tau}_1\\ \delta\underline{\tau}_2\\ \delta\underline{\tau}_3\\ \delta\underline{\tau}_4\\ \delta\underline{\tau}_5\\ \delta\underline{\tau}_6\\ \delta\underline{\tau}_7\end{bmatrix} \tag{18}$$

where the sub-matrices in the linearised system in (18) are given as follows:-

$$\begin{aligned}F_A &= [[\hat{\underline{\omega}}_B]]\\ F_B &= \frac{1}{2}I_3\\ F_C &= J_B^{-1}([[\hat{\underline{\omega}}_B]]J_B - [[J_B\hat{\underline{\omega}}_B]])\end{aligned} \tag{19}$$

and as already mentioned before, the matrices F_i are defined according to the HCM nominal slew timeline (see Figure 1), together with the logic given by (16).

2.5.2 Measurement Model

The measurement model is given by (9) in Section 2.4.2.

The linearised measurement equation in terms of the vector part of the error quaternion, defined in (4), is then given by:-

$$\delta\underline{q}_{STR} = H\left[\delta\underline{q}\ \delta\underline{\omega}\ \delta\underline{\tau}_1\ \delta\underline{\tau}_2\ \delta\underline{\tau}_3\ \delta\underline{\tau}_4\ \delta\underline{\tau}_5\ \delta\underline{\tau}_6\ \delta\underline{\tau}_7\right]^T + \delta\underline{\nu} = \delta\underline{q} + \delta\underline{\nu} \tag{20}$$

where

$$H = \left[H_q\ H_\omega\ H_{\tau_1}\ H_{\tau_2}\ H_{\tau_3}\ H_{\tau_4}\ H_{\tau_5}\ H_{\tau_6}\ H_{\tau_7}\right] = \left[I_3\ 0_{3\times 24}\right] \tag{21}$$

2.6 Dynamic Model Based Estimation Algorithm (SCM)

The following section presents the state prediction and measurement models, that are used within a batch least squares algorithm. This algorithm is used to estimate the state vector at a specified epoch by processing all the star tracker measurements, rejecting outliers based on thresholds computed using the statistics of the observation residuals. The general implementation of the batch least squares algorithm implementation is described in Appendix C.

This algorithm will be used to filter STR attitude quaternion data during stable pointing phases in SCM, also taking into account periodic internal disturbance torques created by the sorption cooler sub-system. The normal state operational mode of the sorption cooler sub-system is described in Section 6.2.4.3 of [17].

2.6.1 State Prediction Model

In this case, the general state prediction model uses a model of the spacecraft kinematics and dynamics. The time evolution of all the state variables is given by:-

$$\begin{aligned}
\dot{\underline{q}} &= \frac{1}{2}\Omega(T_{BP}(\underline{\Psi},\Psi_3)\underline{\omega}_P)\underline{q} = \frac{1}{2}\Theta(\underline{q})T_{BP}(\underline{\Psi},\Psi_3)\underline{\omega}_P = f_q(\underline{q},\underline{\omega}_P,\underline{\Psi},\Psi_3)\\
\dot{\underline{\omega}}_P &= J_P^{-1}\left(\underline{\tau}_P - \begin{bmatrix}\sum_{i=1}^{5} x_i\\ 0\\ 0\end{bmatrix} + [[\underline{\omega}_P]]J_P\underline{\omega}_P\right) = f_\omega(\underline{\omega}_P,\underline{\tau}_P,\underline{x},\omega_{scs})\\
\dot{\underline{\tau}}_P &= [[\underline{\omega}_P]]\underline{\tau}_P = f_\tau(\underline{\omega}_P,\underline{\tau}_P)\\
\ddot{\underline{\Psi}} &= \underline{0}\\
\ddot{x}_i &= -\omega_i^2 x_i\\
\dot{\omega}_{scs} &= 0
\end{aligned} \tag{22}$$

where:-

$\underset{\sim}{q}$ is the true attitude quaternion

$\underline{\omega}_P$ is the true angular rate vector expressed in spacecraft principal axes

$\underline{\tau}_P$ is the true external torque vector expressed in spacecraft principal axes

$T_{BP}(\underline{\Psi},\Psi_3)$ is the principal axis to body axis transformation matrix which is a function of the principal axis tilt angles $\underline{\Psi} = (\Psi_1, \Psi_2)$ and principal axis azimuth angle, Ψ_3, is obtained from the predicted

mass properties.

J_P is the principal axis inertia tensor, which is obtained from the predicted mass properties.

x_i is the i^{th} periodic component of the sorption cooler disturbance torque with frequency ω_i, i=1…5.

and $\Omega(\underline{\nu})$ and $\Theta(\underline{q})$ are defined earlier in the section on Notation and Conventions.

During pointings in SCM, the following states, $\underset{\sim}{q}$, $\underline{\omega}_P$, $\underline{\tau}_P$, $\underline{\Psi}$, $\underline{\psi}$, x_i, $\dot{x}_i$, ω_{scs}, are estimated. It is assumed that the disturbance torques, expressed in the inertial reference system, are constant during pointings in SCM. The estimation of the parameter, ψ_3, is only possible when there is a sufficient level of residual nutation on the spacecraft, which is not the case for SCM pointings. The best possible knowledge of this parameter can only be obtained from the predicted mass properties.

A frequency analysis of STR attitude quaternion data and FOG integrated angular rate during a long SCM pointing of OD 0561, revealed that the internal disturbance torques are periodic with frequency components that are fixed multiples of the compressor cycle frequency. This compressor cycle frequency is the inverse of the commanded look up table (LUT) cycle time, which is used to provide an initial estimate for the frequency ω_{scs}. From this analysis, five frequencies have been retained, namely:-

$$\begin{bmatrix}\omega_1 & \omega_2 & \omega_3 & \omega_4 & \omega_5\end{bmatrix} = \begin{bmatrix}\frac{1}{6} & \frac{1}{3} & \frac{1}{2} & 1 & 2\end{bmatrix}\omega_{scs} \tag{23}$$

Taking the expectation of (22), the complete state prediction model can be approximated as follows:-

$$\frac{d}{dt}\begin{bmatrix}\hat{\underset{\sim}{q}}\\ \hat{\underline{\omega}}_P\\ \hat{\underline{\tau}}_P\\ \hat{\underline{\Psi}}\\ \dot{\hat{\underline{\Psi}}}\\ \hat{x}_1\\ \dot{\hat{x}}_1\\ \hat{x}_2\\ \dot{\hat{x}}_2\\ \hat{x}_3\\ \dot{\hat{x}}_3\\ \hat{x}_4\\ \dot{\hat{x}}_4\\ \hat{x}_5\\ \dot{\hat{x}}_5\\ \hat{\omega}_{scs}\end{bmatrix} = \begin{bmatrix}f_q(\hat{\underset{\sim}{q}}, \hat{\underline{\omega}}_P, \hat{\underline{\Psi}}, \hat{\psi}_3)\\ f_\omega(\hat{\underline{\omega}}_P, \hat{\underline{\tau}}_P, \hat{\underline{x}}, \hat{\omega}_{scs})\\ f_\tau(\hat{\underline{\omega}}_P, \hat{\underline{\tau}}_P)\\ \dot{\hat{\underline{\Psi}}}\\ \underline{0}\\ \dot{\hat{x}}_1\\ -\hat{\omega}_1^2\hat{x}_1\\ \dot{\hat{x}}_2\\ -\hat{\omega}_2^2\hat{x}_2\\ \dot{\hat{x}}_3\\ -\hat{\omega}_3^2\hat{x}_3\\ \dot{\hat{x}}_4\\ -\hat{\omega}_4^2\hat{x}_4\\ \dot{\hat{x}}_5\\ -\hat{\omega}_5^2\hat{x}_5\\ 0\end{bmatrix} \tag{24}$$

As before the rest of the formulation follows the approach detailed in [15].

Defining the error quaternion as in (4), then it can be shown that:-

$$
\begin{aligned}
\delta\dot{\underline{q}} &= [[\hat{T}_{BP}\hat{\underline{\omega}}_P]]\delta\underline{q} + \frac{1}{2}\hat{T}_{BP}\delta\underline{\omega}_P + \frac{1}{2}\sum_{i=1}^{2}\left[\left(\frac{\partial\hat{T}_{BP}}{\partial\hat{\psi}_i}\right)\hat{\underline{\omega}}_P\right]\delta\psi_i \\
\delta\dot{q}_4 &= 0 \\
\delta\dot{\underline{\omega}}_P &= J_P^{-1}([[\hat{\underline{\omega}}_P]]J_P - [[J_P\hat{\underline{\omega}}_P]])\delta\underline{\omega}_P + J_P^{-1}\delta\underline{\tau}_P + J_P^{-1}\begin{bmatrix}\sum_{i=1}^{5}\left(-\delta x_i - \frac{t\dot{\hat{x}}_i}{\hat{\omega}_i}\left(\frac{\partial\hat{\omega}_i}{\partial\hat{\omega}_{scs}}\right)\delta\omega_{scs}\right)\\ 0 \\ 0\end{bmatrix} \\
\delta\dot{\underline{\tau}}_P &= -[[\hat{\underline{\tau}}_P]]\delta\underline{\omega}_P + [[\hat{\underline{\omega}}_P]]\delta\underline{\tau}_P \\
\delta\ddot{\underline{\psi}} &= \underline{0} \\
\delta\ddot{x}_i &= -\hat{\omega}_i^2\delta x_i - 2\hat{\omega}_i\dot{\hat{x}}_i\left(\frac{\partial\hat{\omega}_i}{\partial\hat{\omega}_{scs}}\right)\delta\omega_{scs} \\
\delta\dot{\omega}_{scs} &= 0
\end{aligned}
\tag{25}
$$

or in matrix form, the linearised state prediction model can be written:-

$$
\frac{d}{dt}\begin{bmatrix}
\delta\underline{q} \\ \delta\underline{\omega}_P \\ \delta\underline{\tau}_P \\ \delta\underline{\psi} \\ \delta\dot{\underline{\psi}} \\ \delta x_1 \\ \delta\dot{x}_1 \\ \delta x_2 \\ \delta\dot{x}_2 \\ \delta x_3 \\ \delta\dot{x}_3 \\ \delta x_4 \\ \delta\dot{x}_4 \\ \delta x_5 \\ \delta\dot{x}_5 \\ \delta\omega_{scs}
\end{bmatrix} =
\begin{bmatrix}
F_A & F_B & 0_{3\times3} & F_C & 0_{3\times2} & 0_{3\times1} & 0_{3\times1} & 0_{3\times1} & 0_{3\times1} & 0_{3\times1} & 0_{3\times1} & 0_{3\times1} & 0_{3\times1} & 0_{3\times1} & 0_{3\times1} & 0_{3\times1} \\
0_{3\times3} & F_D & F_E & 0_{3\times2} & 0_{3\times2} & F_F & 0_{3\times1} & F_F & 0_{3\times1} & F_F & 0_{3\times1} & F_F & 0_{3\times1} & F_F & 0_{3\times1} & F_I \\
0_{3\times3} & F_J & F_K & 0_{3\times2} & 0_{3\times2} & 0_{3\times1} & 0_{3\times1} & 0_{3\times1} & 0_{3\times1} & 0_{3\times1} & 0_{3\times1} & 0_{3\times1} & 0_{3\times1} & 0_{3\times1} & 0_{3\times1} & 0_{3\times1} \\
0_{2\times3} & 0_{2\times3} & 0_{2\times3} & 0_{2\times2} & I_2 & 0_{2\times1} & 0_{2\times1} & 0_{2\times1} & 0_{2\times1} & 0_{2\times1} & 0_{2\times1} & 0_{2\times1} & 0_{2\times1} & 0_{2\times1} & 0_{2\times1} & 0_{2\times1} \\
0_{2\times3} & 0_{2\times3} & 0_{2\times3} & 0_{2\times2} & 0_{2\times1} & 0_{2\times1} & 0_{2\times1} & 0_{2\times1} & 0_{2\times1} & 0_{2\times1} & 0_{2\times1} & 0_{2\times1} & 0_{2\times1} & 0_{2\times1} & 0_{2\times1} & 0_{2\times1} \\
0 & 0 & 0 & 0 & 0 & 0 & 1 & 0 & 0 & 0 & 0 & 0 & 0 & 0 & 0 & 0 \\
0 & 0 & 0 & 0 & 0 & F_L & 0 & 0 & 0 & 0 & 0 & 0 & 0 & 0 & 0 & F_M \\
0 & 0 & 0 & 0 & 0 & 0 & 0 & 0 & 1 & 0 & 0 & 0 & 0 & 0 & 0 & 0 \\
0 & 0 & 0 & 0 & 0 & 0 & 0 & F_N & 0 & 0 & 0 & 0 & 0 & 0 & 0 & F_O \\
0 & 0 & 0 & 0 & 0 & 0 & 0 & 0 & 0 & 0 & 1 & 0 & 0 & 0 & 0 & 0 \\
0 & 0 & 0 & 0 & 0 & 0 & 0 & 0 & 0 & F_P & 0 & 0 & 0 & 0 & 0 & F_Q \\
0 & 0 & 0 & 0 & 0 & 0 & 0 & 0 & 0 & 0 & 0 & 0 & 1 & 0 & 0 & 0 \\
0 & 0 & 0 & 0 & 0 & 0 & 0 & 0 & 0 & 0 & 0 & F_R & 0 & 0 & 0 & F_S \\
0 & 0 & 0 & 0 & 0 & 0 & 0 & 0 & 0 & 0 & 0 & 0 & 0 & 0 & 1 & 0 \\
0 & 0 & 0 & 0 & 0 & 0 & 0 & 0 & 0 & 0 & 0 & 0 & 0 & F_T & 0 & F_U \\
0 & 0 & 0 & 0 & 0 & 0 & 0 & 0 & 0 & 0 & 0 & 0 & 0 & 0 & 0 & 0
\end{bmatrix}
\begin{bmatrix}
\delta\underline{q} \\ \delta\underline{\omega}_P \\ \delta\underline{\tau}_P \\ \delta\underline{\psi} \\ \delta\dot{\underline{\psi}} \\ \delta x_1 \\ \delta\dot{x}_1 \\ \delta x_2 \\ \delta\dot{x}_2 \\ \delta x_3 \\ \delta\dot{x}_3 \\ \delta x_4 \\ \delta\dot{x}_4 \\ \delta x_5 \\ \delta\dot{x}_5 \\ \delta\omega_{scs}
\end{bmatrix}
\tag{26}
$$

The sub-matrices in the linearised system in (26) are given as follows:-

$$
\begin{aligned}
F_A &= [[\hat{T}_{BP}\hat{\underline{\omega}}_P]] & F_J &= -[[\hat{\underline{\tau}}_P]] \\
F_B &= \frac{1}{2}\hat{T}_{BP} & F_K &= [[\hat{\underline{\omega}}_P]] \\
F_C &= \frac{1}{2}\left[\left(\frac{\partial \hat{T}_{BP}}{\partial \hat{\psi}_1}\right)\hat{\underline{\omega}}_P \left(\frac{\partial \hat{T}_{BP}}{\partial \hat{\psi}_2}\right)\hat{\underline{\omega}}_P\right] & F_L &= -\hat{\omega}_1^2 \\
F_D &= J_P^{-1}([[\hat{\underline{\omega}}_P]]J_P - [[J_P\hat{\underline{\omega}}_P]]) & F_M &= -2\hat{\omega}_1\hat{x}_1 \\
F_E &= J_P^{-1} & F_N &= -\hat{\omega}_2^2 \\
F_F &= -J_P^{-1}\begin{bmatrix}1\\0\\0\end{bmatrix} & F_O &= -2\hat{\omega}_2\hat{x}_2 \\
F_I &= F_F\sum_{i=1}^{5}\left(\frac{t\dot{x}_i}{\omega_i}\left(\frac{\partial \omega_i}{\partial \omega_{scs}}\right)\right) & F_P &= -\hat{\omega}_3^2 \\
 & & F_Q &= -2\hat{\omega}_3\hat{x}_3 \\
 & & F_R &= -\hat{\omega}_4^2 \\
 & & F_S &= -2\hat{\omega}_4\hat{x}_4 \\
 & & F_T &= -\hat{\omega}_5^2 \\
 & & F_U &= -2\hat{\omega}_5\hat{x}_5
\end{aligned}
\tag{27}
$$

The analytical expressions for the above partial derivatives are derived in Appendix B.1.

2.6.2 Measurement Model

The measurement model is given by (9) in Section 2.4.2.

The linearised measurement equation in terms of the vector part of the error quaternion defined in (4) is then given by:-

$$
\delta\underline{q}_{STR} = H\left[\delta\underline{q}\ \delta\underline{\omega}_P\ \delta\underline{\tau}_P\ \delta\underline{\psi}\ \delta\underline{\dot{\psi}}\ \delta x_1\ \delta\dot{x}_1\ \delta x_2\ \delta\dot{x}_2\ \delta x_3\ \delta\dot{x}_3\ \delta x_4\ \delta\dot{x}_4\ \delta x_5\ \delta\dot{x}_5\ \delta\omega_{scs}\right]^T + \delta\underline{\nu} = \delta\underline{q} + \delta\underline{\nu} \tag{28}
$$

where the measurement geometry matrix is given by:-

$$
H = \left[H_q\ H_\omega\ H_\tau\ H_{x_1}\ H_{\dot{x}_1}\ H_{x_2}\ H_{\dot{x}_2}\ H_{x_3}\ H_{\dot{x}_3}\ H_{x_4}\ H_{\dot{x}_4}\ H_{x_5}\ H_{\dot{x}_5}\ H_{\omega_{scs}}\right] = \left[I_3\ 0_{3\times 21}\right] \tag{29}
$$

2.7 Dynamic Model Based Inertia Tensor Estimation Algorithm

The following section presents the state prediction and measurement models, that are used within a batch least squares algorithm. This algorithm is used to estimate the state vector at a specified epoch by processing all the star tracker measurements, rejecting outliers based on thresholds computed using the statistics of the observation residuals. The spacecraft inertia tensor can be reconstructed from some of these parameters in the estimated state vector. The batch least squares algorithm implementation is described in Appendix C.

This algorithm will be used to filter STR attitude quaternion data and estimate all the required parameters necessary to reconstruct an estimate of the spacecraft inertia tensor.

2.7.1 State Prediction Model

In this case, the general state prediction model uses a model of the spacecraft kinematics and dynamics. The time evolution of all the state variables is given by:-

$$
\begin{aligned}
\dot{\underset{\sim}{q}} &= \frac{1}{2}\Omega(T_{BP}(\underline{\Psi},\psi_3)\underline{\omega}_P)\underset{\sim}{q} = \frac{1}{2}\Theta(\underset{\sim}{q})T_{BP}(\underline{\Psi},\psi_3)\underline{\omega}_P = f_q(\underset{\sim}{q}, \underline{\omega}_P, \underline{\Psi},\psi_3)\\
\dot{\underline{\omega}}_P &= J_P^{-1}(\nu_n, \Delta)(\underline{\tau}_P + [[\underline{\omega}_P]]J_P(\nu_n, \Delta)\underline{\omega}_P) = f_\omega(\underline{\omega}_P, \underline{\tau}_P, \nu_n, \Delta)\\
\dot{\underline{\tau}}_P &= [[\underline{\omega}_P]]\underline{\tau}_P = f_\tau(\underline{\omega}_P, \underline{\tau}_P)\\
\ddot{\underline{\Psi}} &= \underline{0}\\
\dot{\nu}_n &= 0\\
\dot{\Delta} &= 0\\
\dot{\psi}_3 &= 0
\end{aligned}
\tag{30}
$$

where:-

$\underset{\sim}{q}$ is the true attitude quaternion

$\underline{\omega}_P$ is the true angular rate vector expressed in spacecraft principal axes

$\underline{\tau}_P$ is the true external torque vector expressed in spacecraft principal axes

$T_{BP}(\underline{\Psi},\psi_3)$ is the principal axis to body axis transformation matrix which is a function of the principal axis tilt angles $\underline{\Psi} = (\psi_1, \psi_2)$ and principal axis azimuth angle ψ_3

$J_P(\nu_n, \Delta)$ is the principal axis inertia tensor which is a function of the nutation to spin rate ratio, ν_n, and the axial imbalance, Δ. See Appendix B.2 to see how they are related to the principal axis moments of inertias.

Also, $\Omega(\underline{\nu})$ and $\Theta(\underset{\sim}{q})$ are defined earlier in Notation and Conventions.

Taking the expectation of (30), the complete state prediction model can be approximated as follows:-

$$
\frac{d}{dt}\begin{bmatrix}
\hat{\underset{\sim}{q}}\\ \hat{\underline{\omega}}_P\\ \hat{\underline{\tau}}_P\\ \hat{\underline{\Psi}}\\ \dot{\hat{\underline{\Psi}}}\\ \hat{\nu}_n\\ \dot{\hat{\nu}}_n\\ \hat{\Delta}\\ \hat{\psi}_3
\end{bmatrix} =
\begin{bmatrix}
\frac{1}{2}\Omega(T_{BP}(\hat{\underline{\Psi}},\hat{\psi}_3)\hat{\underline{\omega}}_P)\hat{\underset{\sim}{q}}\\
J_P^{-1}(\hat{\nu}_n, \hat{\Delta})(\hat{\underline{\tau}}_P + [[\hat{\underline{\omega}}_P]]J_P(\hat{\nu}_n, \hat{\Delta})\hat{\underline{\omega}}_P)\\
[[\hat{\underline{\omega}}_P]]\hat{\underline{\tau}}_P\\
\dot{\hat{\underline{\Psi}}}\\ 0\\ \dot{\hat{\nu}}_n\\ 0\\ 0\\ 0
\end{bmatrix} =
\begin{bmatrix}
f_q(\hat{\underset{\sim}{q}}, \hat{\underline{\omega}}_P, \hat{\underline{\Psi}},\hat{\psi}_3)\\
f_\omega(\hat{\underline{\omega}}_P, \hat{\underline{\tau}}_P, \hat{\nu}_n, \hat{\Delta})\\
f_\tau(\hat{\underline{\omega}}_P, \hat{\underline{\tau}}_P)\\
\dot{\hat{\underline{\Psi}}}\\ 0\\ \dot{\hat{\nu}}_n\\ 0\\ 0\\ 0
\end{bmatrix}
\tag{31}
$$

As in the previous case, the rest of the formulation follows the approach in [15].

Defining the error quaternion as in (4), then it can be shown that:-

$$
\begin{aligned}
\delta\dot{\underline{q}} &= [[\hat{T}_{BP}\hat{\underline{\omega}}_P]]\delta\underline{q} + \frac{1}{2}\hat{T}_{BP}\delta\underline{\omega}_P + \frac{1}{2}\sum_{i=1}^{3}\left[\left(\frac{\partial\hat{T}_{BP}}{\partial\hat{\psi}_i}\right)\hat{\underline{\omega}}_P\right]\delta\psi_i \\
\delta\dot{q}_4 &= 0 \\
\delta\dot{\underline{\omega}}_P &= J_P^{-1}(\hat{\nu}_n, \hat{\Delta})([[\hat{\underline{\omega}}_P]]J_P(\hat{\nu}_n, \hat{\Delta}) - [[J_P(\hat{\nu}_n, \hat{\Delta})\hat{\underline{\omega}}_P]])\delta\underline{\omega}_P + J_P^{-1}(\hat{\nu}_n, \hat{\Delta})\delta\underline{\tau}_P \\
\delta\dot{\underline{\tau}}_P &= -[[\hat{\underline{\tau}}_P]]\delta\underline{\omega}_P + [[\hat{\underline{\omega}}_P]]\delta\underline{\tau}_P \\
\delta\ddot{\underline{\psi}} &= \underline{0} \\
\delta\ddot{\nu}_n &= 0 \\
\delta\dot{\Delta} &= 0 \\
\delta\dot{\psi}_3 &= 0
\end{aligned}
\tag{32}
$$

During routine pointings in SCM mode, the following states, q, $\underline{\omega}_P$, $\underline{\tau}_P$, $\underline{\psi}$, $\dot{\underline{\psi}}$, are estimated. Estimation of the parameters, ν_n, $\dot{\nu}_n$, Δ, ψ_3, is only possible when there is a sufficient level of residual nutation on the spacecraft. If this is not the case, these parameters are unobservable. A sufficient level of residual nutation is usually present after completing a routine station keeping manoeuvre, where the spacecraft is still in OCM mode, just prior to a nutation damping by commanding a manoeuvre in HCM to the same target inertial angular momentum vector.

Based on the estimated parameters, $\underline{\psi}$, ψ_3, ν_n, Δ, together with a knowledge of the X-axis principal moment of inertia from the predicted mass properties, it is possible to reconstruct the complete spacecraft inertia tensor.

The current algorithm in use during routine operations for inertia tensor calibration is referenced in Section 2.2.

In matrix form, the linearised state prediction model given by (32) can be written:-

$$
\frac{d}{dt}\begin{bmatrix}
\delta\underline{q} \\ \delta\underline{\omega}_P \\ \delta\underline{\tau}_P \\ \delta\underline{\psi} \\ \delta\dot{\underline{\psi}} \\ \delta\nu_n \\ \delta\dot{\nu}_n \\ \delta\Delta \\ \delta\psi_3
\end{bmatrix} =
\begin{bmatrix}
F_A & F_B & 0_{3\times3} & F_C & 0_{3\times2} & 0_{3\times1} & 0_{3\times1} & 0_{3\times1} & F_D \\
0_{3\times3} & F_E & F_F & 0_{3\times2} & 0_{3\times2} & F_G & 0_{3\times1} & F_H & 0_{3\times1} \\
0_{3\times3} & F_I & F_J & 0_{3\times2} & 0_{3\times2} & 0_{3\times1} & 0_{3\times1} & 0_{3\times1} & 0_{3\times1} \\
0_{2\times3} & 0_{2\times3} & 0_{2\times3} & 0_{2\times2} & I_2 & 0_{2\times1} & 0_{2\times1} & 0_{2\times1} & 0_{2\times1} \\
0_{2\times3} & 0_{2\times3} & 0_{2\times3} & 0_{2\times2} & 0_{2\times2} & 0_{2\times1} & 0_{2\times1} & 0_{2\times1} & 0_{2\times1} \\
0_{1\times3} & 0_{1\times3} & 0_{1\times3} & 0_{1\times2} & 0_{1\times2} & 0 & 1 & 0 & 0 \\
0_{1\times3} & 0_{1\times3} & 0_{1\times3} & 0_{1\times2} & 0_{1\times2} & 0 & 0 & 0 & 0 \\
0_{1\times3} & 0_{1\times3} & 0_{1\times3} & 0_{1\times2} & 0_{1\times2} & 0 & 0 & 0 & 0 \\
0_{1\times3} & 0_{1\times3} & 0_{1\times3} & 0_{1\times2} & 0_{1\times2} & 0 & 0 & 0 & 0
\end{bmatrix}
\begin{bmatrix}
\delta\underline{q} \\ \delta\underline{\omega}_P \\ \delta\underline{\tau}_P \\ \delta\underline{\psi} \\ \delta\dot{\underline{\psi}} \\ \delta\nu_n \\ \delta\dot{\nu}_n \\ \delta\Delta \\ \delta\psi_3
\end{bmatrix}
\tag{33}
$$

and the sub-matrices in the linearised system in (33) are given as follows:-

$$
\begin{aligned}
F_A &= [[\hat{T}_{BP}\hat{\underline{\omega}}_P]] \\
F_B &= \frac{1}{2}\hat{T}_{BP} \\
F_C &= \frac{1}{2}\left[\left(\frac{\partial \hat{T}_{BP}}{\partial \hat{\psi}_1}\right)\hat{\underline{\omega}}_P \left(\frac{\partial \hat{T}_{BP}}{\partial \hat{\psi}_2}\right)\hat{\underline{\omega}}_P\right] \\
F_D &= \frac{1}{2}\left(\frac{\partial \hat{T}_{BP}}{\partial \hat{\psi}_3}\right)\hat{\underline{\omega}}_P \\
F_E &= J_P^{-1}(\hat{\nu}_n, \hat{\Delta})([[\hat{\underline{\omega}}_P]]J_P(\hat{\nu}_n, \hat{\Delta}) - [[J_P(\hat{\nu}_n, \hat{\Delta})\hat{\underline{\omega}}_P]]) \\
F_F &= J_P^{-1}(\hat{\nu}_n, \hat{\Delta}) \\
F_G &= \frac{\partial f_\omega}{\partial \nu_n} = \frac{\partial f_\omega}{\partial J_2}\cdot\frac{\partial J_2}{\partial \nu_n} + \frac{\partial f_\omega}{\partial J_3}\cdot\frac{\partial J_3}{\partial \nu_n} \\
F_H &= \frac{\partial f_\omega}{\partial \Delta} = \frac{\partial f_\omega}{\partial J_2}\cdot\frac{\partial J_2}{\partial \Delta} + \frac{\partial f_\omega}{\partial J_3}\cdot\frac{\partial J_3}{\partial \Delta} \\
F_I &= -[[\hat{\underline{\tau}}_P]] \\
F_J &= [[\hat{\underline{\omega}}_P]]
\end{aligned}
\tag{34}
$$

The analytical expressions for the above partial derivatives are derived in Appendix B.2.

2.7.2 Measurement Model

The measurement model uses exactly the same as that presented in Section 2.4.2.

The linearised measurement equation in terms of the vector part of the error quaternion defined in (4) is then given by:-

$$
\delta\underline{q}_{STR} = H\left[\delta\underline{q}\ \delta\underline{\omega}_P\ \delta\underline{\tau}_P\ \delta\underline{\psi}\ \delta\underline{\dot{\psi}}\ \delta\nu_n\ \delta\dot{\nu}_n\ \delta\Delta\ \delta\psi_3\right]^T + \delta\underline{\nu} = \delta\underline{q} + \delta\underline{\nu} \tag{35}
$$

where

$$
H = \left[H_q\ H_\omega\ H_\tau\ H_\psi\ H_{\dot{\psi}}\ H_{\nu_n}\ H_{\dot{\nu}_n}\ H_\Delta\ H_{\psi_3}\right] = \left[I_3\ 0_{3\times 14}\right] \tag{36}
$$

3 Algorithm End-to-End Testing with Simulated Data

This chapter describes the approach used for the end-to-end testing of the current filtering algorithm, that is used within the operational AHF generation software. The Planck HPTDG was used to generate the required telemetry data for all end-to-end testing and the "real world" attitude data from its output "dynamics.dat" were used for the final comparison with filtered attitude data. For a restricted number of slews in HCM and pointings in SCM, the STR-Dynamic model based filtering algorithms, that can be used to filter data during nominal HCM reorientation slews and SCM pointings, have also tested using this approach. An assessment of the STR-FOG based filtering algorithm was not possible since the HPTDG does not incorporate a model of the FOG.

The results presented for the new STR-Dynamic model filtering algorithm (SCM), clearly show the improvements made when compared to the current filter, in particular with respect to the efficiency of STR spatial biases filtering. Also analysed are the effects of introducing different types of time varying star tracker alignments.

Also presented are the performances of the current and new STR-Dynamic model based filtering algorithms, used for spacecraft inertia tensor estimation.

3.1 High Precision Test Data Generator

The Planck HPTDG gives a precise simulation of the Planck ACMS and environment and can be used to generate representative ACMS telemetry in response to telecommanding. The core components of the test data generator are listed as follows:-

- Top level control function to process and schedule ACMS command sequences provided by the Planck MPS sub-system.
- Spacecraft Dynamic Model including a comprehensive model of the external environmental solar radiation pressure disturbance torques as well as torques generated by the Helium venting. The spacecraft dynamics are modelled as a rigid body with a slowly varying inertia tensor resulting from the depletion of fuel.
- A comprehensive model of the STR, derived mainly from the industry model described in [18] and [19], with the basic functionality listed as follows:-
    - Use of attitude and Planck STR on-board star catalogue to provide an STR FOV extract.
    - Generate measured star positions in the STR frame using the attitude to transform the inertial directions to stars within the STR FOV.
    - Add biases and noises to each star coordinate. The requirements listed in Chapter 5 of [18] that have been modelled are listed as follows:-
        - SIM-STR-341 and 342
        - SIM-STR-345 and 346
        - SIM-STR-347, 348 and 349
    - With the measured and catalogued star positions, use the Davenport algorithm or Q method (Section 12.2.3 of [20]) to estimate the attitude quaternion, from which the angular rates can be derived through numerical differentiation.
    - Compute a time label for the attitude quaternion with an accuracy of ±0.1 ms
- A comprehensive model of the 1N thrusters which are used to reorient the spacecraft when the spacecraft is in HCM mode.
- The actual ACC ASW code is integrated into the simulator, together with essential parts of the BSW code, where aspects related to the 1553 communications have been modified.
- Generation of log files that contain the true spacecraft attitude and angular rates as a function of time.
- Generation of all relevant ACC essential housekeeping, ACMS mode specific and diagnostic packets.
- Generation of time correlation packets.

The approach used to completely end-to-end test the various algorithms is listed as follows:-

- The operational mission planning products (APPL/APF) for OD 0390 were processed by TVA to generate the required input ACMS command sequences to be executed using the Planck HPTDG.
- Use the Planck TM access subsystem to retrieve the ACMS housekeeping and diagnostic telemetry generated by the HPTDG.

- Use the AHF generation software to generate the AHF products
- Use pre-processing script to extract stable pointing phase data from the high frequency records of the AHF and store the data for each pointing ID in a dedicated ASCII file.
- Use pre-processing script to extract stable pointing phase data from the "dynamics.dat" file produced by the HPTDG
- Use a MATLAB script to do a full comparison between the data in the "dynamics.dat" file and the pointing products extracted from the AHF and produce plots for the 3-axes errors between the 2 data sets as a function of time. Also provided are histograms of the 3 axes errors.
- Compute the statistics of the 3 axes errors for each pointing.

3.2 AHF Filtering Algorithm Testing

This section presents the results of the comparison between the current AHF filtering algorithm and the new STR dynamic model based filtering algorithm with the HPTDG 'dynamics.dat'.

Table 1 summarises the AME requirements and goal requirements from [21]. Table 2 below shows the 3 axes pointing reconstruction errors for all pointings in OD 0390, which show a very good performance in comparison to Table 1 .

	Requirements (arcsec)	Goals (arcsec)
LOS	28.8	9.6
ALOS	60.0	-

TABLE 1: ACMS AME Specifications

Pointing ID	Mean Error (arcsec)			Standard Deviation (arcsec)		
	X-axis	Y-axis	Z-axis	X-axis	Y-axis	Z-axis
02097460	-0.464	0.015	0.077	0.277	0.354	1.381
02097470	-0.420	-0.006	-0.029	0.276	0.414	1.337
02097480	-0.408	0.021	0.235	0.257	0.360	1.274
02097490	-0.430	-0.014	0.019	0.294	0.395	1.432
02097500	-0.437	-0.002	-0.065	0.285	0.446	1.415
02097510	-0.428	-0.017	-0.099	0.276	0.357	1.389
02097520	-0.449	-0.006	-0.032	0.290	0.456	1.322
02097530	-0.433	-0.002	0.064	0.276	0.424	1.430
02097540	-0.418	-0.005	0.042	0.289	0.396	1.413
02097550	-0.461	0.016	-0.035	0.294	0.446	1.337
02097560	-0.448	-0.018	-0.035	0.286	0.391	1.430
02097570	-0.422	-0.001	0.078	0.281	0.414	1.336
02097580	-0.455	-0.011	-0.157	0.273	0.345	1.369
02097590	-0.462	0.004	-0.044	0.261	0.404	1.330
02097600	-0.437	0.002	0.113	0.285	0.407	1.490
02097610	-0.424	0.003	-0.115	0.285	0.351	1.455
02097620	-0.440	0.002	0.086	0.300	0.346	1.431
02097630	-0.434	0.003	-0.024	0.284	0.371	1.364
02097640	-0.455	0.020	-0.159	0.282	0.423	1.478
02097650	-0.398	-0.011	0.106	0.287	0.417	1.548

TABLE 2: Pointing error statistics for current AHF filtering algorithm

Pointing ID	Mean Error (arcsec)			Standard Deviation (arcsec)		
	X-axis	Y-axis	Z-axis	X-axis	Y-axis	Z-axis
02097660	-0.430	-0.024	0.201	0.295	0.358	1.420
02097670	-0.431	-0.010	-0.008	0.284	0.417	1.409

TABLE 2: Pointing error statistics for current AHF filtering algorithm

The comparison of the filtered quaternions, $\underset{\sim}{q}_{filter}$, and the actual quaternions from the HPTDG "dynamics.dat" data, $\underset{\sim}{q}_{hptdg}$, is made by computing the error quaternion. From this error quaternion, the Euler angles can be computed using a small angle approximation. This can be expressed as follows:-

$$\delta\underset{\sim}{q} = \underset{\sim}{q}_{filter} \otimes \hat{\underset{\sim}{q}}^{-1}_{hptdg} = \begin{bmatrix} \delta\underline{q} \\ \delta q_4 \end{bmatrix} = \begin{bmatrix} \frac{1}{2}\delta\underline{\theta} \\ \delta q_4 \end{bmatrix}, \delta\underline{\theta} = \begin{bmatrix} \delta\theta_x \\ \delta\theta_y \\ \delta\theta_z \end{bmatrix} \tag{37}$$

For the current AHF filtering algorithm, the errors, $\delta\underline{\theta}$, are shown in Figure 5 of Section 3.2.1 and the histograms for these errors are shown in Figure 6 of Section 3.2.1. The PSDs of the errors in Figure 5 are shown in Figure 7 of Section 3.2.1.

As can be seen from these plots, there are still some residual attitude measurement errors after filtering, which can be attributed to the star tracker spatial biases.

Similarly, the new STR Dynamic Model based filter described in Section 2.6 was used to filter the same data. The errors for this case are shown in Figure 11 of Section 3.2.2 and the histograms for these errors are shown in Figure 12 of Section 3.2.2. The results of the comparison with the current AHF filtering algorithm are shown in Figure 13 of Section 3.2.2 and the corresponding PSDs of these errors are shown in Figure 14 of Section 3.2.2. The errors in Figure 13 are practically the same as the results shown in Figure 5. This means that the new filter provides a more accurate representation of the true spacecraft attitude.

These results clearly show how effective the new filter is at rejecting the STR spatial bias errors. There is a noticeable error on the transverse axes with spin and nutation frequency components. It is noted that the SCS internal disturbance states are not estimated in this case. Also that the nutation component in the error could potentially be removed by adding the nutation to spin rate ratio to the estimator state vector.

Finally, in order to see how the new filters respond to time varying thermal distortions of the STR alignment, 3 cases have been considered:-

1. A sinusoidal variation
2. An exponential rise/fall variation (one time constant)
3. An exponential rise/fall variation (two time constants)

The first 2 of these cases have been selected such that the variation is sufficiently high frequency in order to observe a periodic trend within a single pointing duration of typically 48 minutes. The third case adds a longer time constant variation to the first time constant whose periodic feature is not observable within a single pointing duration of typically 48 minutes.

For the first case, the injected alignment variation, the HPTDG "dynamics.dat" versus current filter, the HPTDG "dynamics.dat" versus new STR-dynamic model based filter and the new STR-dynamic model based filter versus current filter results are shown in Figures 2, 8, 15 and 16 respectively.

For the second case, the injected alignment variation, the HPTDG "dynamics.dat" versus current filter, the HPTDG "dynamics.dat" versus new STR-dynamic model based filter and the new STR-dynamic model based filter versus current filter results are shown in Figures 3, 9, 17 and 18 respectively.

For the third case, the injected alignment variation, the HPTDG "dynamics.dat" versus current filter, the HPTDG "dynamics.dat" versus new STR-dynamic model based filter and the new STR-dynamic model based filter versus current filter results are shown in Figures 4, 10, 19 and 20 respectively.

The main conclusions from these 3 cases is that alignment variations, where the period of the variation is less than the duration of the pointing, can be filtered by the new STR-dynamic model based filtering algorithm. Any low frequency variation like that injected during case 3 is not filtered as can be seen in the errors of Figure 19. In

order to deal with long term variations in the alignment in general, it would be necessary to detrend this data using other means prior to filtering the data.

Finally, results in Section 3.2.3 show the performance of the new STR-Dynamic Model based filter, described in Section 2.5, used to filter data during nominal re-orientation slews in HCM. The errors, $\delta\underline{\theta}$, are shown in Figure 21 and the histograms for these errors are shown in Figure 22. The actual times of the thruster pulses can be seen in the plot of the true spacecraft angular rates, which are shown in Figure 23. The main thing that affects the performance of this filter is the thruster torque estimation accuracy at the various steps in the HCM nominal re-orientation slew timeline (shown in Figure 1). This is particularly the case for the last thruster pulse of the manoeuvre sequence, where there are fewer attitude measurements compared to the other parts of the HCM timeline.

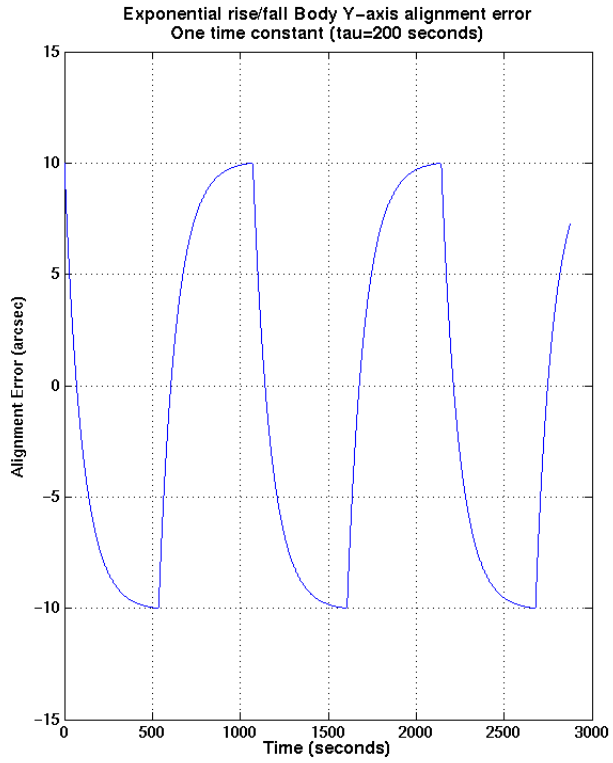

FIGURE 3: Body Y-axis exponential rise/fall alignment error on the STR (One time constant: τ=200 s)

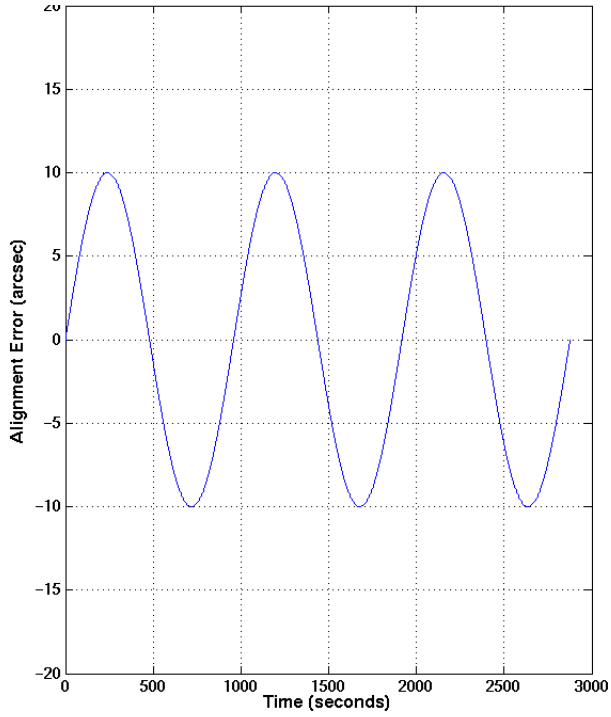

FIGURE 2: Body Y-axis sinusoidal alignment error on the STR

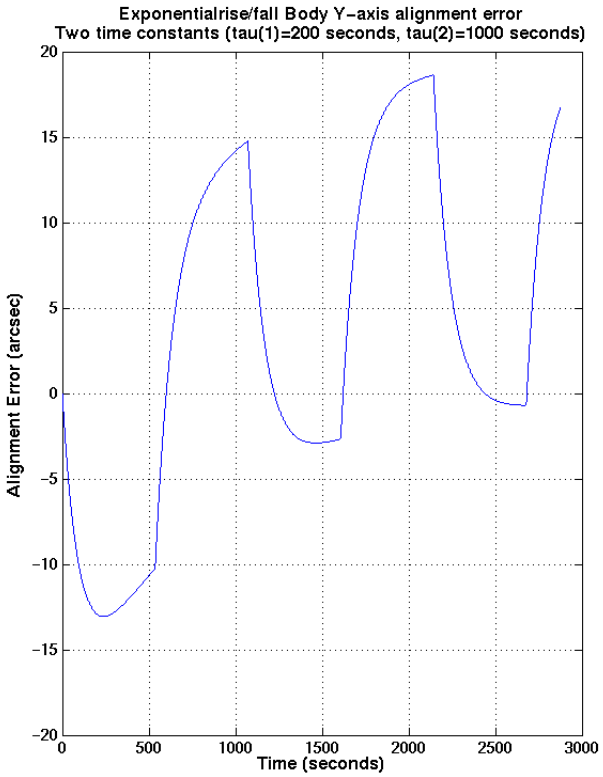

FIGURE 4: Body Y-axis exponential rise/fall alignment error on the STR (Two time constants: τ_1=200 s and τ_2=1000 s)

3.2.1 Current Filter Performance Assessment

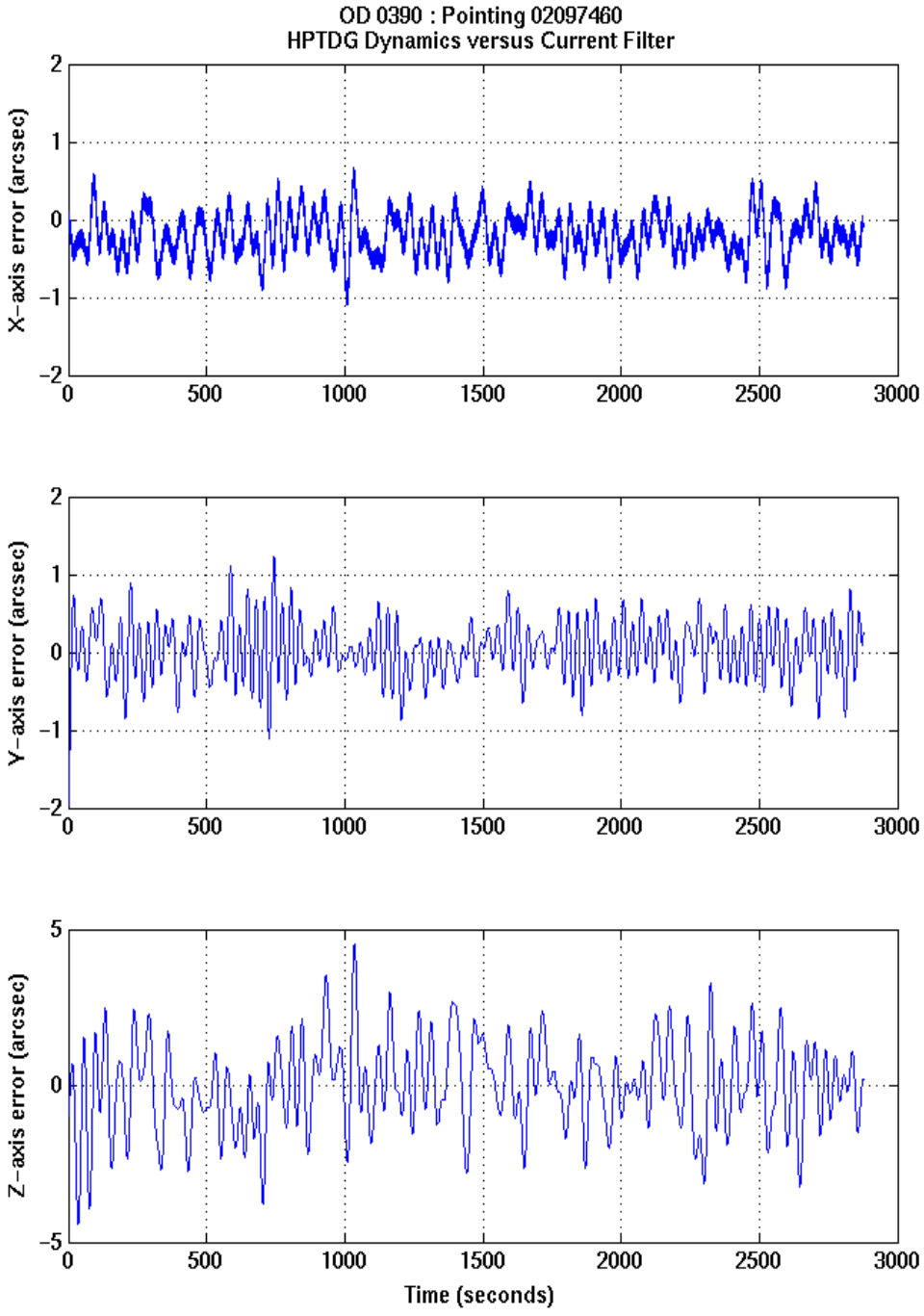

FIGURE 5: 3 axes errors of “dynamics.dat” and current AHF filter output comparison for SCM Pointing 02097460

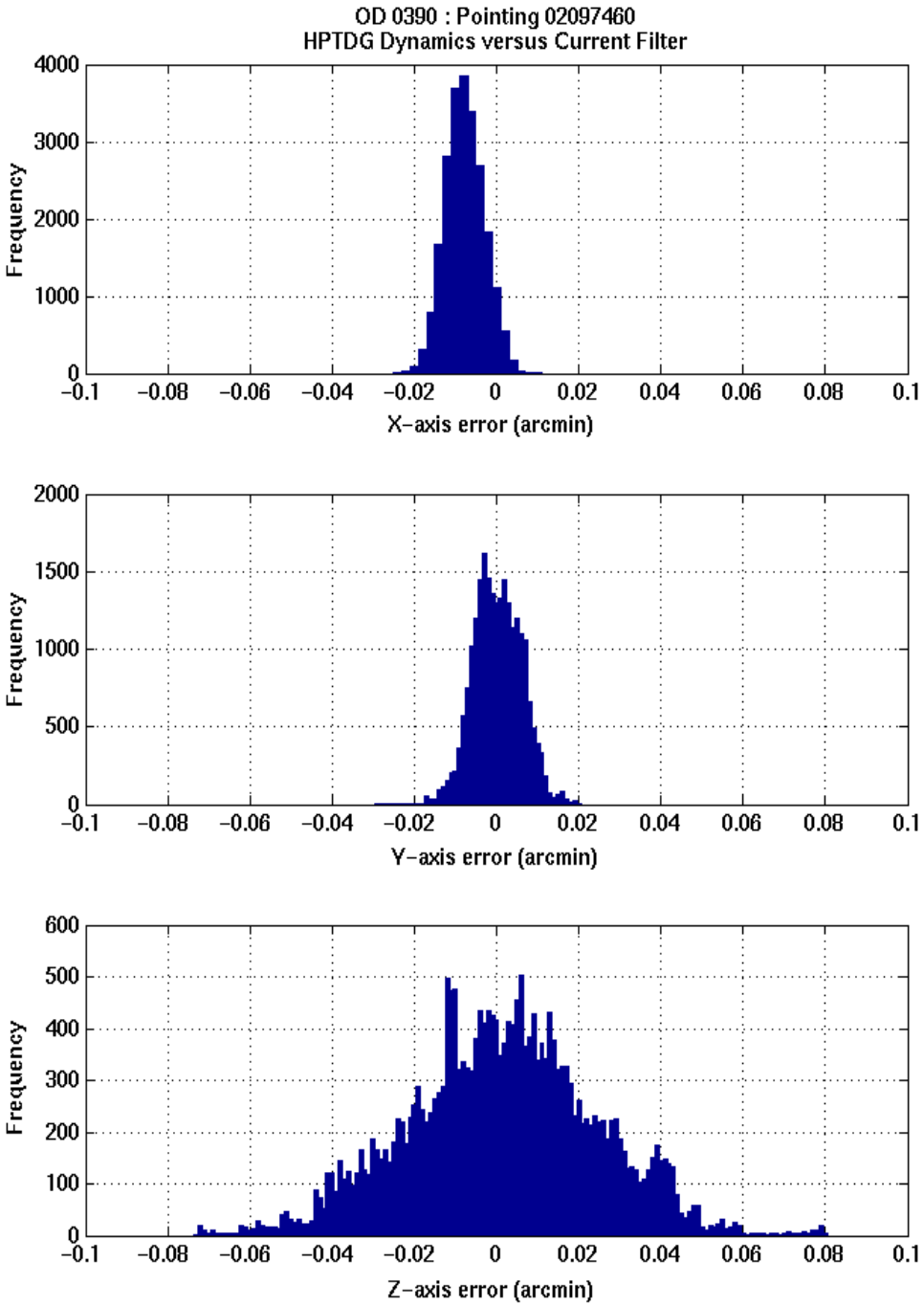

FIGURE 6: 3 axes errors of "dynamics.dat" and current AHF filter output comparison for SCM Pointing 02097460 (Histograms computed using data at 8 Hz with 100 bins)

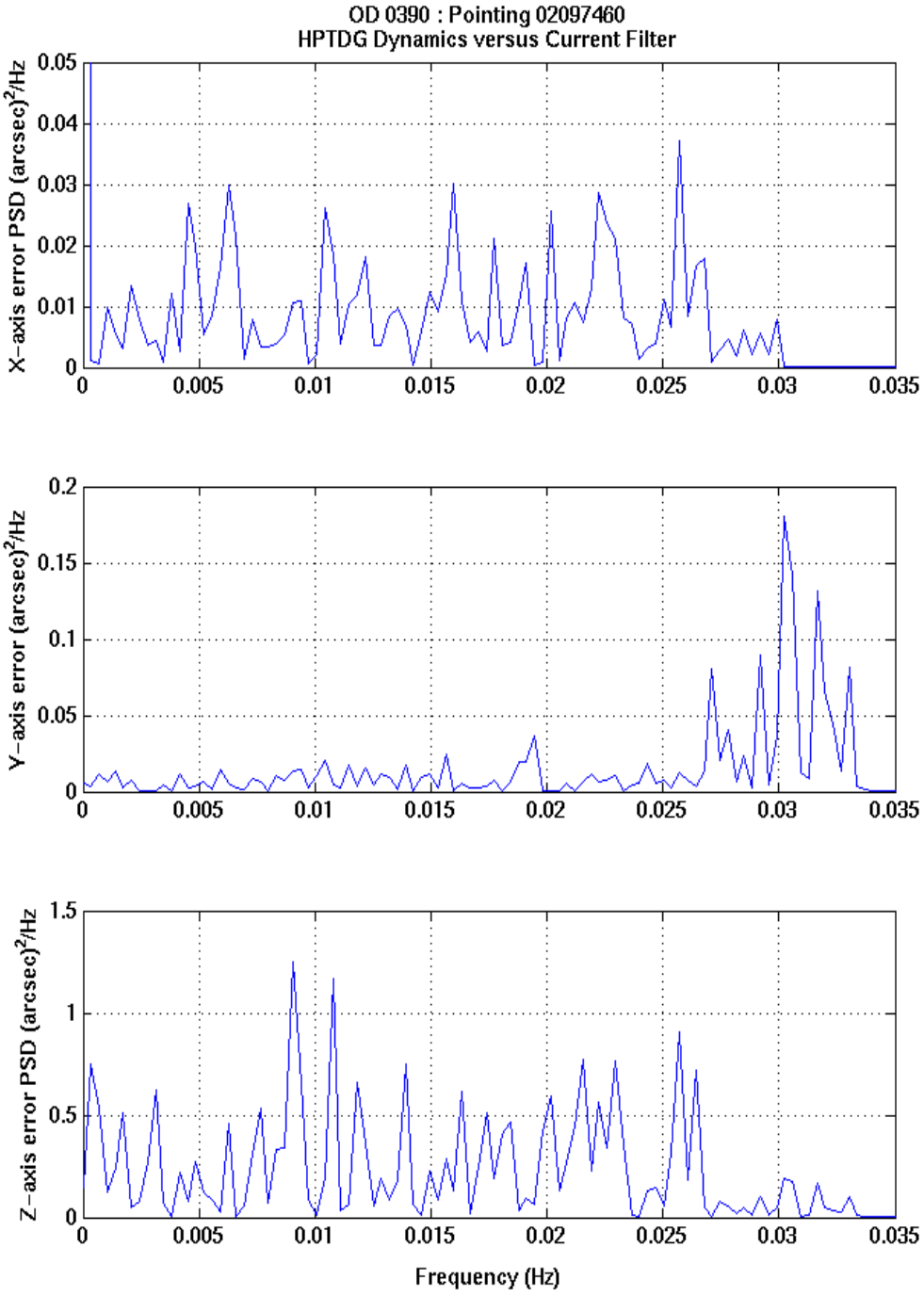

FIGURE 7: PSD of 3 axes errors of "dynamics.dat" and current AHF filter output comparison for SCM Pointing 02097460

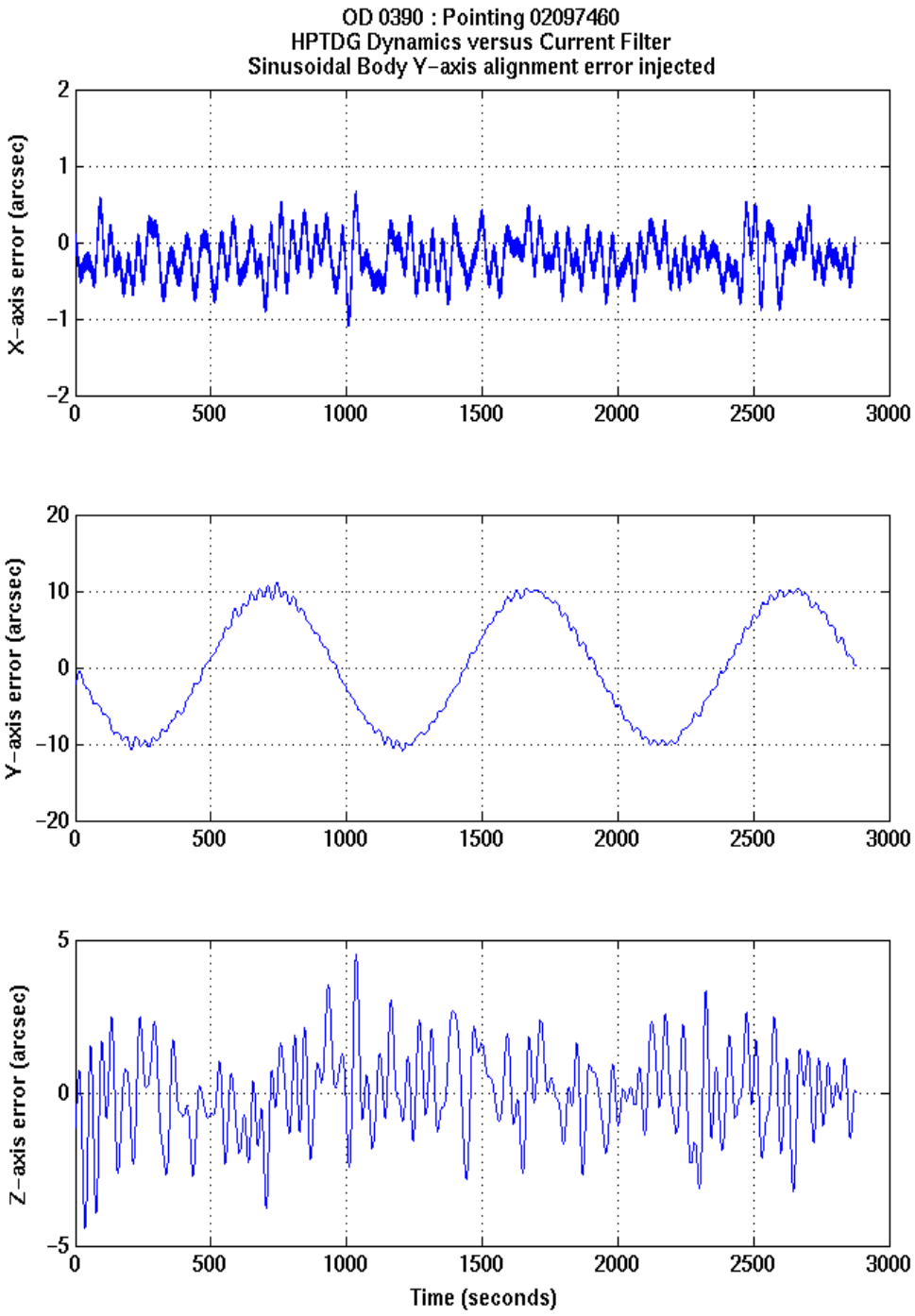

FIGURE 8: 3 axes errors of "dynamics.dat" and current filter output comparison for SCM Pointing 02097460: Body Y-axis sinusoidal alignment error on the STR

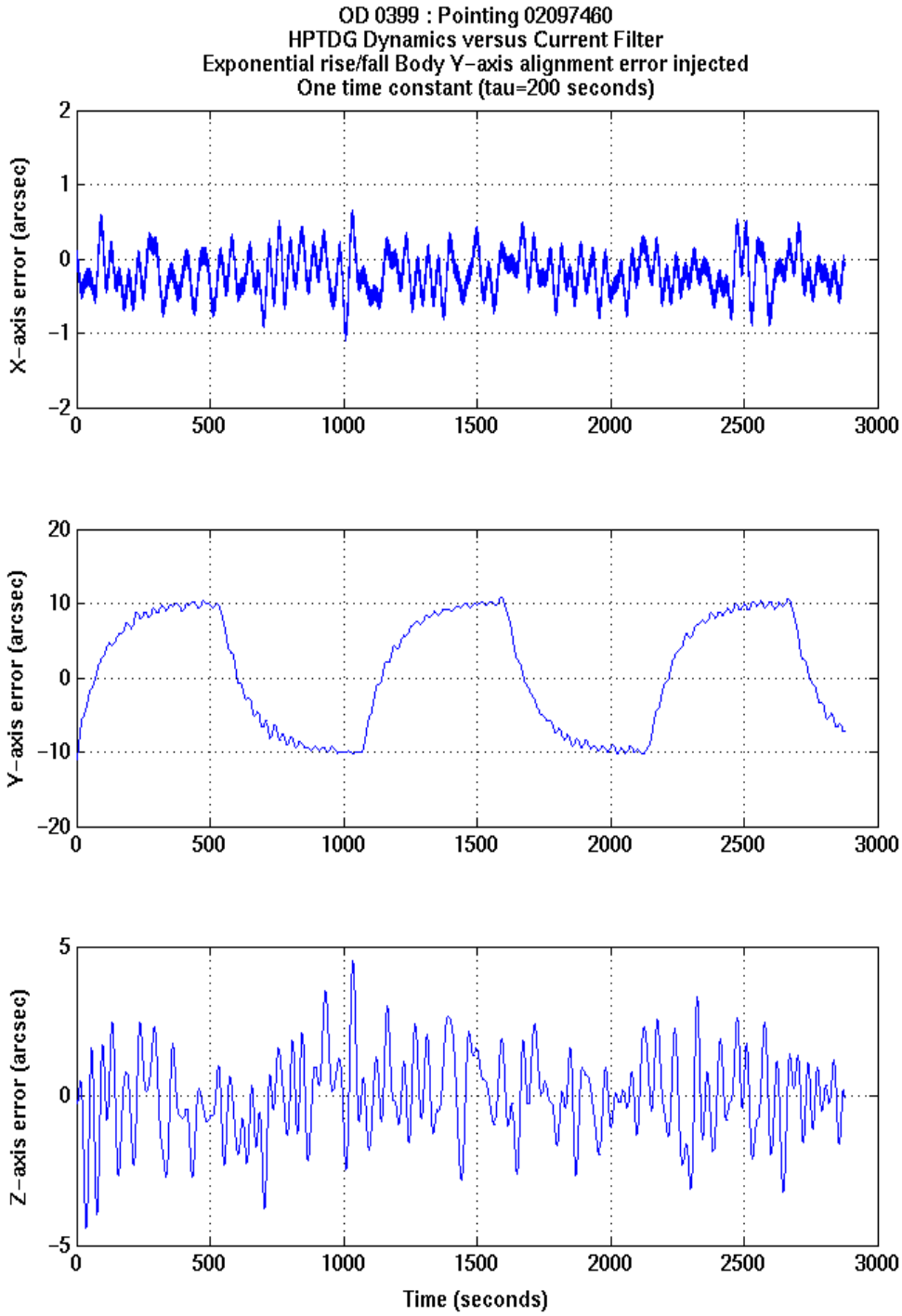

FIGURE 9: 3 axes errors of "dynamics.dat" and current filter output comparison for SCM Pointing 02097460: Body Y-axis exponential rise/fall alignment error on the STR (One time constant: τ=200 s)

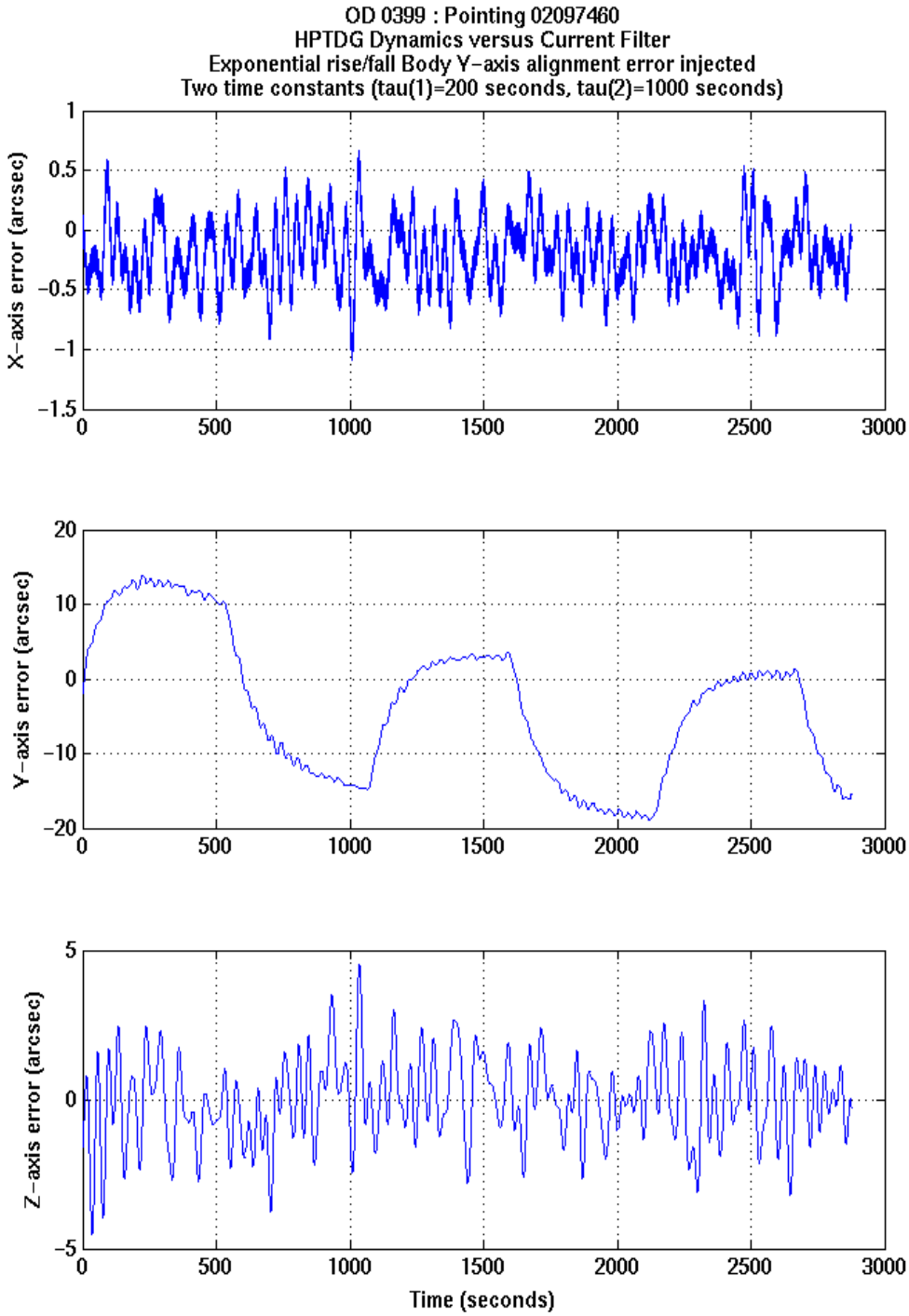

FIGURE 10: 3 axes errors of "dynamics.dat" and current filter output comparison for SCM Pointing 02097460: Body Y-axis exponential rise/fall alignment error on the STR (Two time constants: τ_1=200 s and τ_2=1000 s)

3.2.2 STR-Dynamic Model based Filter (SCM) Performance Assessment

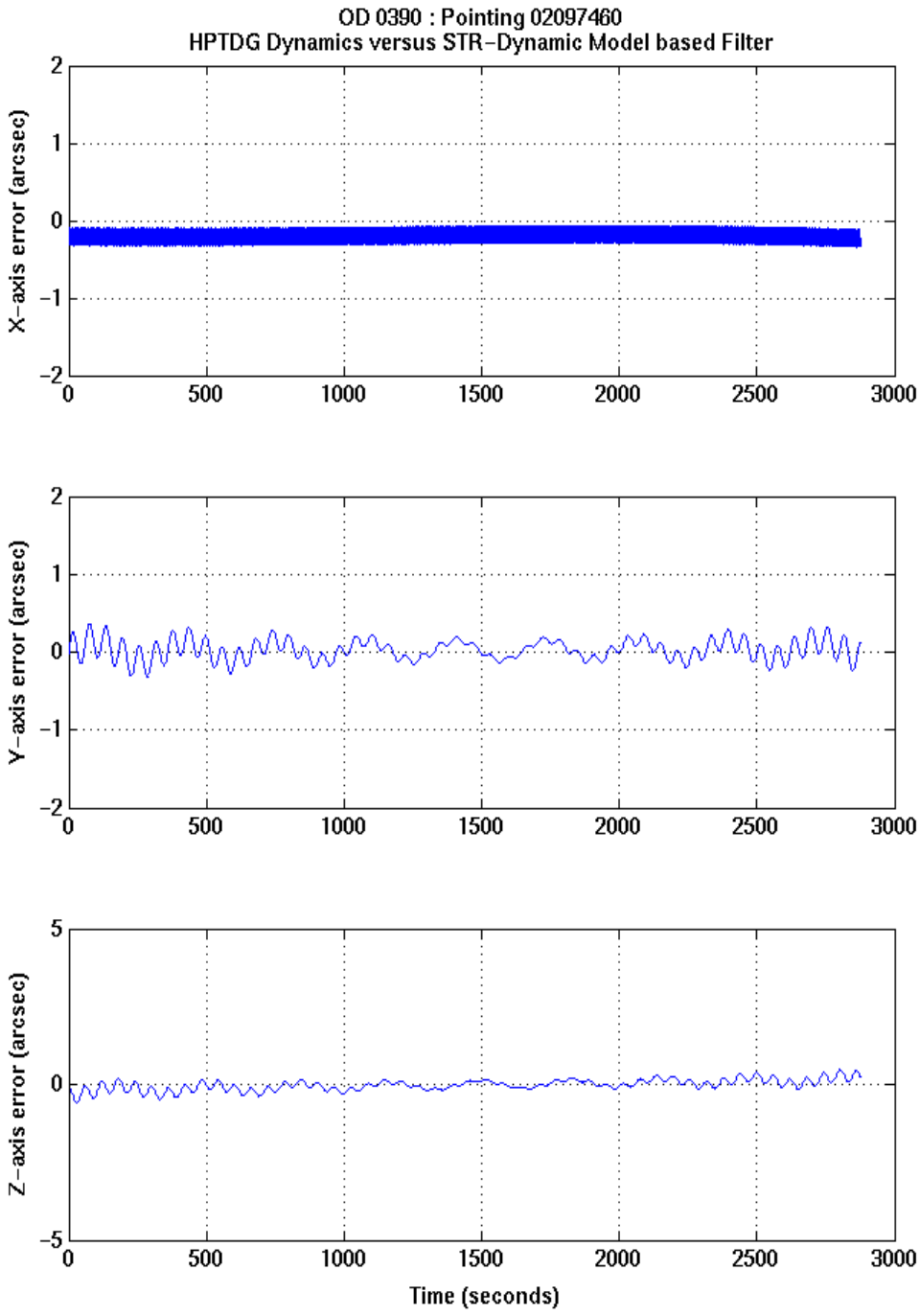

FIGURE 11: 3 axes errors of "dynamics.dat" and new STR-Dynamic Model based filter output comparison for SCM Pointing 02097460

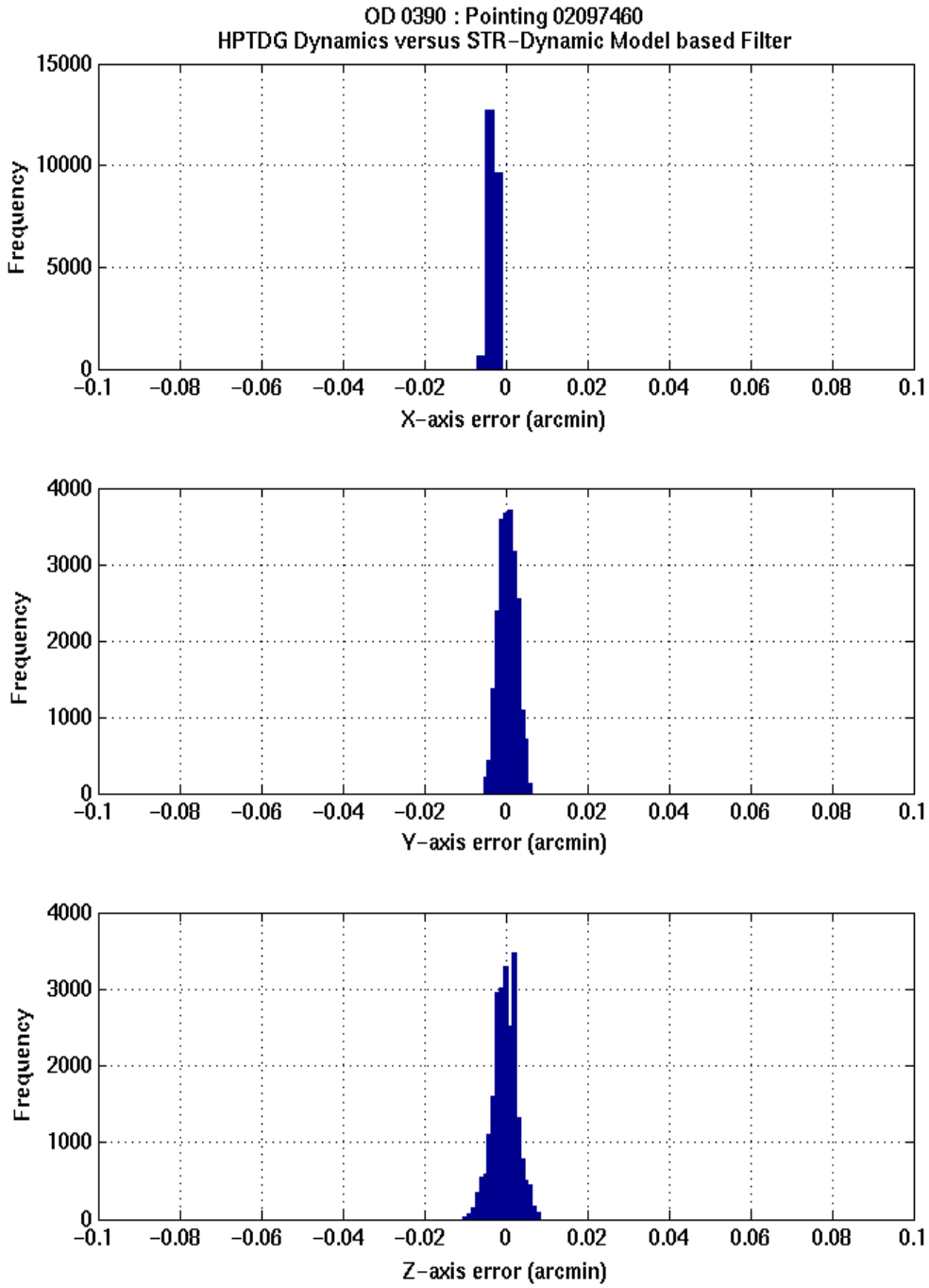

FIGURE 12: 3 axes errors of "dynamics.dat" and new STR-Dynamic Model based filter output comparison for SCM Pointing 02097460 (Histograms computed using data at 8 Hz with 100 bins)

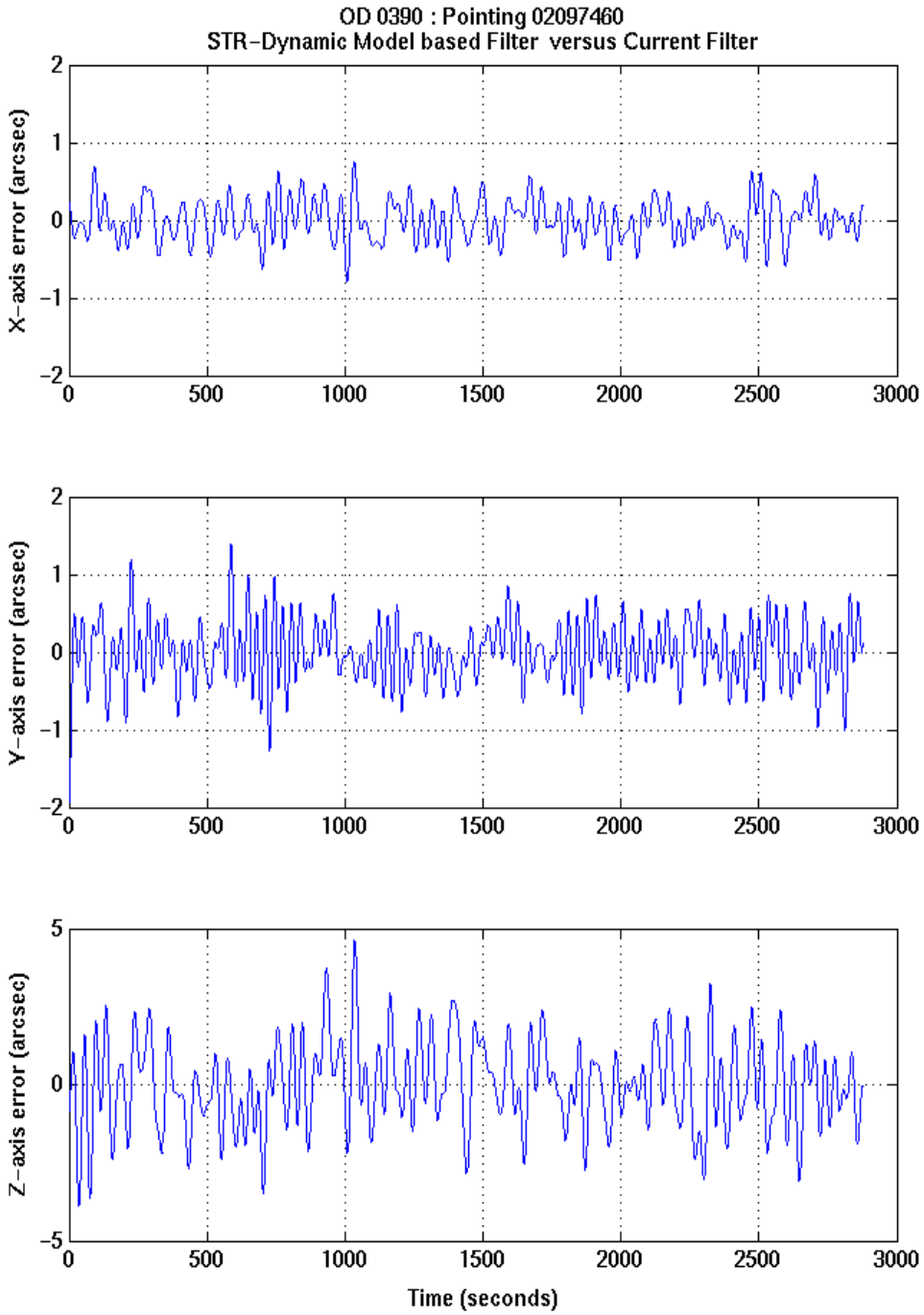

FIGURE 13: 3 axes errors of STR-Dynamic model based filter and current filter output comparison for SCM Pointing 02097460

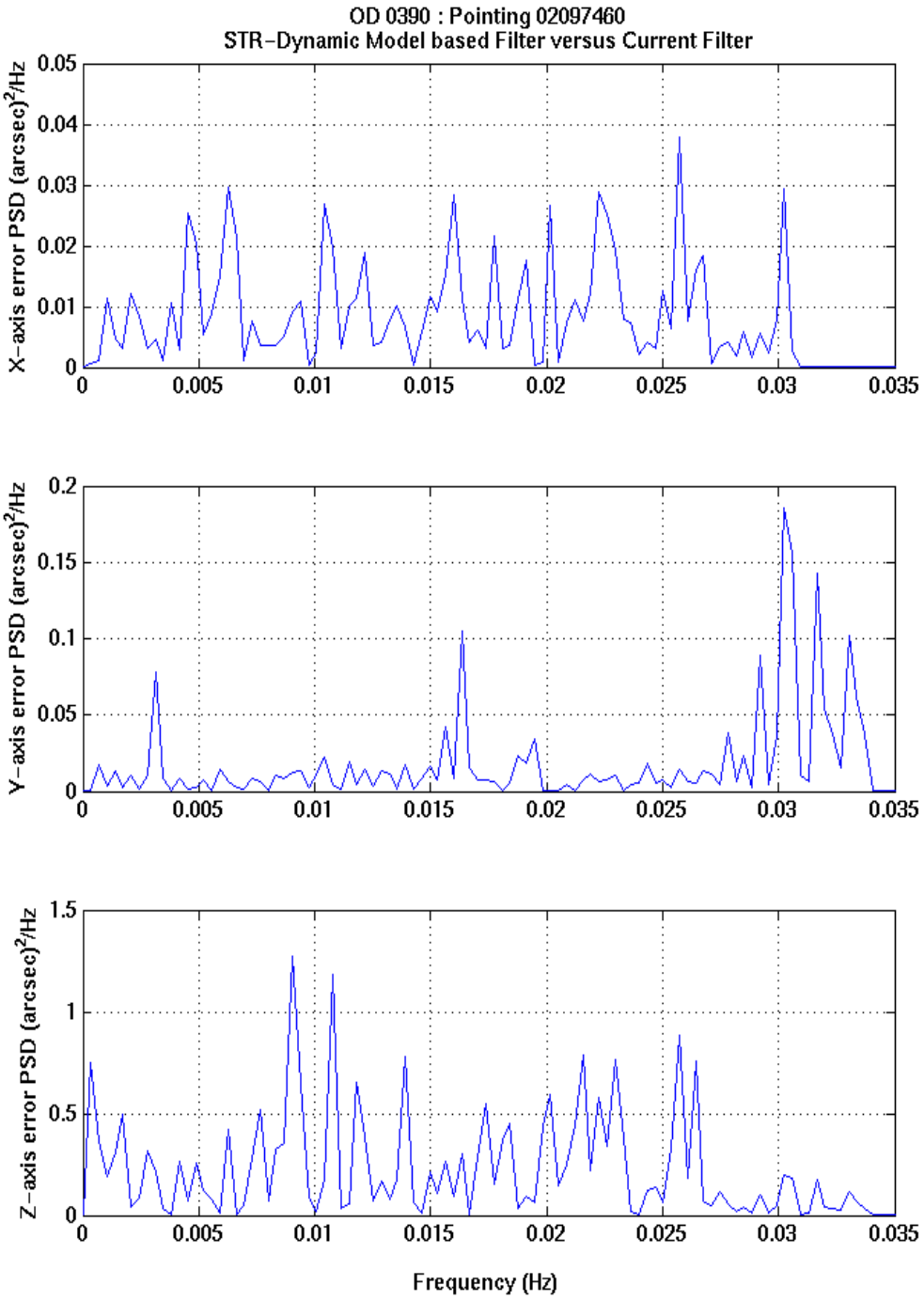

FIGURE 14: PSD of 3 axes errors of STR-Dynamic model based filter and current filter output comparison for SCM Pointing 02097460

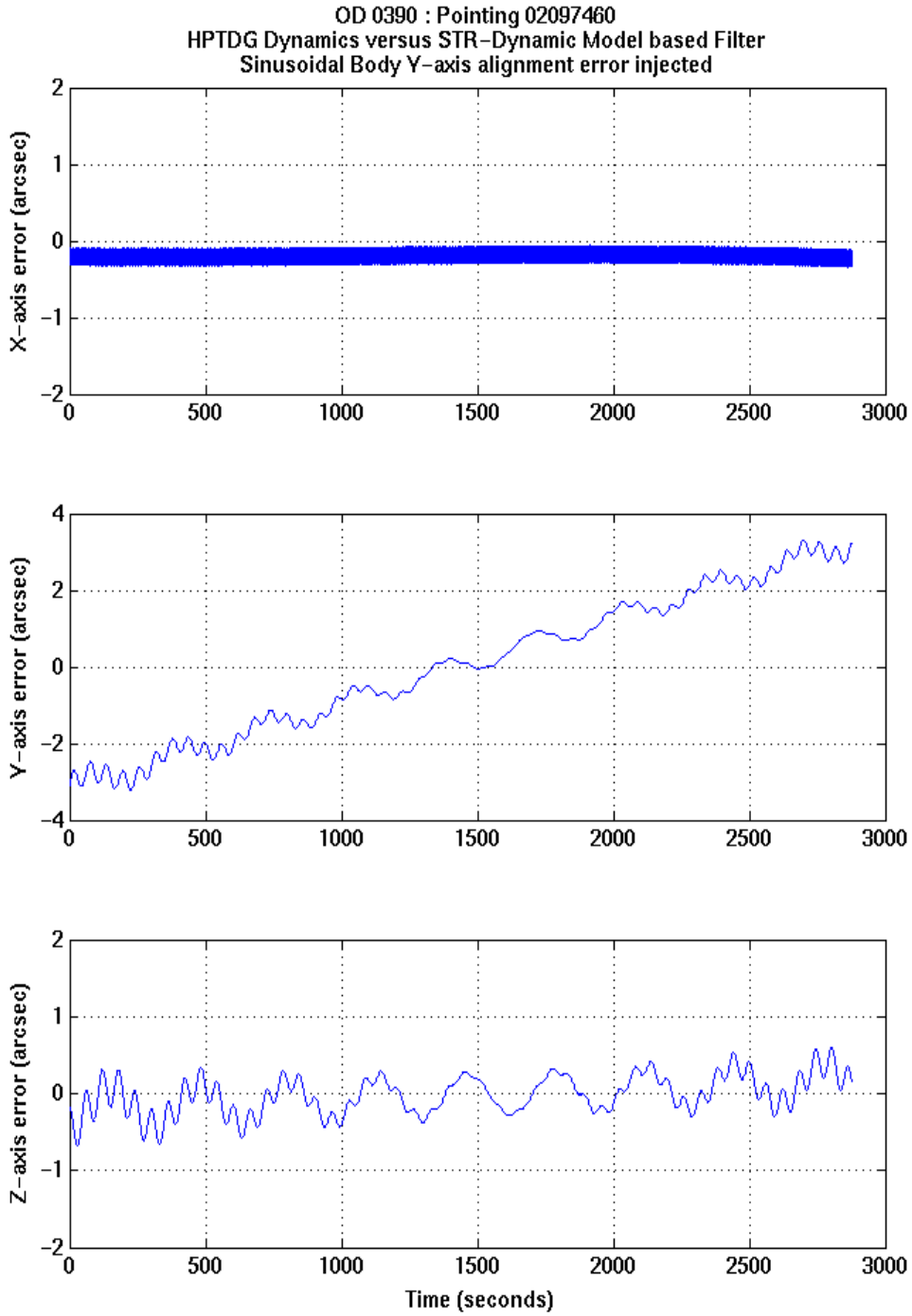

FIGURE 15: 3 axes errors of "dynamics.dat" and new STR-Dynamic Model based filter output comparison for SCM Pointing 02097460: Body Y-axis sinusoidal alignment error on the STR

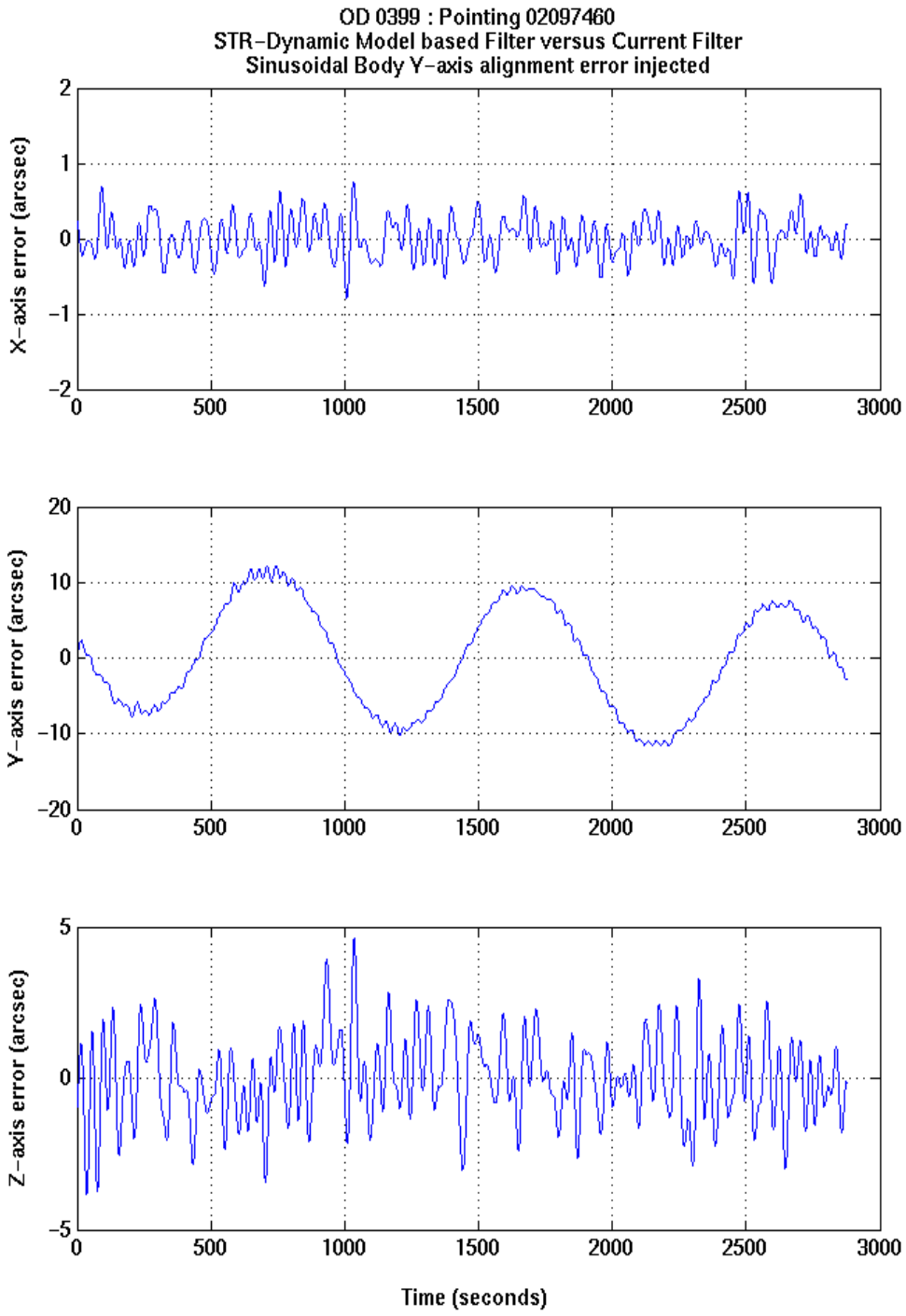

FIGURE 16: 3 axes errors of new STR-Dynamic Model based filter and current filter output comparison for SCM Pointing 02097460: Body Y-axis sinusoidal alignment error on the STR

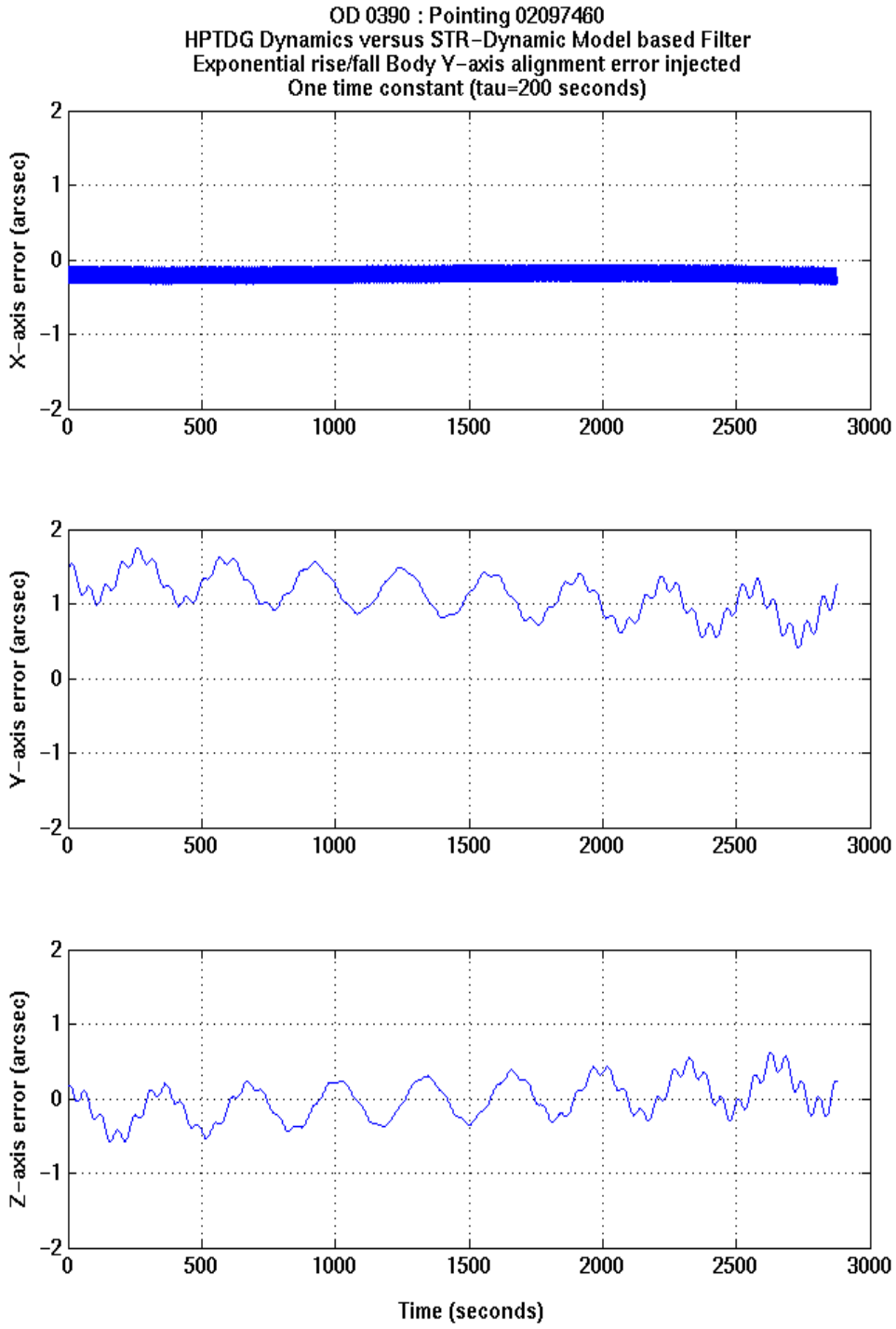

FIGURE 17: 3 axes errors of "dynamics.dat" and new STR-Dynamic Model based filter output comparison for SCM Pointing 02097460: Body Y-axis exponential rise/fall alignment error on the STR (One time constant: τ=200 s)

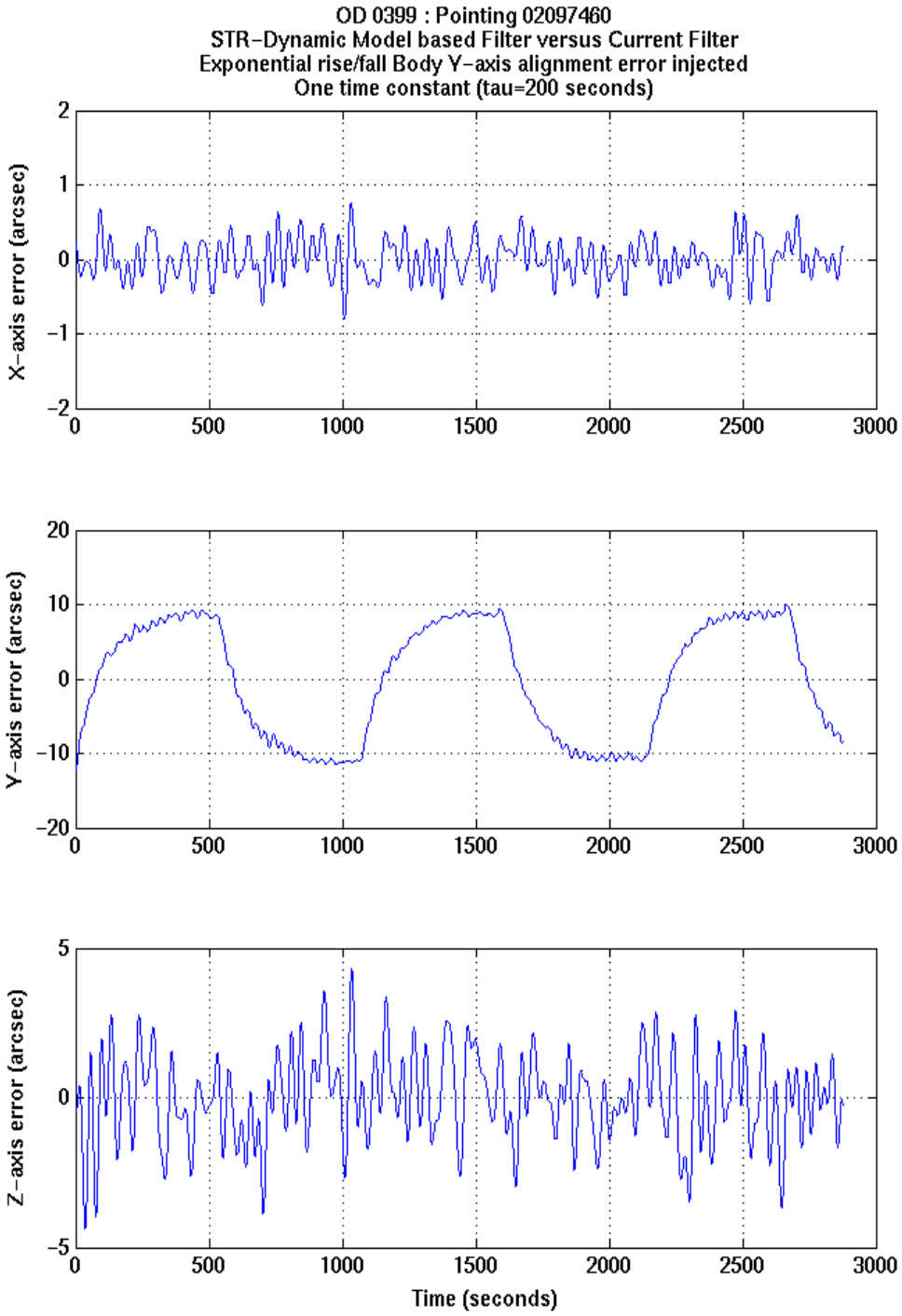

FIGURE 18: 3 axes errors of new STR-Dynamic Model based filter and current filter output comparison for SCM Pointing 02097460: Body Y-axis exponential rise/fall alignment error on the STR (One time constant: τ=200 s)

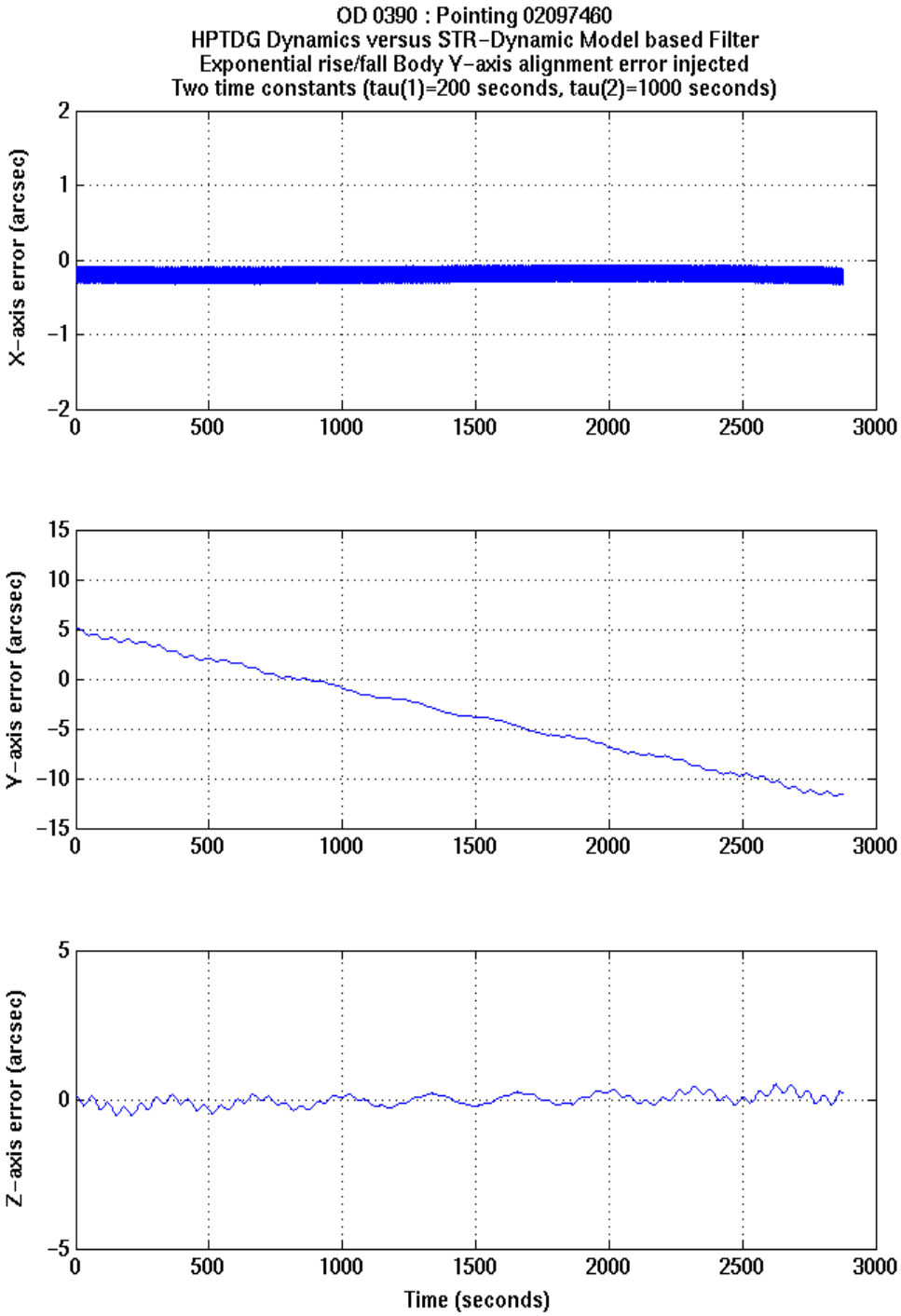

FIGURE 19: 3 axes errors of "dynamics.dat" and new STR-Dynamic Model based filter output comparison for SCM Pointing 02097460: Body Y-axis exponential rise/fall alignment error on the STR (Two time constants: τ_1=200 s and τ_2=1000 s)

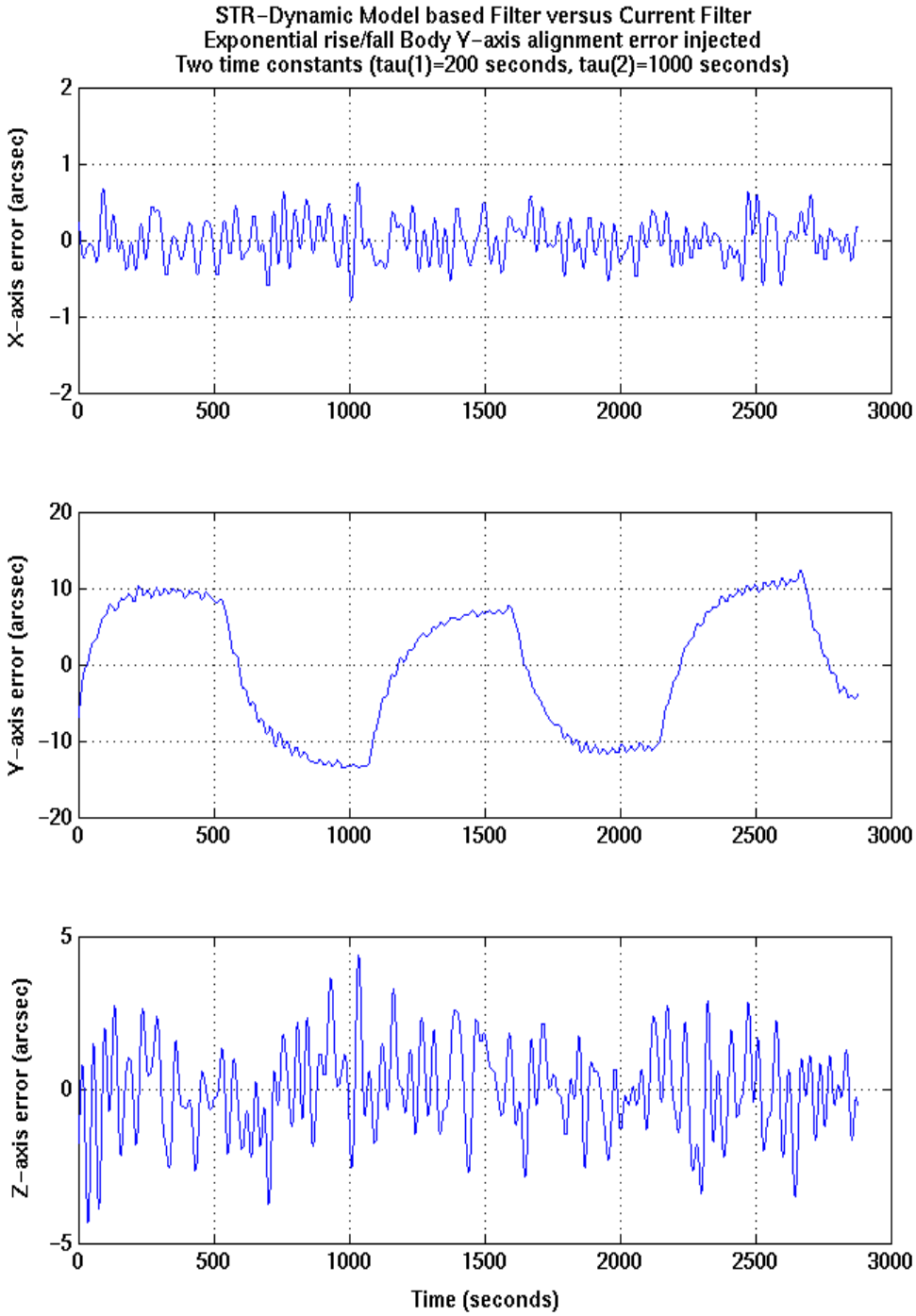

FIGURE 20: 3 axes errors of current filter and new STR-Dynamic Model based filter output comparison for SCM Pointing 02097460: Body Y-axis exponential rise/fall alignment error on the STR (Two time constants: τ_1=200 s and τ_2=1000 s)

3.2.3 STR-Dynamic Model based Filter (HCM) Performance Assessment

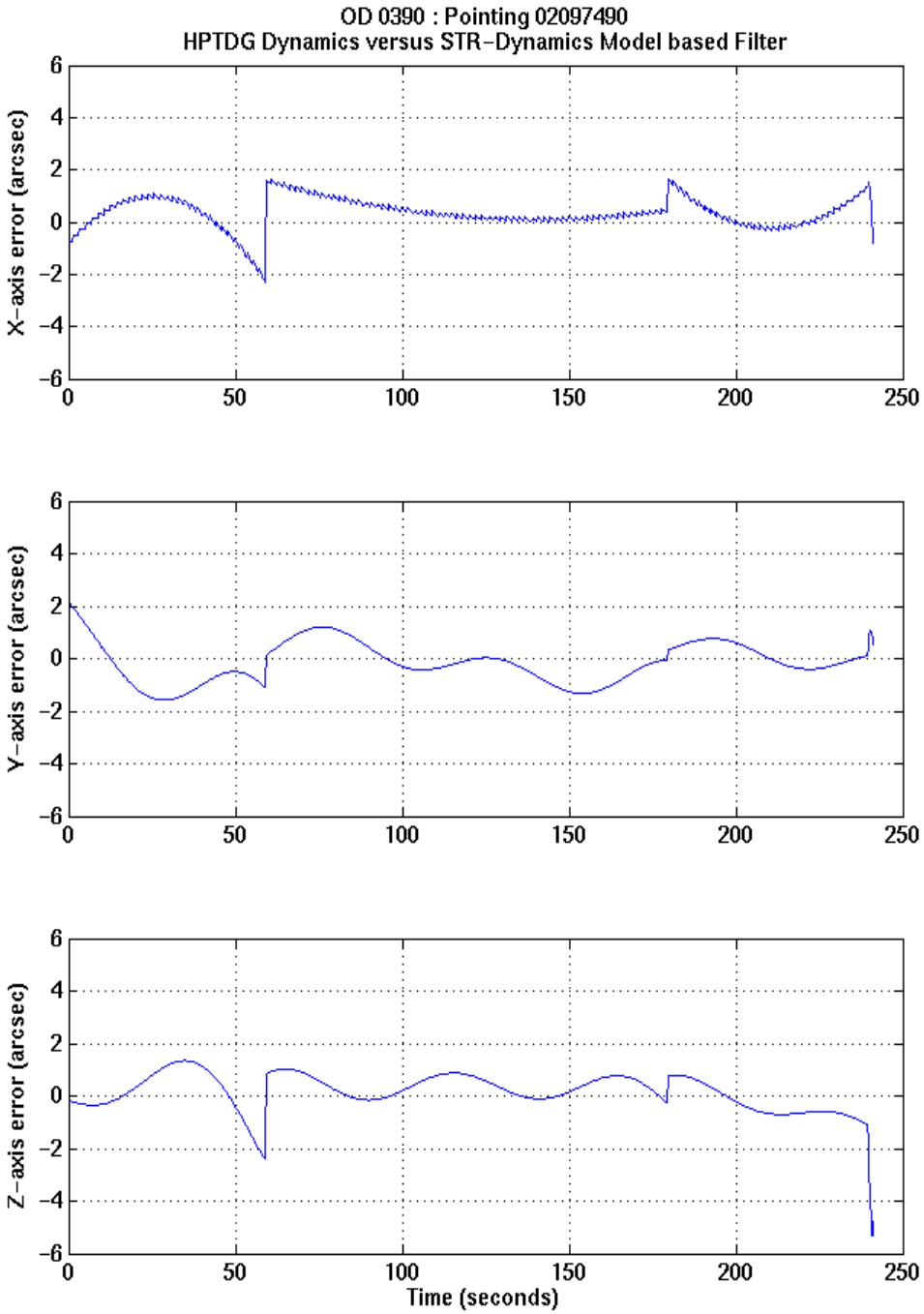

FIGURE 21: 3 axes errors of "dynamics.dat" and new STR-Dynamic Model based filter output comparison for nominal HCM Slew 02097490

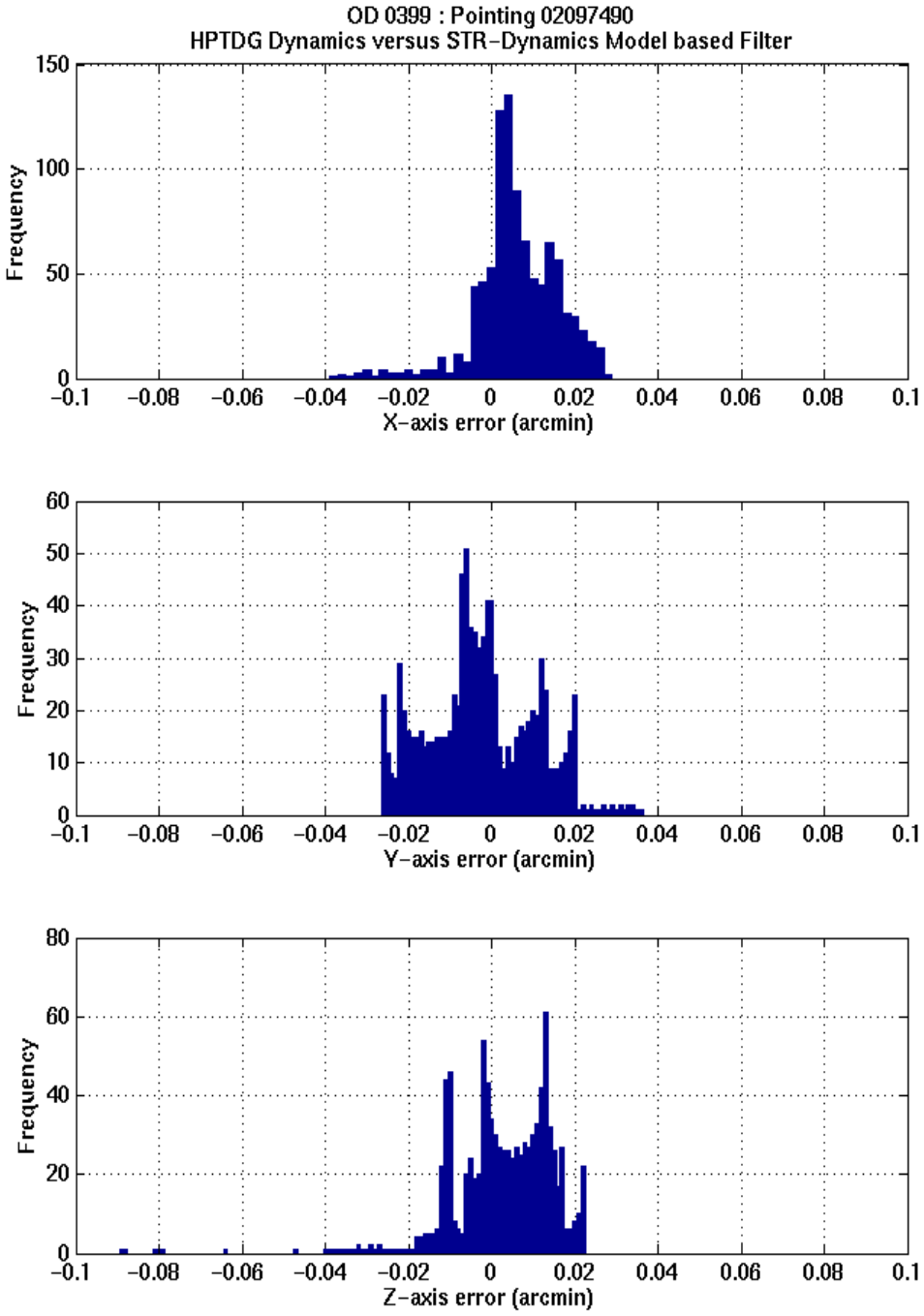

FIGURE 22: 3 axes errors of "dynamics.dat" and new STR-Dynamic Model based filter output comparison for nominal HCM Slew 02097490 (Histograms computed using data at 8 Hz with 100 bins)

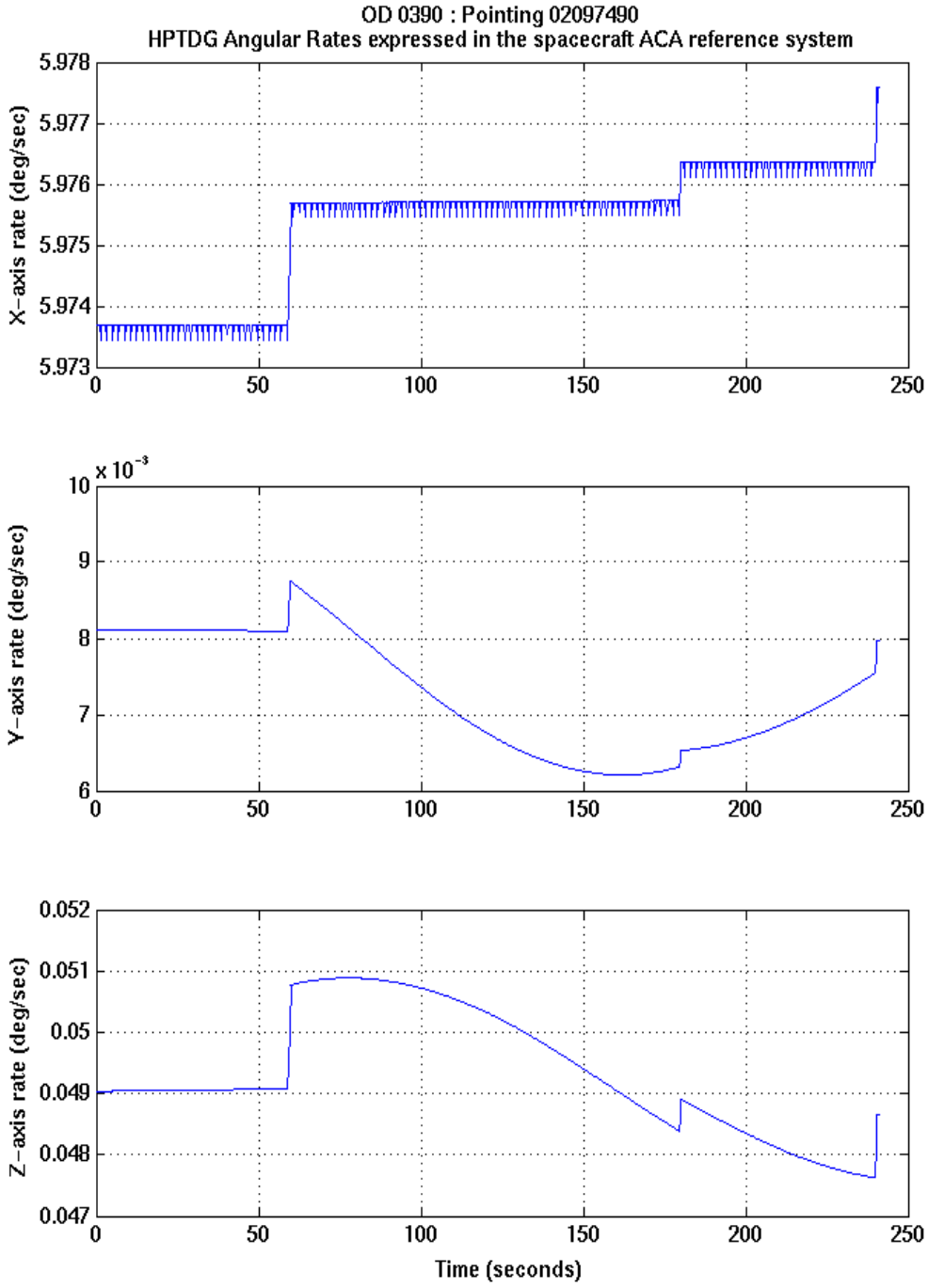

FIGURE 23: HPTDG Body angular rates for the nominal HCM reorientation slew 02097490
Note: The jitter in the upper figure is not representative of real dynamics.

3.3 Dynamic Model Based Inertia Tensor Estimation Algorithm Testing

This section presents the results of the end-to-end test of the current spacecraft inertia estimation algorithm described in Section 2.2 and the new algorithm described in Section 2.7. Three cases have been considered to test

these two algorithms, that correspond to various configurations of the transverse axes moments of inertia and are listed as follows:-

1. ($J_{yy} < J_{zz}$). 5 iterations to converge on final state estimates
2. ($J_{yy} > J_{zz}$). 4 iterations to converge on final state estimates
3. ($J_{yy} = J_{zz}$). 4 iterations to converge on final state estimates

The following tables present the actual mass properties simulated within the HPTDG as well as the values estimated by the current algorithm (Section 2.2) and the new STR-Dynamic Model based algorithm(Section 2.7).

There are no specific requirements on how accurately to estimate the spacecraft inertia tensor, but it is important to estimate it as accurately as possible. This is because it is used in the computations performed by the onboard attitude control laws in all ACMS modes. In particular orbit and attitude manoeuvres in OCM and routine scanning law attitude manoeuvres in HCM.

As can be seen in the following tables, the accuracy achieved in the parameter estimation is very good and comparable for both the current algorithm and the new estimation algorithm..

Parameter		HPTDG Simulated	Current Calibration Algorithm	New Calibration Algorithm
Principal Moments of Inertia	J_1 (kg m^2)	3114.541734	3114.541734	3114.541734
	J_2 (kg m^2)	2615.994489	2616.008219	2615.989437
	J_3 (kg m^2)	2654.122777	2654.132633	2654.117487
Nutation to Spin Ratio	ν_n (-)	0.181823847	0.181818582	0.181826169
Axial Imbalance	Δ (-)	-0.01710345	-0.01710156	-0.01710341
Principal Axis Tilt Angles	ψ_1 (arcmin)	-2.2344243	-2.2424724	-2.2425282
	ψ_2 (arcmin)	-13.6631194	-13.6600520	-13.660376
	ψ_3 (degree)	-31.7742616	-31.7836174	-31.7740864
Moments of Inertia	J_{xx} (kg m^2)	3114.534	3114.534	3114.534
	J_{yy} (kg m^2)	2626.567	2626.58523	2626.56178
	J_{zz} (kg m^2)	2643.558	2643.56335	2643.55288
	J_{xy} (kg m^2)	-0.385	-0.386119	-0.386139
	J_{xz} (kg m^2)	1.883	1.882599	1.882685
	J_{yz} (kg m^2)	17.067	17.068034	17.066838

TABLE 3: Inertia Tensor Calibration Testing: Case 1 ($J_{yy} < J_{zz}$)

Parameter		HPTDG Simulated	Current Calibration Algorithm	New Calibration Algorithm
Principal Moments of Inertia	J_1 (kg m^2)	3115.008396	3115.008396	3115.008396
	J_2 (kg m^2)	2654.722177	2655.192880	2654.710546
	J_3 (kg m^2)	2615.269427	2615.793789	2615.263774
Nutation to Spin Ratio	ν_n (-)	0.182019467	0.181796561	0.182023391
Axial Imbalance	Δ (-)	0.017701130	0.017670378	0.017698563

TABLE 4: Inertia Tensor Calibration Testing: Case 2 ($J_{yy} > J_{zz}$)

Parameter		HPTDG Simulated	Current Calibration Algorithm	New Calibration Algorithm
Principal Axis Tilt Angles	ψ_1 (arcmin)	-2.4212186	-2.4295119	-2.4295743
	ψ_2 (arcmin)	-13.9472990	-13.9446135	-13.9447474
	ψ_3 (degree)	29.7635233	29.7618034	29.7622415
Moments of Inertia	J_{xx} (kg m^2)	3115.0	3115.0	3115.0
	J_{yy} (kg m^2)	2645.0	2645.48495	2644.99060
	J_{zz} (kg m^2)	2625.0	2625.51011	2624.99211
	J_{xy} (kg m^2)	-0.4	-0.400682	-0.401124
	J_{xz} (kg m^2)	2.0	1.997572	1.999707
	J_{yz} (kg m^2)	17.0	16.976274	16.996972

TABLE 4: Inertia Tensor Calibration Testing: Case 2 ($J_{yy} > J_{zz}$)

Parameter		HPTDG Simulated	Current Calibration Algorithm	New Calibration Algorithm
Principal Moments of Inertia	J_1 (kg m^2)	3115.008472	3115.008472	3115.008472
	J_2 (kg m^2)	2646.997265	2647.038046	2646.993929
	J_3 (kg m^2)	2612.994263	2613.027635	2612.983693
Nutation to Spin Ratio	ν_n (-)	0.184306290	0.184289537	0.184309376
Axial Imbalance	Δ (-)	0.015313856	0.015316760	0.015317195
Principal Axis Tilt Angles	ψ_1 (arcmin)	-2.3411985	-2.3492251	-2.34928928
	ψ_2 (arcmin)	-14.0938843	-14.0909430	-14.0912065
	ψ_3 (degree)	44.9934013	44.9838540	44.9916636
Moments of Inertia	J_{xx} (kg m^2)	3115.0	3115.0	3115.0
	J_{yy} (kg m^2)	2630.0	2630.04275	2629.99408
	J_{zz} (kg m^2)	2630.0	2630.03140	2629.99201
	J_{xy} (kg m^2)	-0.4	-0.401104	-0.401147
	J_{xz} (kg m^2)	2.0	1.999499	1.999697
	J_{yz} (kg m^2)	17.0	17.003697	17.003612

TABLE 5: Inertia Tensor Calibration Testing: Case 3 ($J_{yy} = J_{zz}$)

4 Algorithm Testing with In-Flight Data

In this chapter a performance assessment of the new filters has been made, by comparing the results with those obtained with the current filter used to generate the AHF pipeline products. For the algorithms used to filter data during nominal slew manoeuvres in HCM, this comparison is made with the unfiltered data, because the current filter can not be used to filter data during slew manoeuvres.

In addition, results have been correlated with data from the thermal sub-system. After changes made to the thermal control, whereby certain heaters known to perturb the alignment of the operational star tracker, the attitude reconstruction performance has been significantly improved. However, there is still some uncertainty as to how much the FOG performances are affected by the thermal environment prior to the thermal controller updates, but there are indications that the FOG is not affected as much as the STR.

It is now understood that the current filter algorithm is sensitive to a number things, in particular low frequency thermal distortions where the frequencies are within the filter pass band. In addition, there are problems to detrend data, which is required prior to filtering, mainly due to the piecewise continuous nature of the attitude data at the instants of heater switching. The new filters are less sensitive to this and can also tolerate data outages[3] as well. However, they are sensitive to deficiencies in the fidelity of the prediction model, which could be circumvented by introducing a series of smaller batch intervals, where the batch size is chosen such that the unmodelled low frequency errors can be better tracked.

An assessment of both filtering algorithms described in Sections 2.4 and 2.6 has been made. In Section 4.1, results are shown for a single pointing in science mode (SCM) prior to the thermal controller updates and in Section 4.2, similar results are shown for a single pointing in SCM after the thermal controller updates were made. Results also show improvements when the SCS internal disturbances torques are estimated within dynamic model based filters.

In Section 4.3, results are shown for a nominal re-orientation slew in HCM, performed in OD 0561. The assessment of both filtering algorithms described in Sections 2.4 and 2.5 has been made, where a comparison of filtered data versus unfiltered data has been performed.

In Section 4.4, results are shown for a single pointing in OCM after the station keeping delta-V manoeuvre performed in OD 0247. This was prior to the thermal controller updates and in Section 4.5, similar results are shown for a single pointing in OCM after the station keeping delta-V manoeuvre performed in OD 0568. This was after the thermal controller updates were made.

The comparison of the filtered quaternions of the current filter, $\underline{q}_{current}$, and the new filter, $\underline{q}_{new}$, is made by computing the error quaternion, from which the Euler angles can be computed using a small angle approximation. This can be expressed as follows:-

$$\delta\underline{q} = \underline{q}_{current} \otimes \hat{\underline{q}}_{new}^{-1} = \begin{bmatrix} \delta\underline{q} \\ \delta q_4 \end{bmatrix} = \begin{bmatrix} \frac{1}{2}\delta\underline{\theta} \\ \delta q_4 \end{bmatrix}, \qquad \delta\underline{\theta} = \begin{bmatrix} \delta\theta_x \\ \delta\theta_y \\ \delta\theta_z \end{bmatrix} \tag{38}$$

4.1 Pre Thermal Control Updates - Science Mode Pointings

4.1.1 Fibre Optic Gyro Based Estimation Algorithm

The errors, $\delta\underline{\theta}$, are shown in below Figure 24 and the corresponding PSDs are shown in Figure 25. The PSDs show a modulation of the spin frequency with a low frequency term. The on-board filter estimates of the principal axis tilt angles, ψ_2 and ψ_1, with the non-zero offset subtracted, are shown in Figure 26. A comparison of the errors $\delta\theta_y$ and $\delta\theta_z$ in Figure 24 with the principal axis tilt angles ψ_2 and ψ_1 in Figure 26 shows a weak correlation. Therefore the low frequency alignment variations of the star tracker mounting are passed by the current filter, but they are partially rejected[4] by the new STR-FOG based filter. In order to quantify these effects, various examples with different alignment variations injected onto the measured STR attitude quaternion are shown, which clearly show which components are rejected. It is noted however that it is not possible to comment on how

3. Telemetry gap or star tracker falling out of tracking mode

much the FOG alignment and biases are affected by the thermal control, although as mentioned, it is not affected as much as the STR. Also it is not clear on how much the angle errors in Figure 24, are due to star tracker measurement errors. It is however clear from Figures 24 and 25, that spin frequency components are pre-dominant in the error angle plots of the STR-FOG based filter, which is less so in the case of the STR-dynamic model based filter, which will be presented later.

If the FOG can be considered to be an accurate replacement of the spacecraft dynamics model, this is a good result for removing these low frequency distortions. The downside is that the effect of alignment variations will vary from pointing to pointing depending on the signature of the thermal distortions.

In order for the STR-FOG based filter to better track low frequency errors and distortions, it is necessary to split the complete interval into smaller sub-intervals.

The plot of the FOG angular rates expressed in the spacecraft body reference system are shown in Figure 28. Also shown is a least squares fit of a model of the spacecraft angular rates to the star tracker derived angular rates. Referring to Figure 28, it can be seen from the Z-axis rate that there is a change in the trend which could indicate a shift of the principal axis not incorporated within the model of s/c angular rates.

A histogram of the estimated nutation angle is shown in Figure 27 which shows a peak value approximately at 2.2 arcsec. This is comparable to the values obtained using the current filter.

The estimation process is an iterative process[5] and in all cases run, the algorithm rapidly converged with two iterations. A further iteration was required to reduce the norm of the state vector correction to below a specified threshold of 1.0E-10. In no cases were there any poorly observable cases where the estimation process diverged.

4. Actually the low frequency errors are combined and affect the state estimate at the specified single epoch. This results from using the linearised system to refer all the observations back to this specified epoch as required to solve the batch least squares problem. As shown in Section 3.2, only the higher frequency components of the alignment variation are rejected. The low frequency terms are not rejected.
5. See Appendix C for description of the algorithm implementation

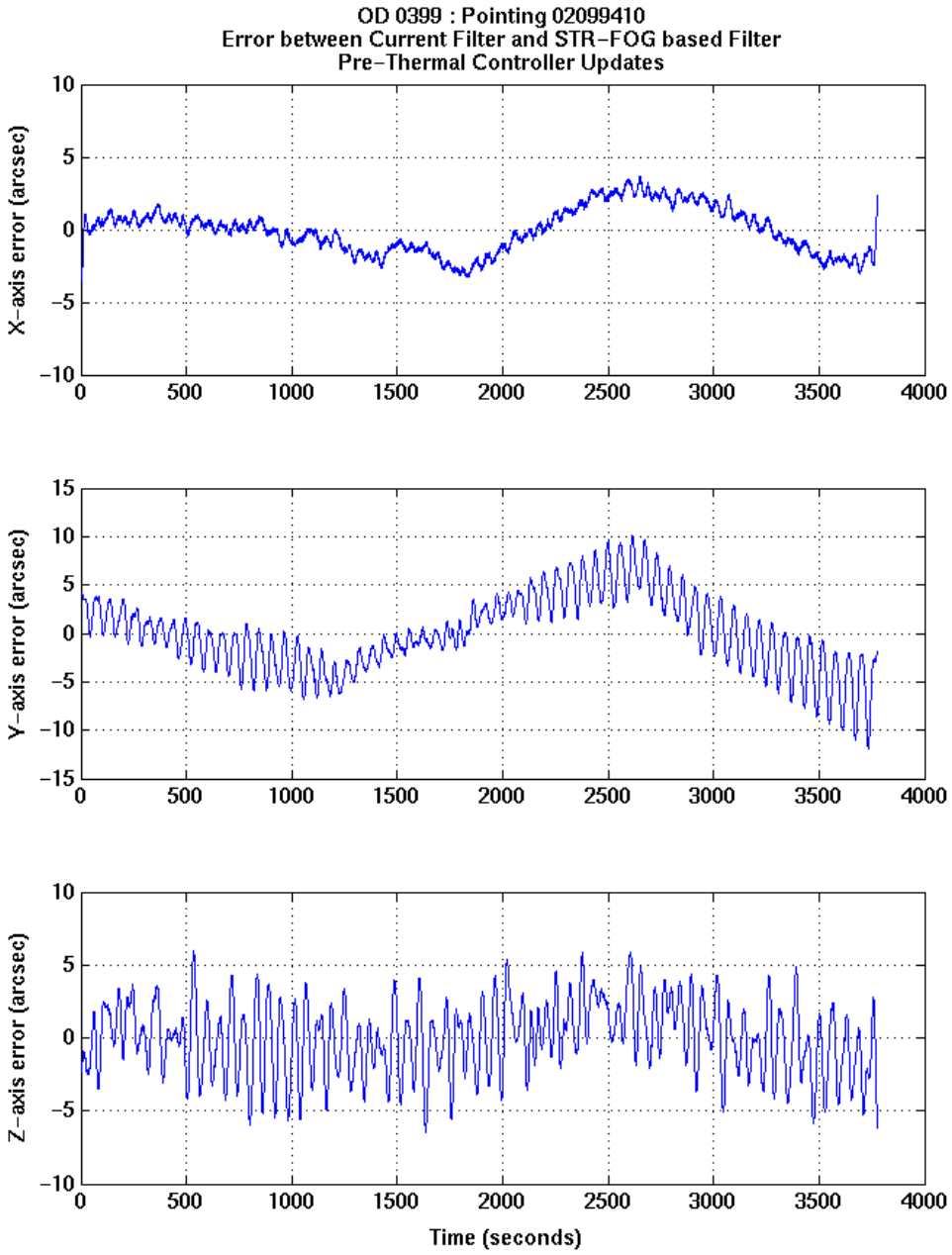

FIGURE 24: Current filter versus STR-FOG based filter comparison

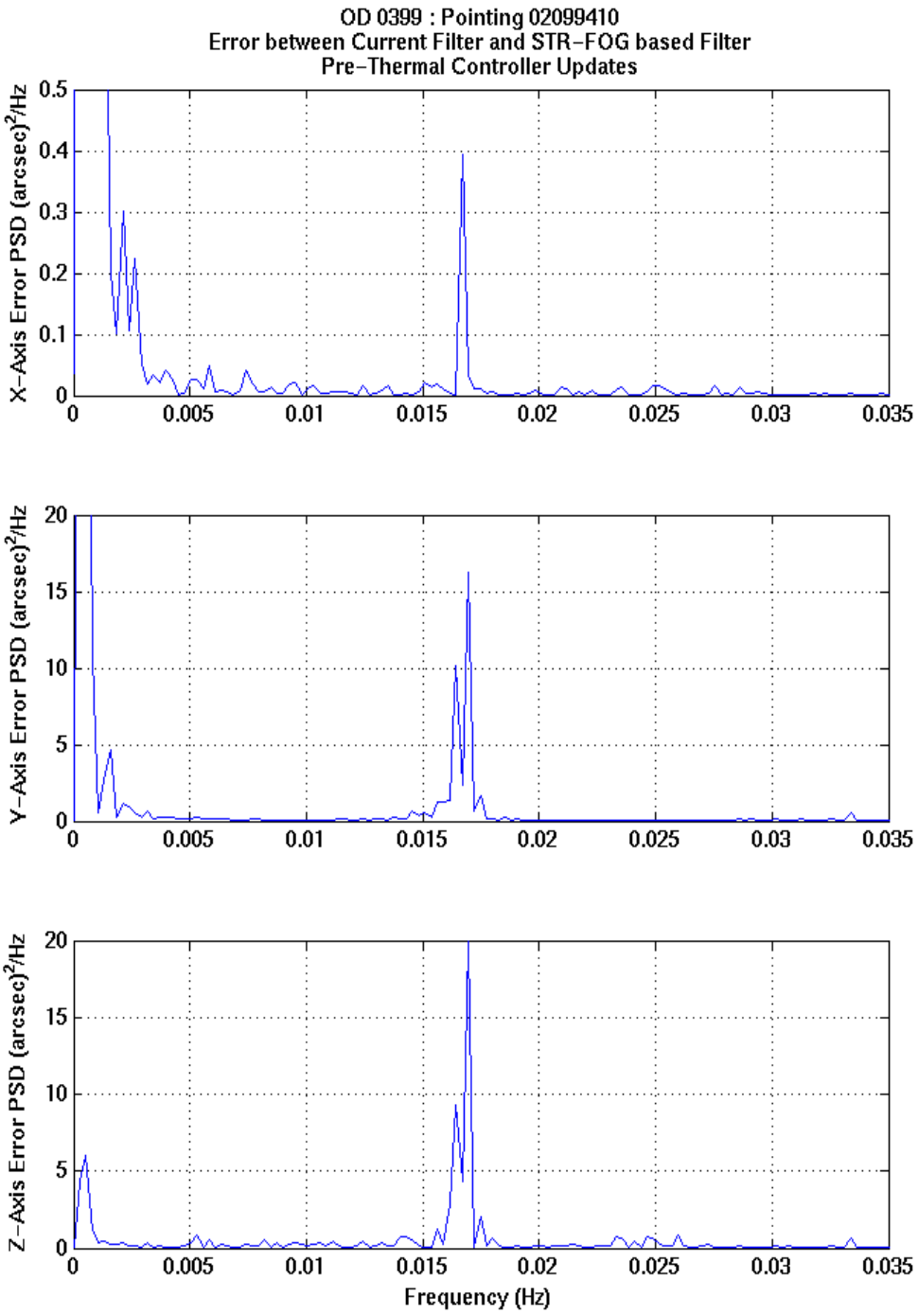

FIGURE 25: Current filter versus STR-FOG based filter comparison PSDs

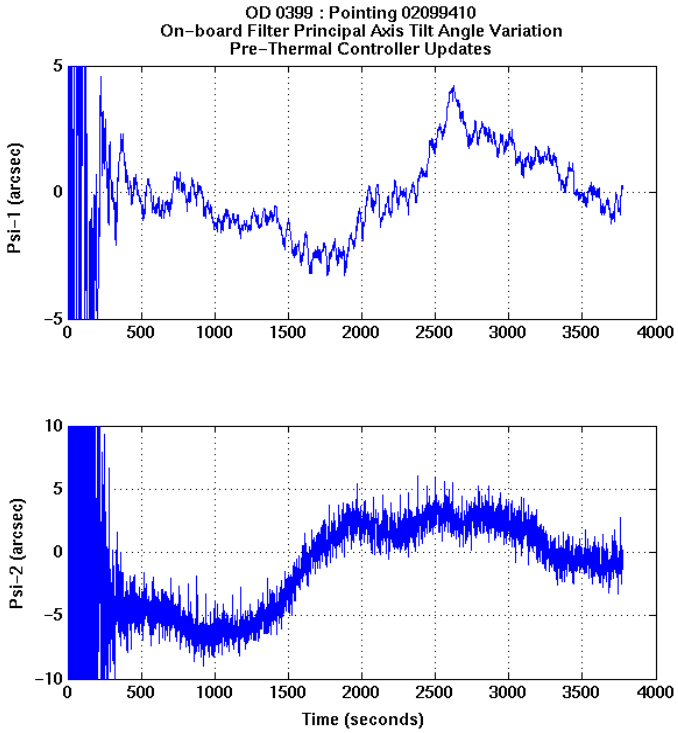

FIGURE 26: On-board principal axis tilt estimate evolution (non-zero offset removed)

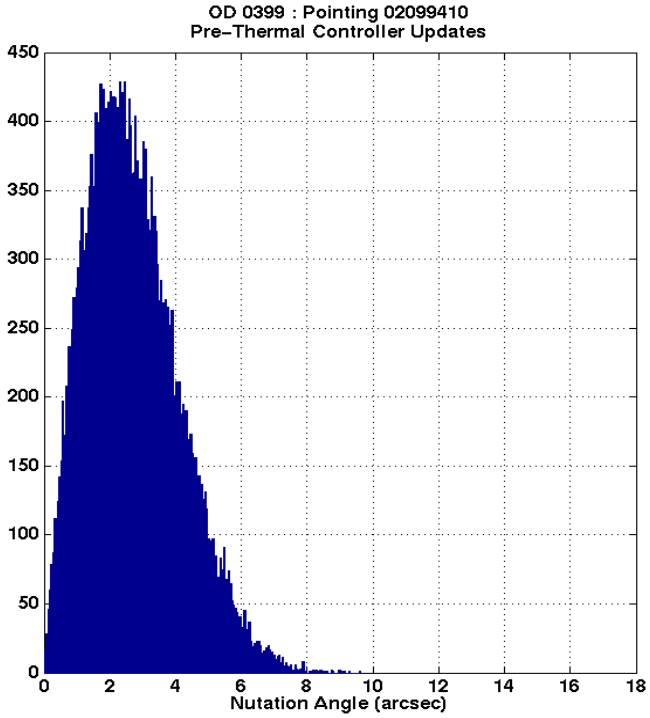

FIGURE 27: STR-FOG based filter nutation angle histogram, computed using data at 8 Hz with 200 bins

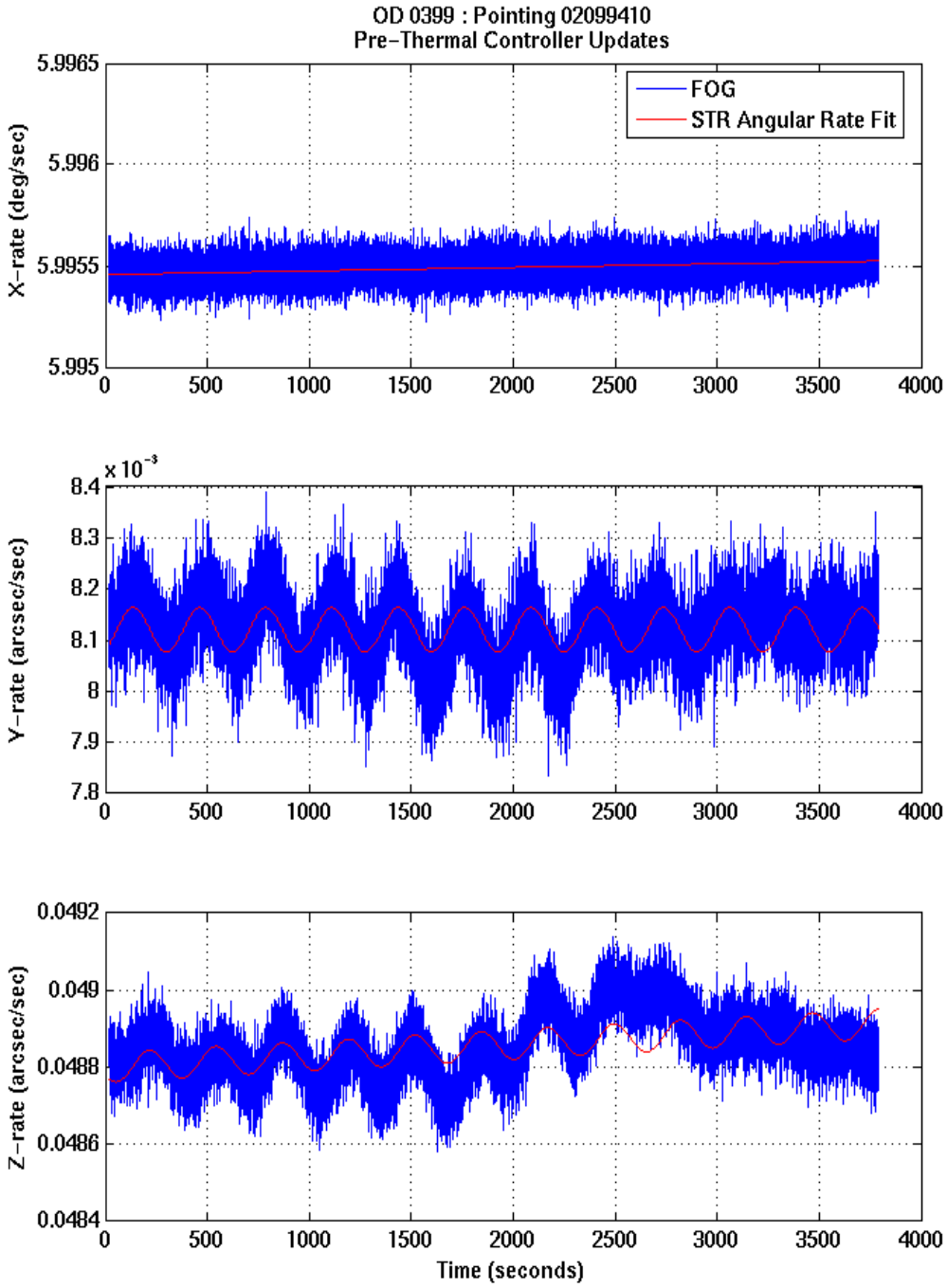

FIGURE 28: STR derived and FOG angular rates

4.1.2 Dynamic Model Based Estimation Algorithm

The errors, $\delta\underline{\theta}$, for this case are shown in below Figure 29 and the corresponding PSDs are shown in Figure 30. As with the STR-FOG comparison results in Figures 24 and 26, but to a lesser extent which is unclear why, the PSDs in Figure 30 show a modulation of the spin frequency with a low frequency term. There is also a component at the nutation frequency in $\delta\theta_y$ and $\delta\theta_z$ and two X-axis frequency components, that will be discussed in

the following paragraph. A comparison of $\delta\theta_y$ and $\delta\theta_z$, with the on-board filter estimates of the principal axis tilt angles, ψ_2 and ψ_1, shown in Figure 26, with non-zero offsets removed, shows a slightly better correlation in relation to the STR-FOG based filter. As with the STR-FOG based filter, this allows us to infer that the low frequency alignment variations of the star tracker mounting are passed by the current filter and partially rejected by the new STR-Dynamic model based filter.

As mentioned previously, referring to Figures 29 and 30, there is a periodic signal remaining in the $\delta\theta_x$ error angle, which is not present in the STR-FOG based filter results of Figures 24 and 25. In the STR-FOG intercalibration work of [14], these low frequency components in the X-axis angular rate PSD plot of Figure 9 of [14] are not discernible. This was addressed for a more recent long pointing where the spacecraft is in SCM and the results of this clearly show these frequencies in the processed STR and FOG data. These effects have now been correlated with the compressor cycle time and are due to internal disturbances created by the sorption cooler. Other effects are thermoelastic distortions that affect the STR and to a lesser extent the FOG as shown in the Z-axis rate PSD of Figure 33. The PSDs were created from data taken during a long pointing during the CPV phase in ODs 0077 to 0079 and are shown in Figure 33. Also, the X-axis integrated rate PSD shown in Figure 34. Table 6 gives a complete list of the frequencies observed in the rate PSDs of Figure 33 and where possible the source of the disturbance and which sensors are affected is identified.

Since the rigid body dynamic model does not account for internal disturbances caused by the sorption cooler, it was for this reason that the filter described in Section 2.6 was modified to include an estimation of these extra state variables. The result of the updates to the filter can be seen in Figure 32, which shows that the error, $\delta\theta_x$, has been significantly reduced with these updates.

Another way to look at this is that if we numerically differentiate $-\delta\theta_x$, the resulting rate, $-\delta\omega_x$, correlates quite well with the low pressure side of the sorption cooler (P8). An estimate of how much the X-axis moment of inertia varies as a result of mass migration has been computed from this rate variation using (39) and is shown in Figure 31.

$$\delta J_x = -J_x\left(\frac{\delta\omega_x}{\omega_x}\right) \tag{39}$$

The mean nutation angle derived from the principal axis rates and the assumed moment of inertia tensor is 1.29 arcsec.

The algorithm rapidly converged with four iterations. A further iteration was required to reduce the norm of the state vector correction to below a specified threshold of 1.0E-10. In no cases were there any poorly observable cases where the estimation process diverged.

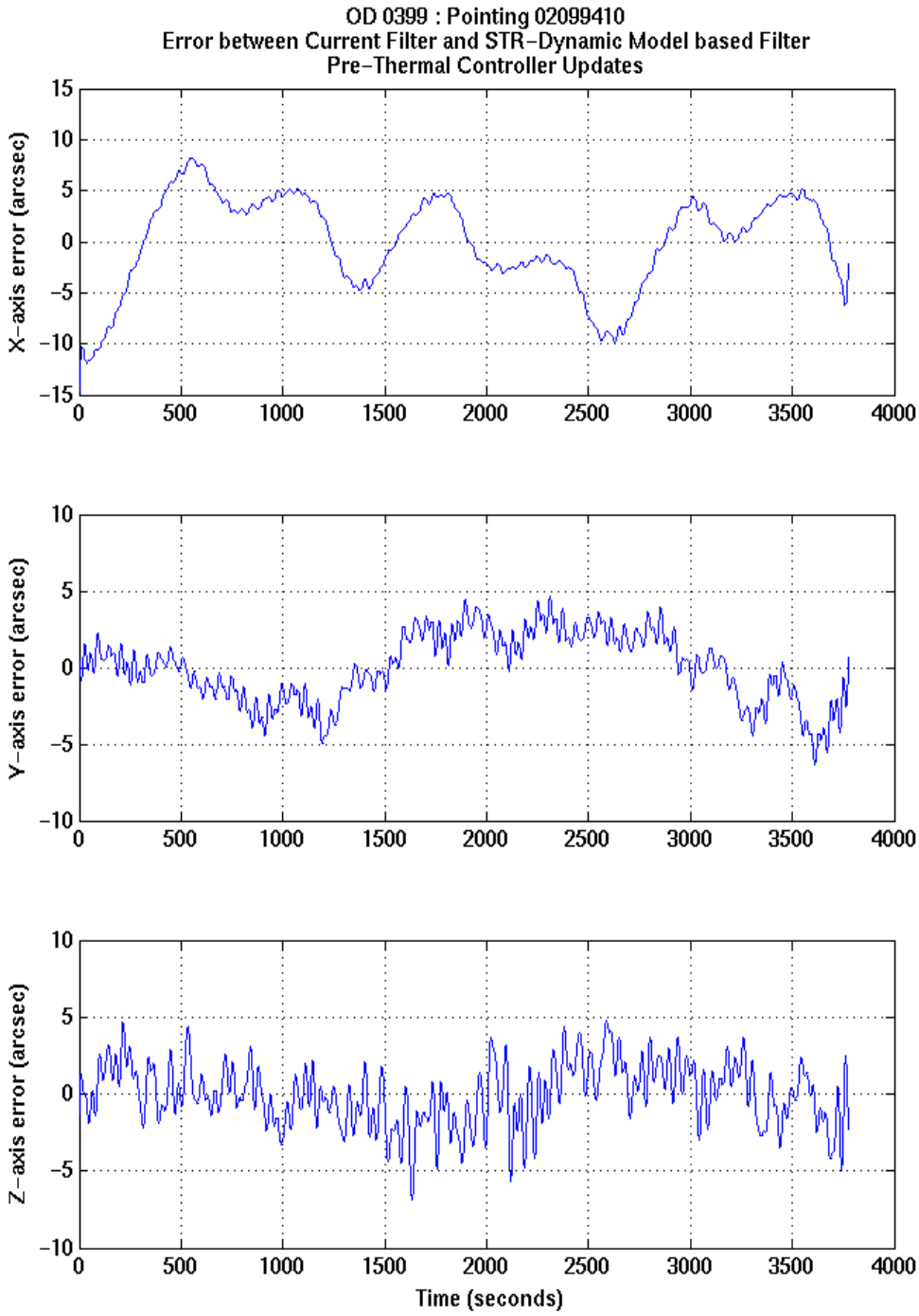

FIGURE 29: Current filter versus STR-Dynamic model based filter comparison: sorption cooler internal disturbances not estimated

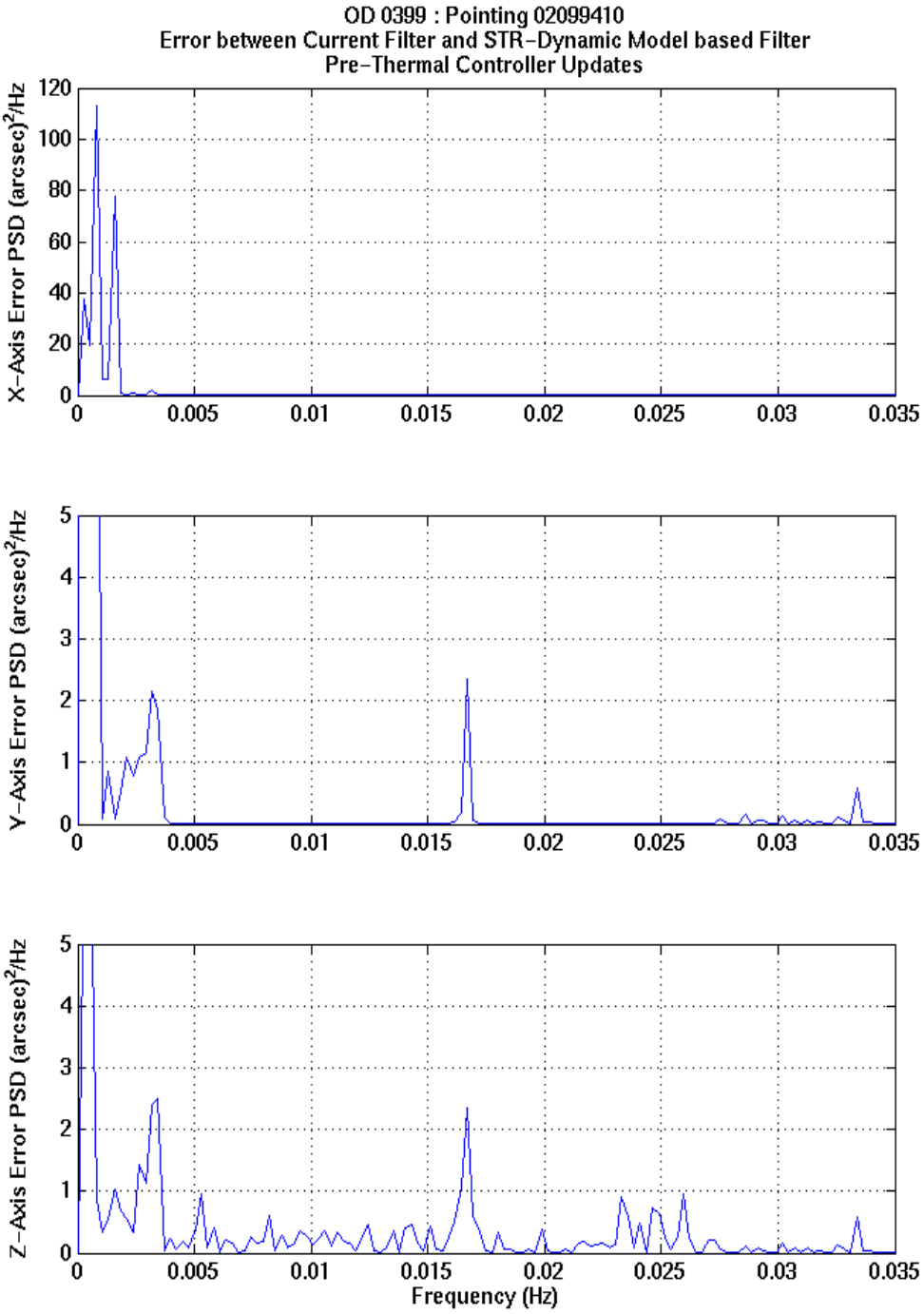

FIGURE 30: Current filter versus STR-Dynamic model based filter comparison PSDs: sorption cooler internal disturbances not estimated

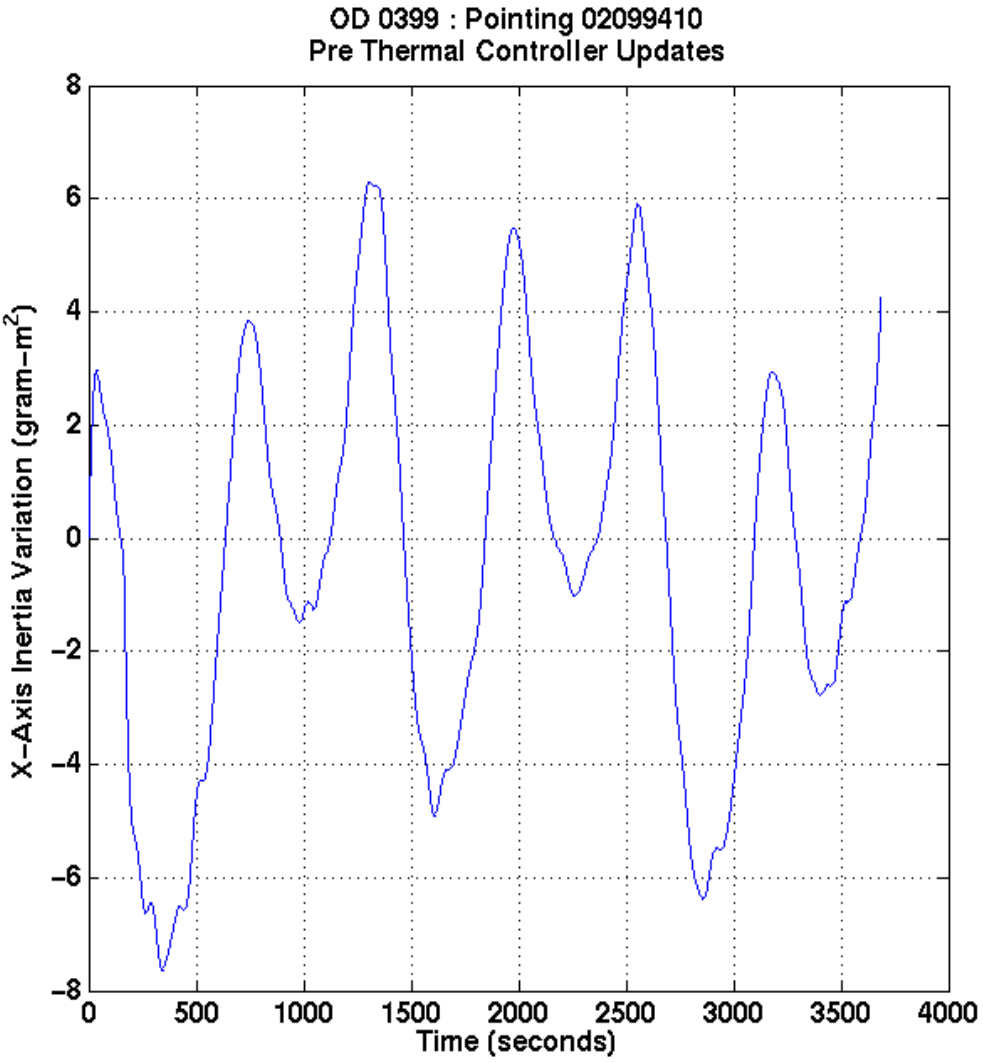

FIGURE 31: Estimate of variation in the principal X-axis moment of inertia

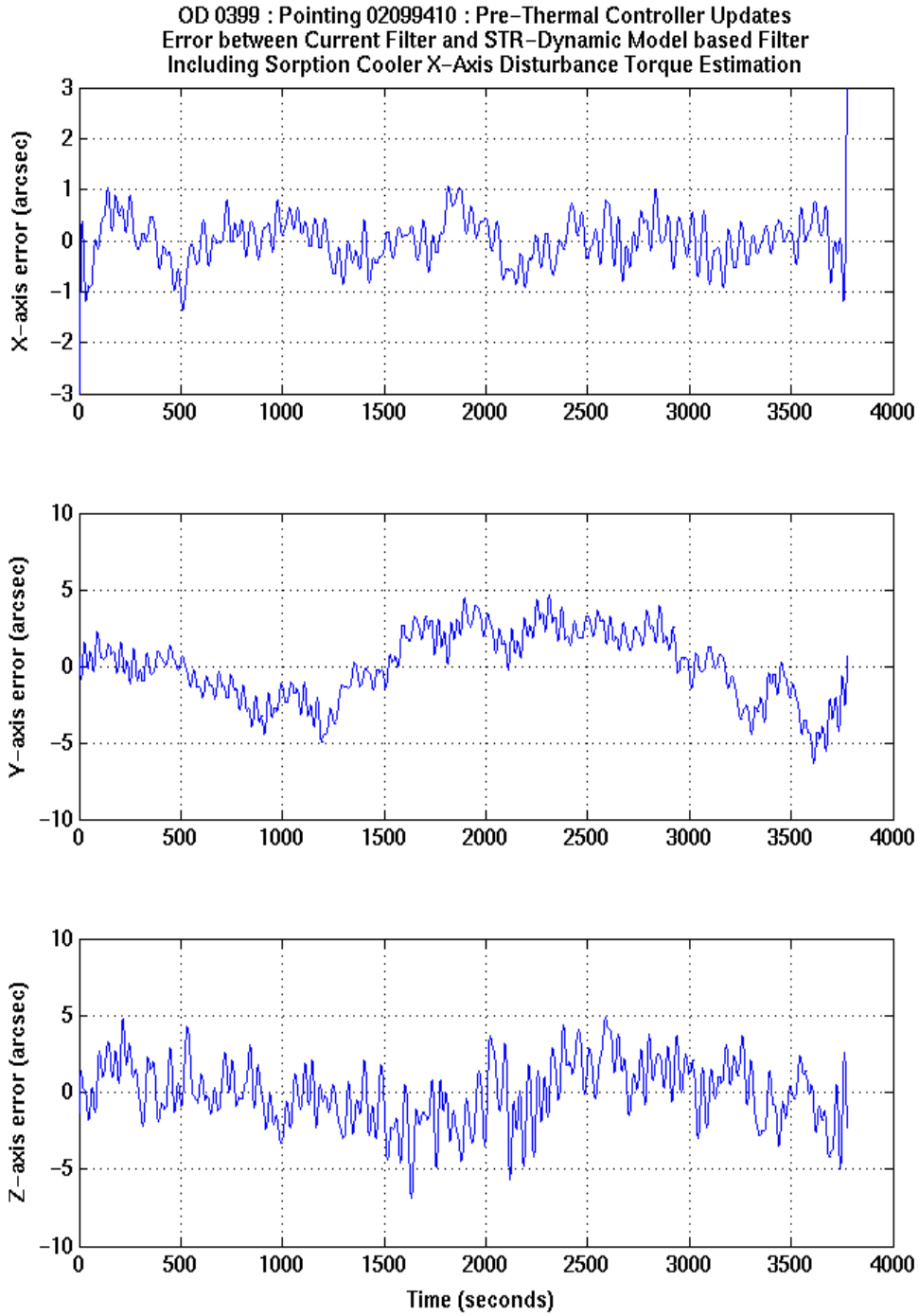

FIGURE 32: Current filter versus STR-Dynamic model based filter comparison: sorption cooler internal disturbances estimated.

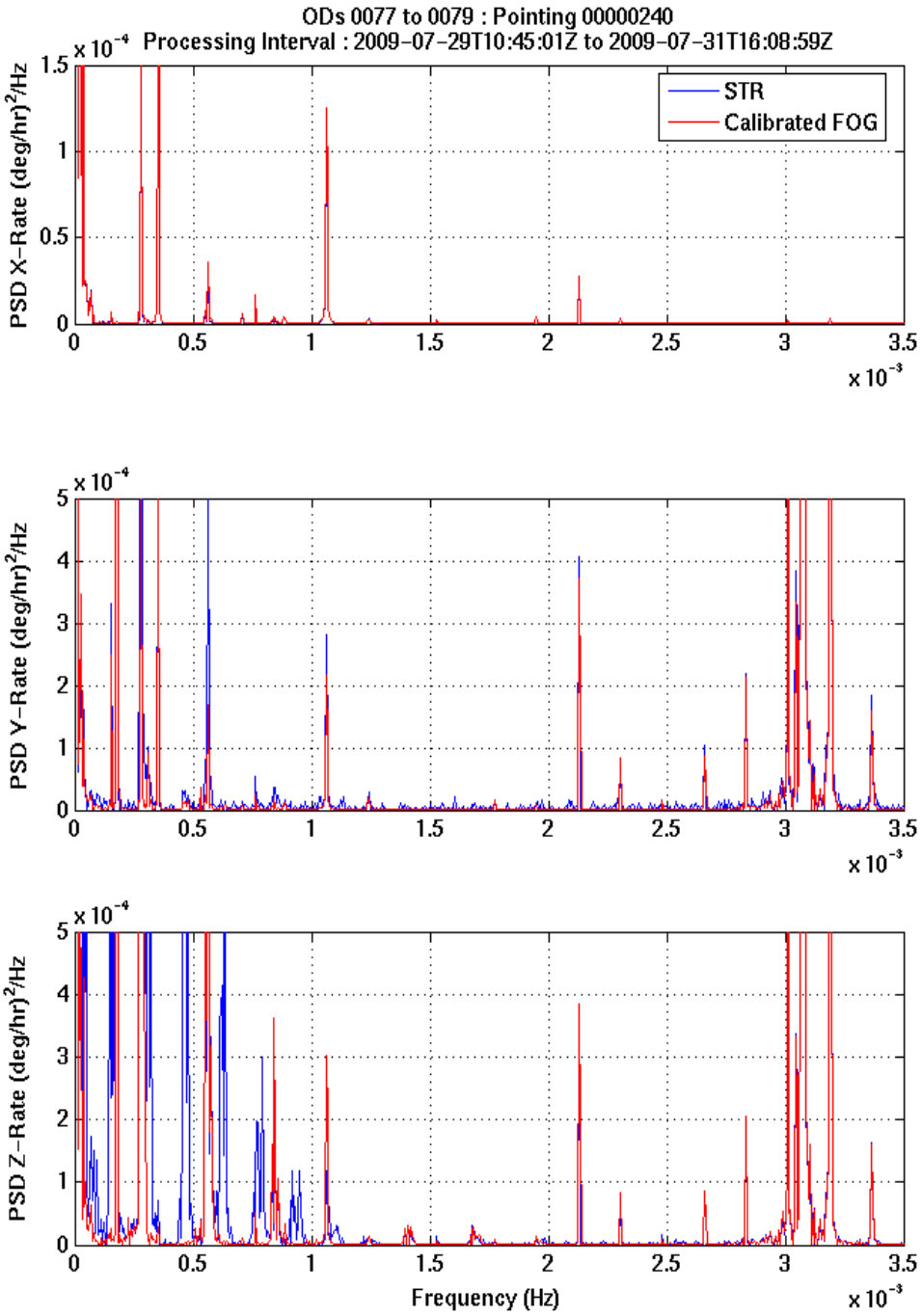

FIGURE 33: STR/FOG Angular Rate PSDs

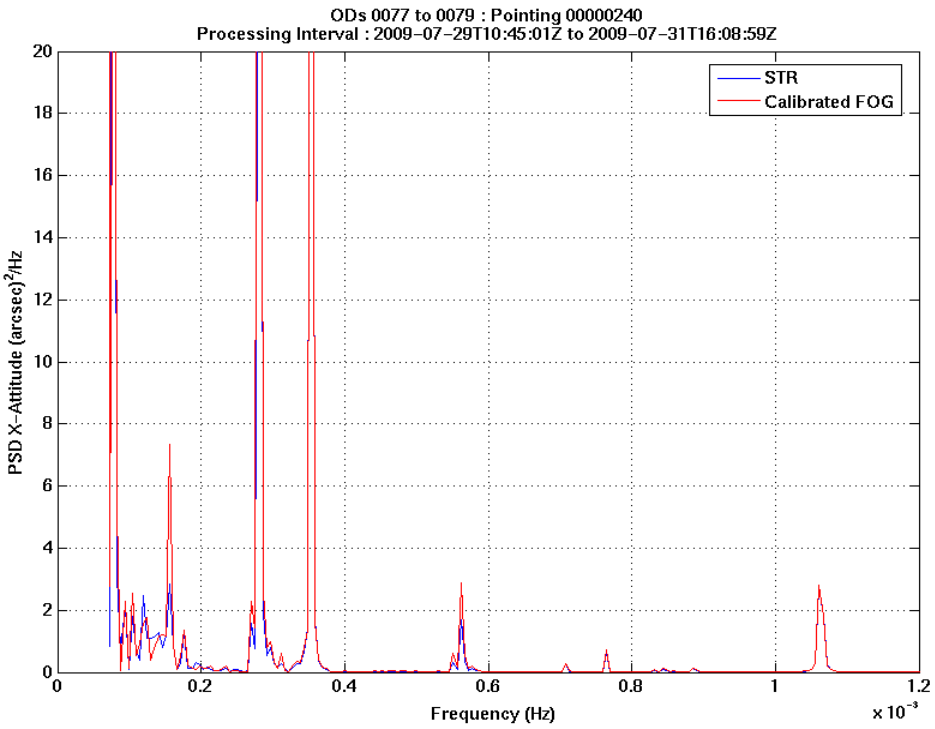

FIGURE 34: STR/FOG X-Axis Integrated Angular Rate PSD

Source	Frequency (mHz)	Sensors affected
DPU-2 (fundamental)	0.15614	STR only
SCS (fundamental)	0.1773	STR+FOG
REBA (fundamental)	0.2809	STR+FOG
DPU-2 (2nd harmonic)	0.31136	STR only
SCS (2nd harmonic)	0.3546	STR+FOG
DPU-2 (3rd harmonic)	0.4684	STR only
REBA (2nd harmonic)	0.56182	STR+FOG
DPU-2 (4th harmonic)	0.62456	STR only
DPU-2 (5th harmonic)	0.7807	STR only
REBA (3rd harmonic)	0.8433	STR+FOG
DPU-2 (6th harmonic)	0.93684	STR only
Compressor cycle (fundamental)	1.0638	STR+FOG
Compressor cycle (2nd harmonic)	2.1276	STR+FOG
Unidentified frequency	3.012	STR+FOG
Nutation frequency	3.07	STR+FOG
Compressor cycle (3rd harmonic)	3.1914	STR+FOG

TABLE 6: Modes identified from the rate PSDs in Figure 33

4.2 Post Thermal Control Updates - Science Mode Pointings

4.2.1 Fibre Optic Gyro Based Estimation Algorithm

The errors, $\delta\underline{\theta}$, are shown in below Figure 35 and the corresponding PSDs are shown in Figure 36. The PSDs show a modulation of the spin frequency with a low frequency term. The on-board filter estimates of the principal axis tilt angles, ψ_2 and ψ_1, with the non-zero offset subtracted, are shown in Figure 37.

It can be seen from the results in Figure 37 that the changes to the thermal controller have resulted in a significant improvement in the stability of the principal axis tilt estimates. This has also been confirmed in the principal axis tilt estimates that are provided in the routine AHF products. As a result, this has also had a positive impact in the angle error comparisons between current and new filters, as shown in Figure 35 for the STR-FOG based filter. There is still a spin frequency component observable in the errors, but the performances of the 2 filters are quite similar. The results shown in Figure 35 are also quite similar to the results of the HPTDG versus current filter output comparisons shown in Figure 5, where it was concluded in Section 3.2 that the new filters were efficient in rejecting STR spatial bias errors.

The plot of the FOG angular rates expressed in the spacecraft body reference system are shown in Figure 38. Also shown is a least squares fit of a model of the spacecraft angular rates to the star tracker derived angular rates.

A histogram of the estimated nutation angle is shown in Figure 39 which shows a peak value approximately at 1.8 arcsec. This is comparable to the values obtained using the current filter and slightly less than the value obtained prior to the thermal controller updates.

The sensitivity of the STR-Dynamic Model based filter to variations in the STR alignment was already analysed previously in Section 3.2. The same analysis performed here for STR-FOG based filter, shows similar results for the comparisons made with the current filter output. As with analysis performed in Section 3.2, 3 cases have been considered:-

1. A sinusoidal variation shown in Figure 40
2. An exponential rise/fall variation (one time constant) shown in Figure 42
3. An exponential rise/fall variation (two time constants) shown in Figure 44

For the first case, the results for the Y-axis angle error shown in Figures 16 and 41 are quite similar. Likewise for the second case, the results shown in Figures 18 and 43 and finally for the third case, the results shown in Figures 20 and 45. This implies that similar conclusions to those reached in Section 3.2 can be reached.

The algorithm rapidly converged with two iterations. A further iteration was required to reduce the norm of the state vector correction to below a specified threshold of 1.0E-10. In no cases were there any poorly observable cases where the estimation process diverged.

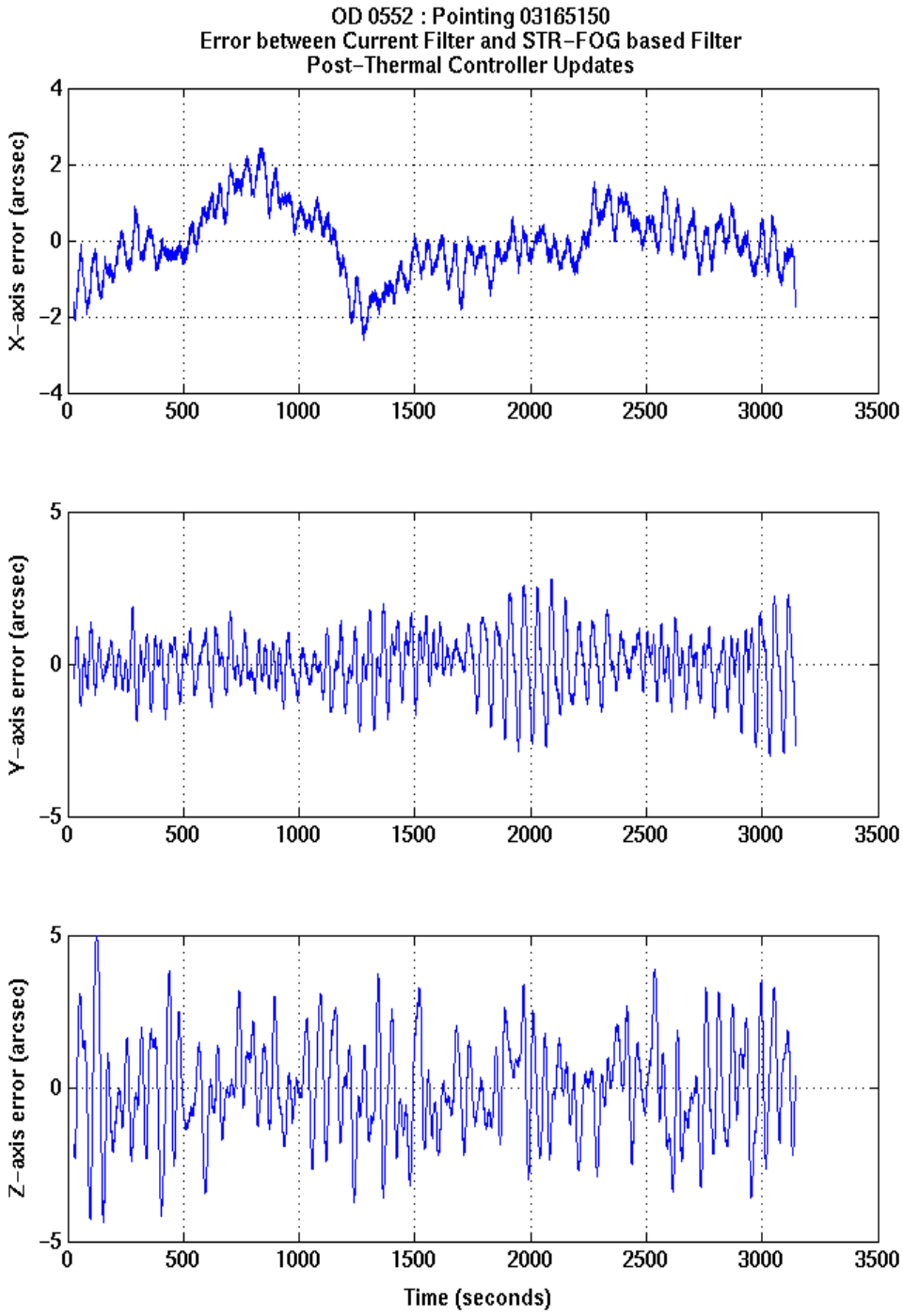

FIGURE 35: Current filter versus STR-FOG based filter comparison

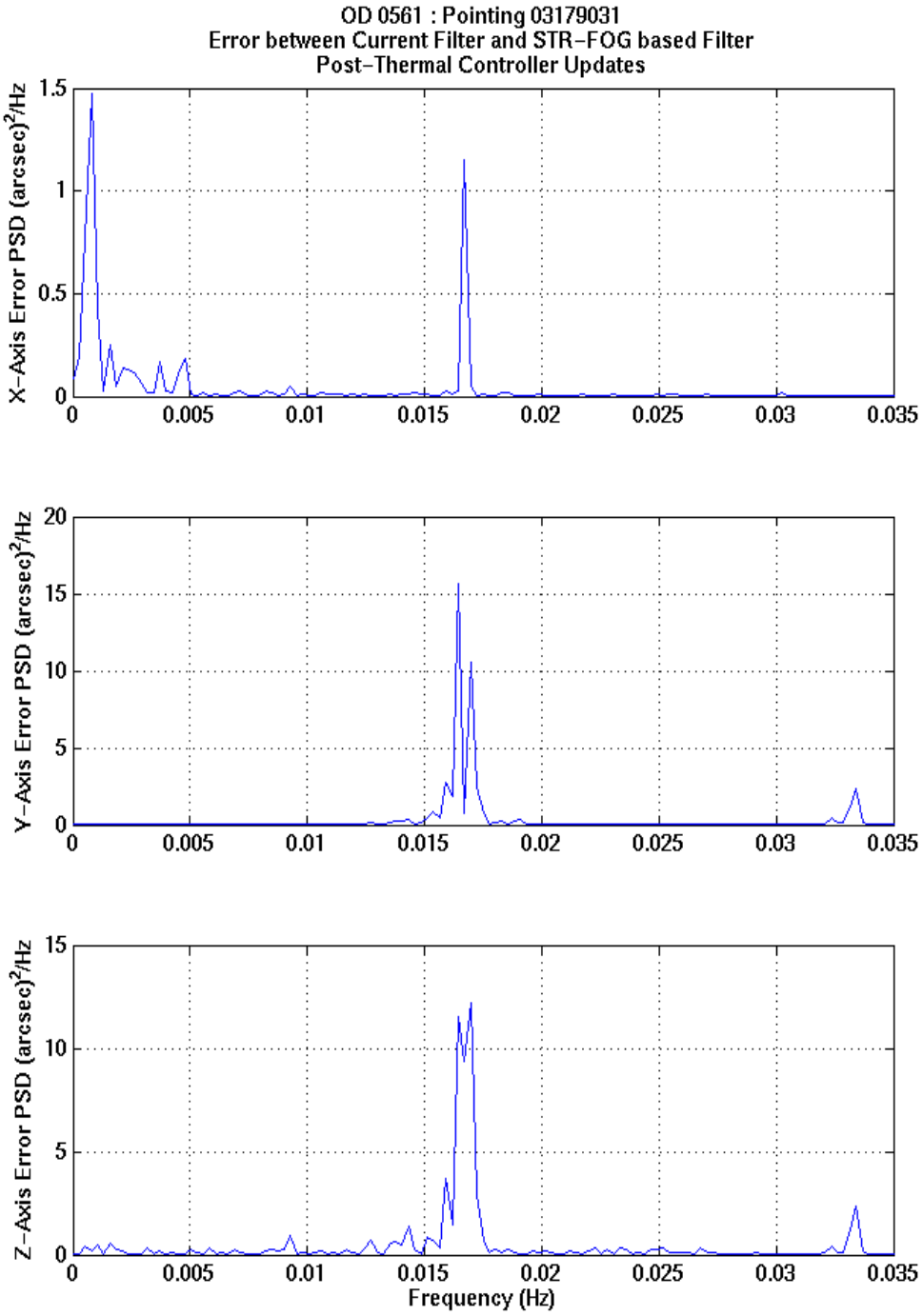

FIGURE 36: Current filter versus STR-FOG based filter comparison PSDs

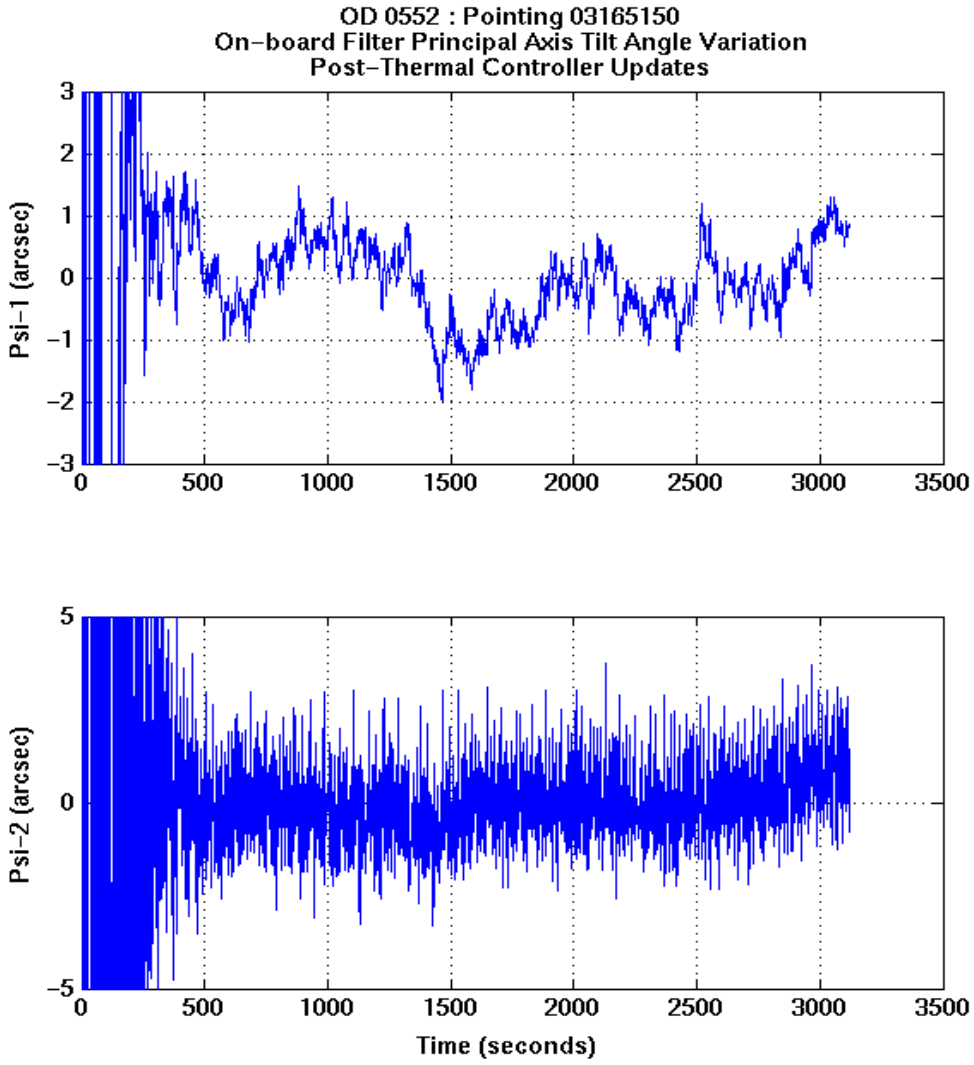

FIGURE 37: On-board principal axis tilt estimate evolution (non-zero offset removed)

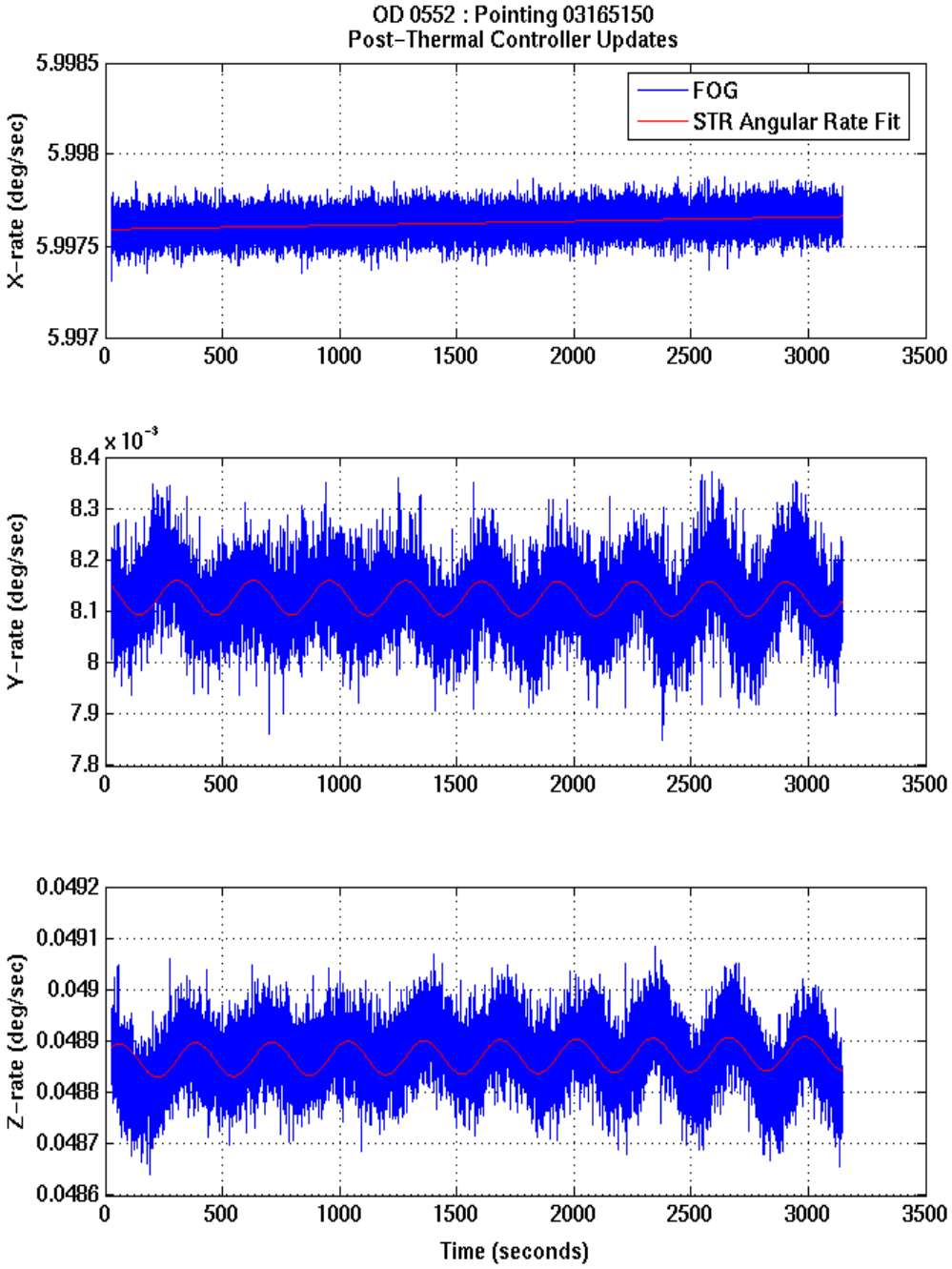

FIGURE 38: STR derived and FOG angular rates

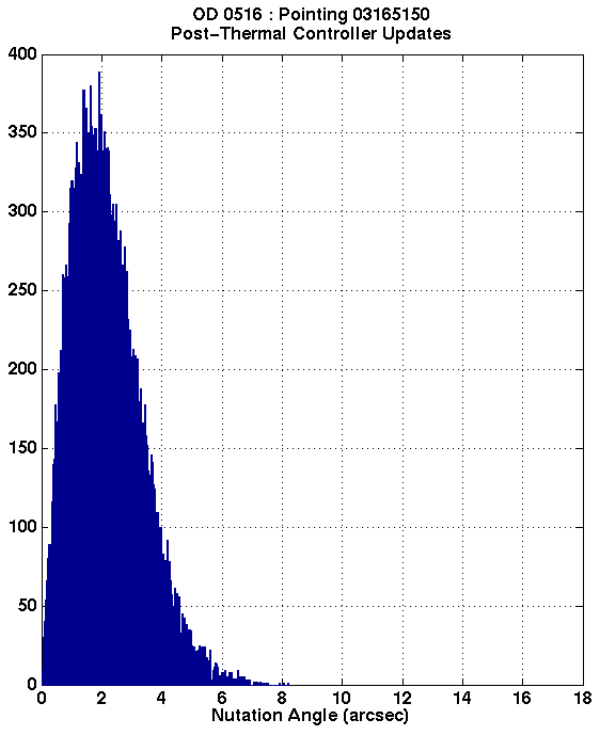

FIGURE 39: STR-FOG based filter nutation angle histogram, computed using data at 8 Hz with 200 bins

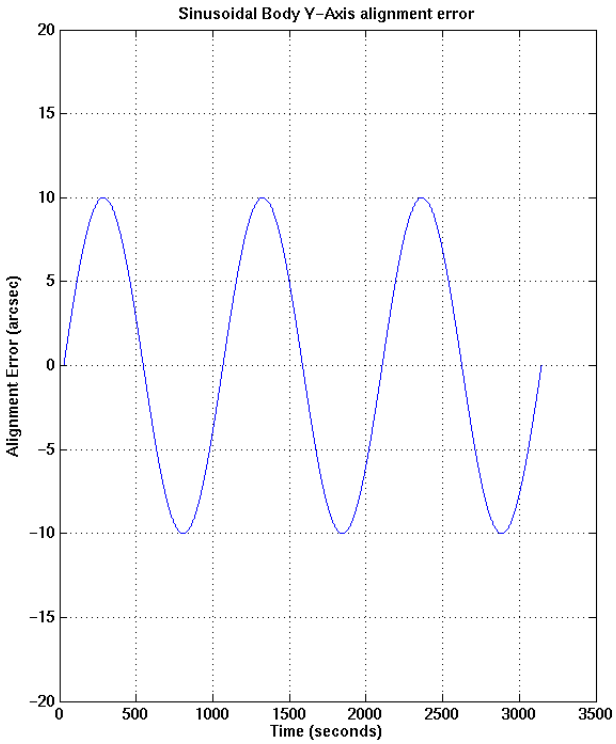

FIGURE 40: Low frequency sinusoidal alignment error injected on the Y-axis

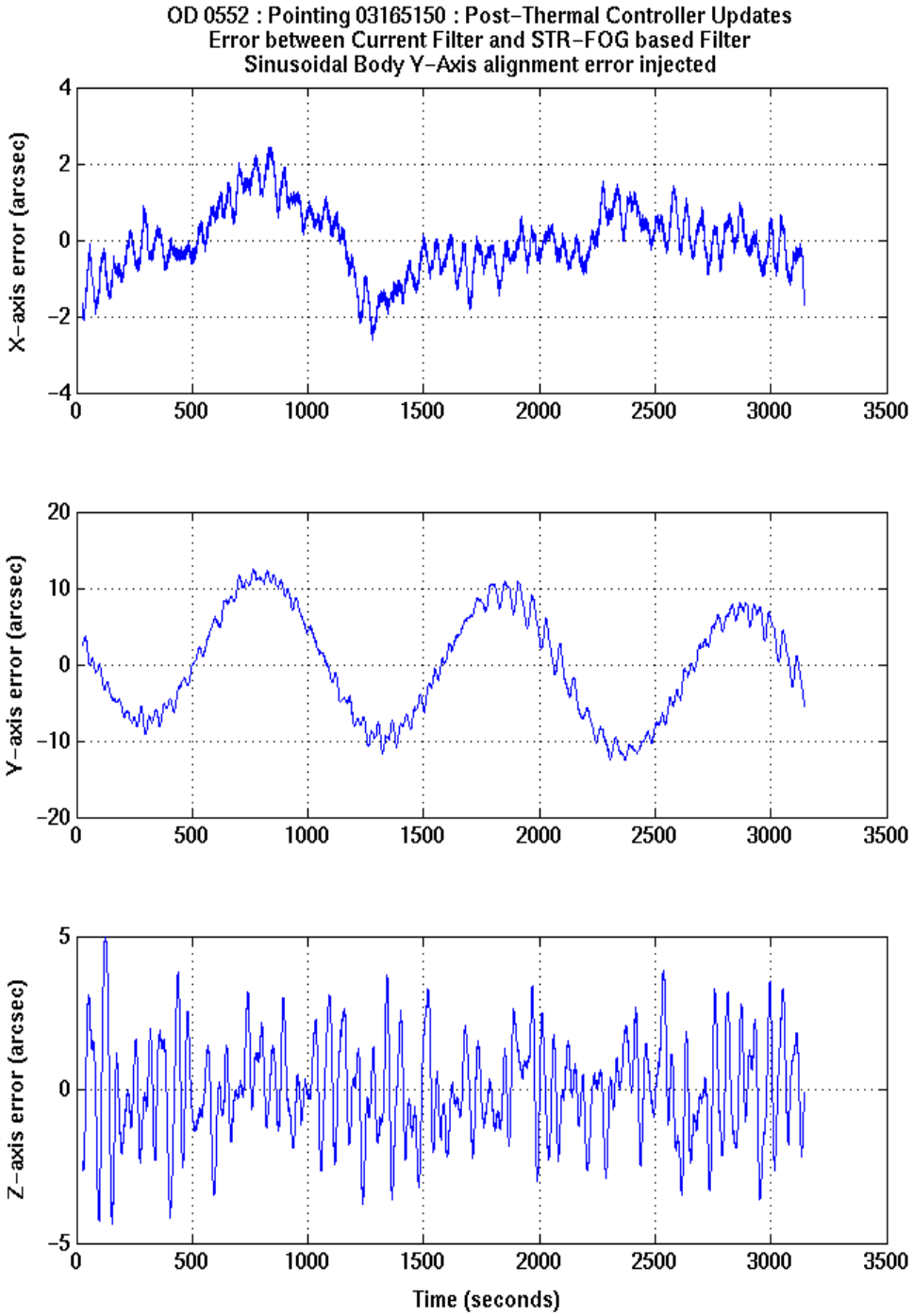

FIGURE 41: Current filter versus STR-FOG based filter comparison with a star tracker low frequency sinusoidal alignment error injected on the Y-axis

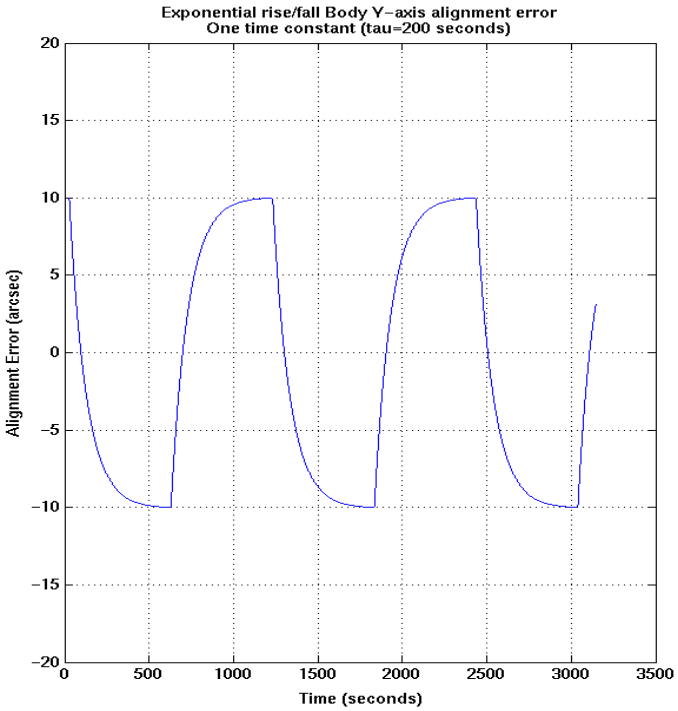

FIGURE 42: Low frequency exponential rise/fall alignment error injected on the Y-axis. One time constant (τ = 200 s)

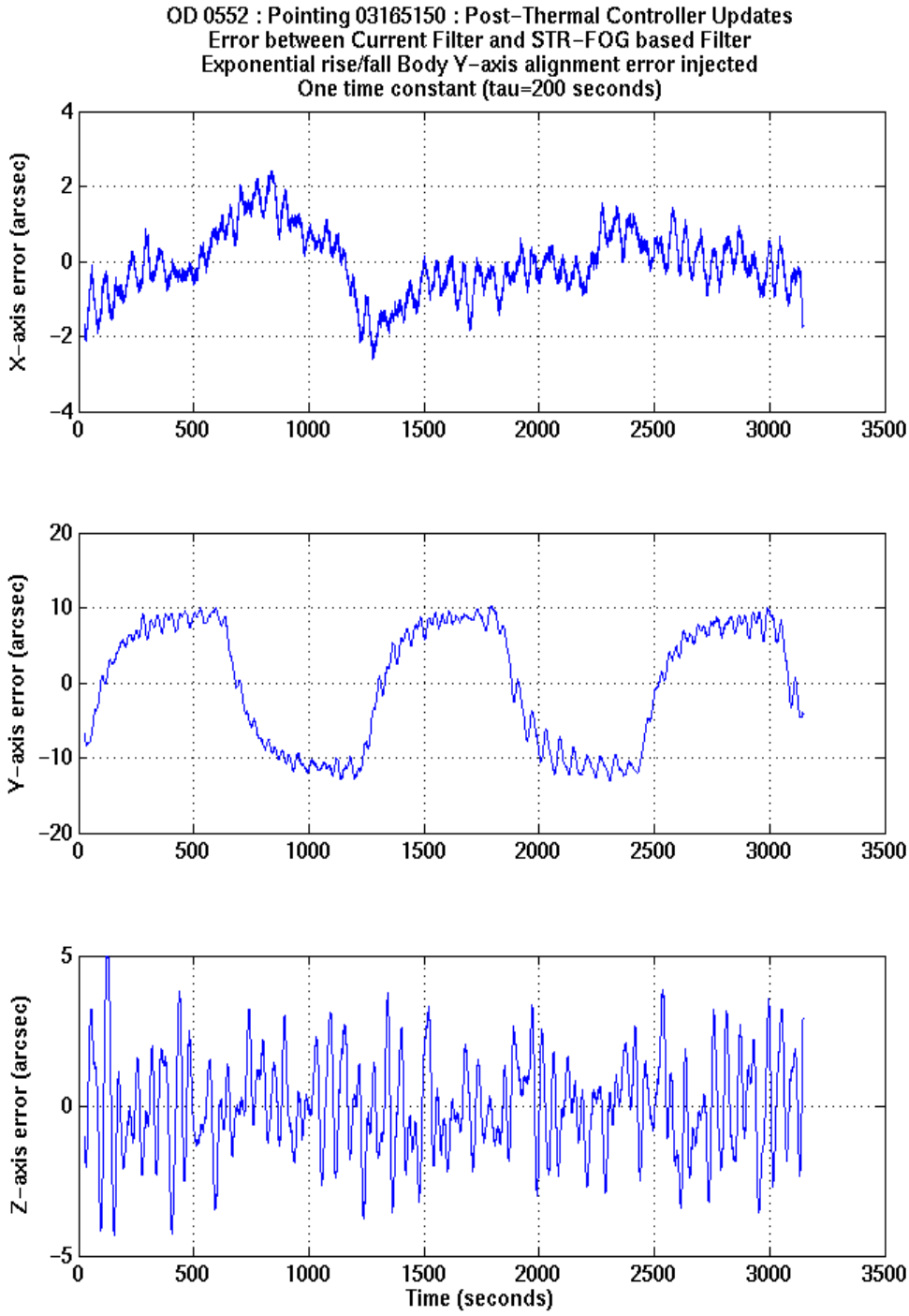

FIGURE 43: Current filter versus STR-FOG based filter comparison with a star tracker low frequency exponential rise/fall alignment error injected on the Y-axis. One time constant (τ = 200 s)

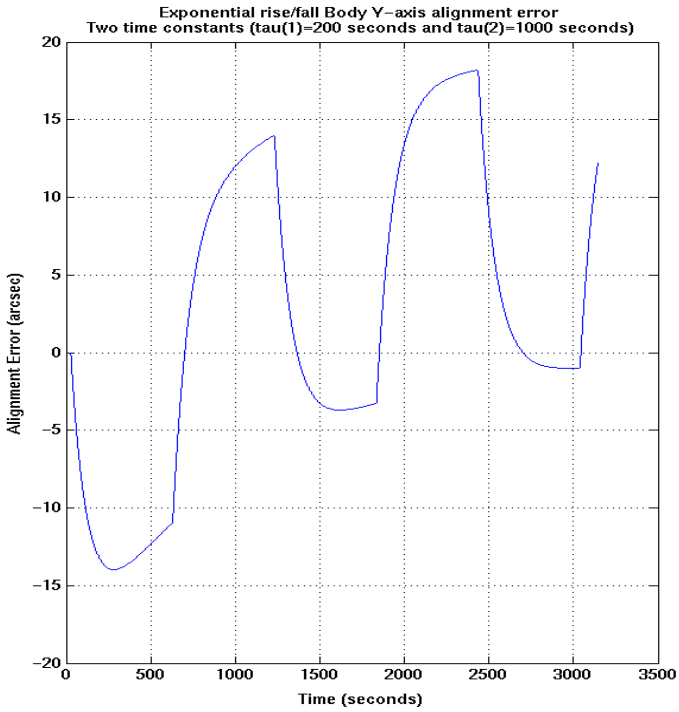

FIGURE 44: Low frequency exponential rise/fall alignment error injected on the Y-axis. Two time constants (τ_1 = 200 s and τ_2 = 1000 s)

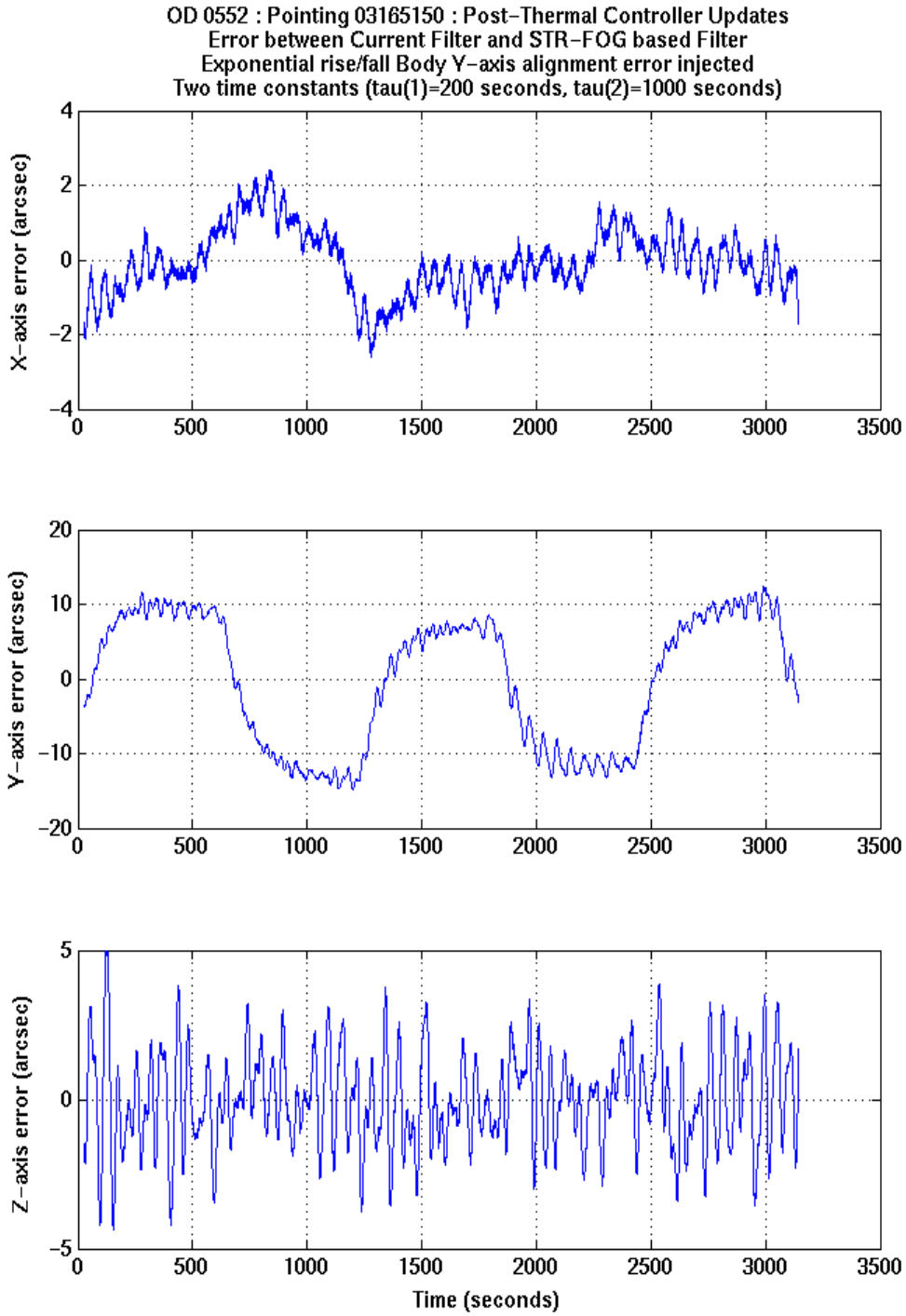

FIGURE 45: Current filter versus STR-FOG based filter comparison with a star tracker low frequency exponential rise/fall alignment error injected on the Y-axis. Two time constants (τ_1 = 200 s and τ_2 = 1000 s)

4.2.2 Dynamic Model Based Estimation Algorithm

The errors, $\delta\underline{\theta}$, for this case are shown in below Figure 46 and the corresponding PSDs are shown in Figure 47. The PSDs in Figure 47 show a component at the spin frequency and at twice the spin frequency that is modulated with a low frequency term. As with the pre-thermal controller updates case, referring to Figure 46, there is a

trend in the $\delta\theta_x$ error angle, which is not observed in the STR-FOG based filter results of Figure 35.

Again, if we numerically differentiate $-\delta\theta_x$, the resulting rate, $-\delta\omega_x$, correlates quite well with the low pressure side of the sorption cooler (P8). Using (39), an estimate of how much this rate variation translates into a variation of the X-axis moment of inertia, is shown in Figure 48. These estimates are comparable to the estimates obtained in the pre-thermal controller updates case.

In ODs 560 and 561, there were some tests to check the STR alignment stability resulting from a switchover to the redundant star tracker and back. During the switchover periods there were long duration pointings with the spacecraft in SCM. A frequency analysis of the FOG and STR derived angular rates was performed to see if the low frequencies present in the X-axis rotational dynamics are discernible in the angular rate PSD. Since the errors are present in the X-axis attitude data, it is necessary to look at the integrated angular rate PSD when deciding on what the dominant frequencies in the error signal are.

These pointings are long enough to provide sufficient resolution at low frequencies. The errors, $\delta\underline{\theta}$, for part of this pointing are shown in Figure 49. The PSD of the angular rates, computed using the complete data set, are shown in Figure 51. The PSD for the integrated X-axis angular rate is shown in Figure 52. It is clear from Figures 51 and 52, that there are peaks at 1.09 mHz, 2.18 mHz and 3.27 mHz in the X-axis rate PSD, for both STR and FOG data. The dominant frequency being due to the sorption cooler compressor cycle, which is commanded regularly by the flight control team to update a lookup table (LUT). On the transverse axes, one also sees a peak at 0.15 mHz, which is the whole cooler cycle period. The reader is referred to section 6.2.4.3 of [17] for an explanation. It is also noted that some frequencies observed in Figure 33, Figure 34 and Table 6, in particular the DPU-2 ones, are significantly reduced.

It can be concluded that the rigid body dynamic model does not account for these perturbations. Due to the periodic nature of the error, $\delta\theta_x$, the dynamic model has been modelled as a rigid body with an X-axis internal disturbance torque, modelled as a multiple mode pendulum. The estimator in Section 2.6 is then used to estimate the amplitude and amplitude rate of change to account for these effects. Optionally, the filter has been formulated to estimate the compressor cycle frequency as well, but this could also be simply fixed at the reciprocal of the commanded cycle time. The errors, $\delta\underline{\theta}$, for part of this pointing, when the sorption cooler internal torques are estimated, are shown in Figure 50.

The mean nutation angle derived from the principal axis rates and the assumed moment of inertia tensor is 1.29 arcsec. In Figure 51, one can see the nutation mode at about 3.05 mHz, in the transverse axes angular rate PSD plots.

The algorithm rapidly converged with four iterations. A further iteration was required to reduce the norm of the state correction to below a specified threshold of 1.0E-10. In no cases were there any poorly observable cases where the estimation process diverged.

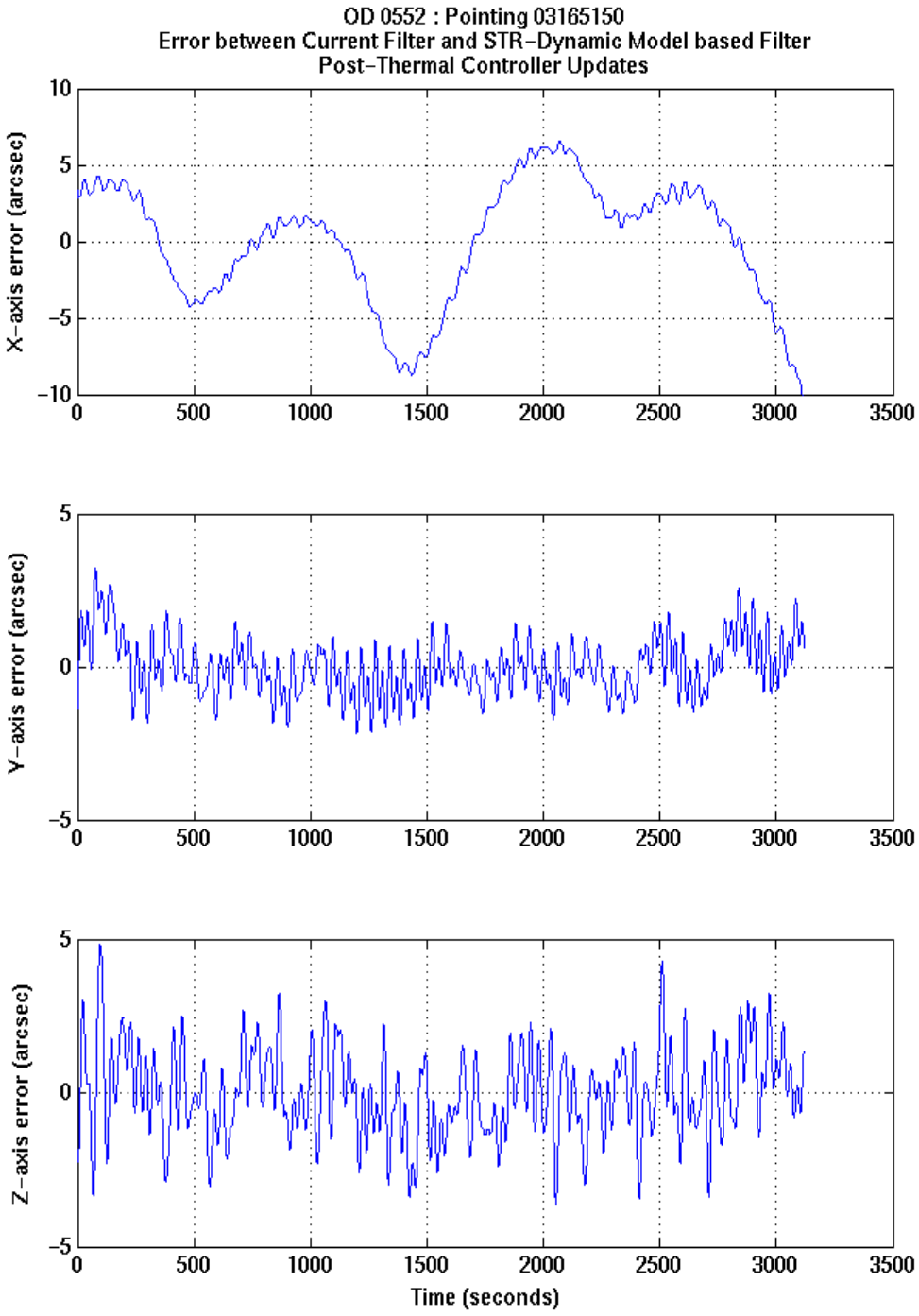

FIGURE 46: Current filter versus STR-Dynamic model based filter comparison: sorption cooler internal disturbances not estimated

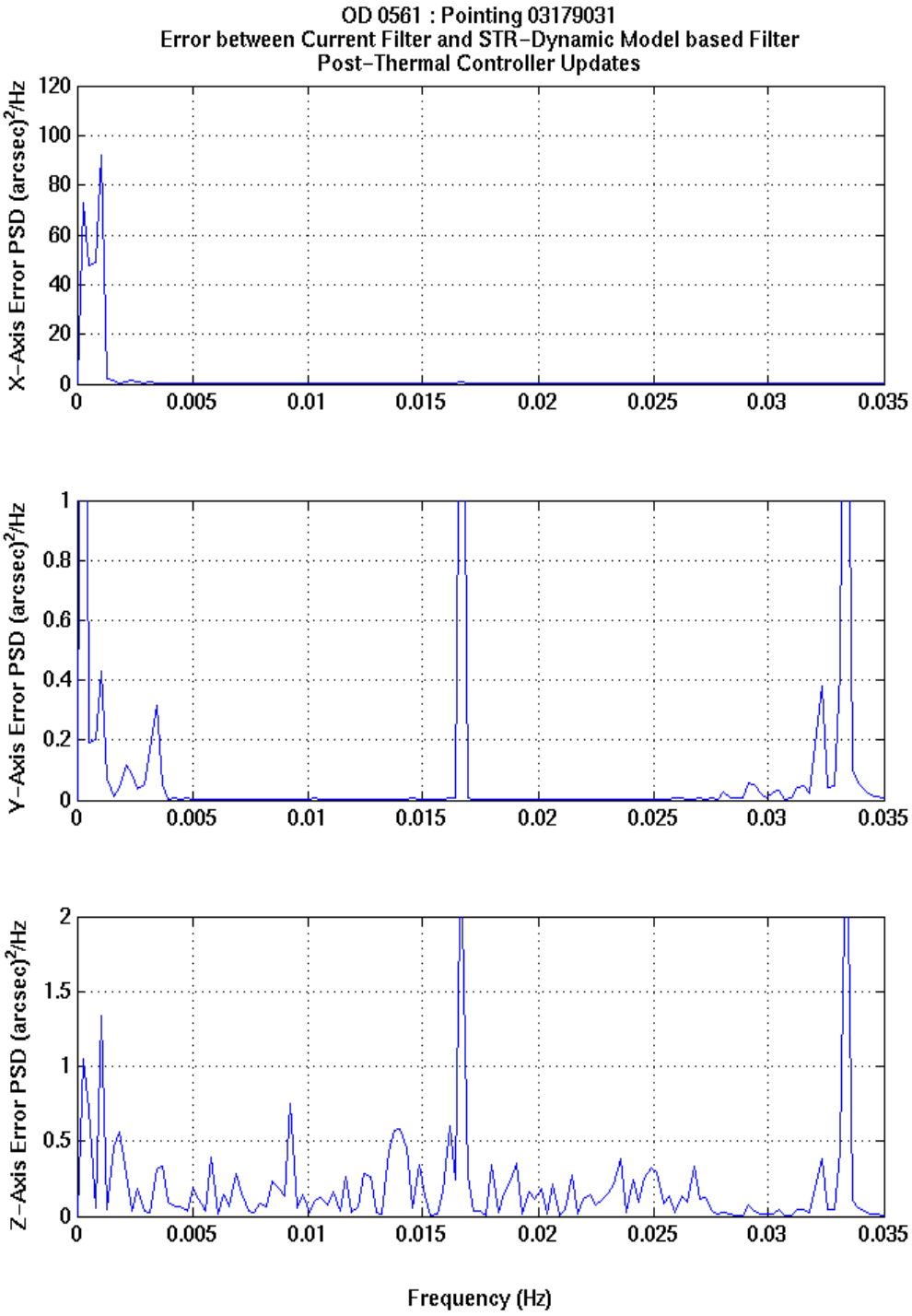

FIGURE 47: Current filter versus STR-Dynamic model based filter comparison PSDs: sorption cooler internal disturbances not estimated

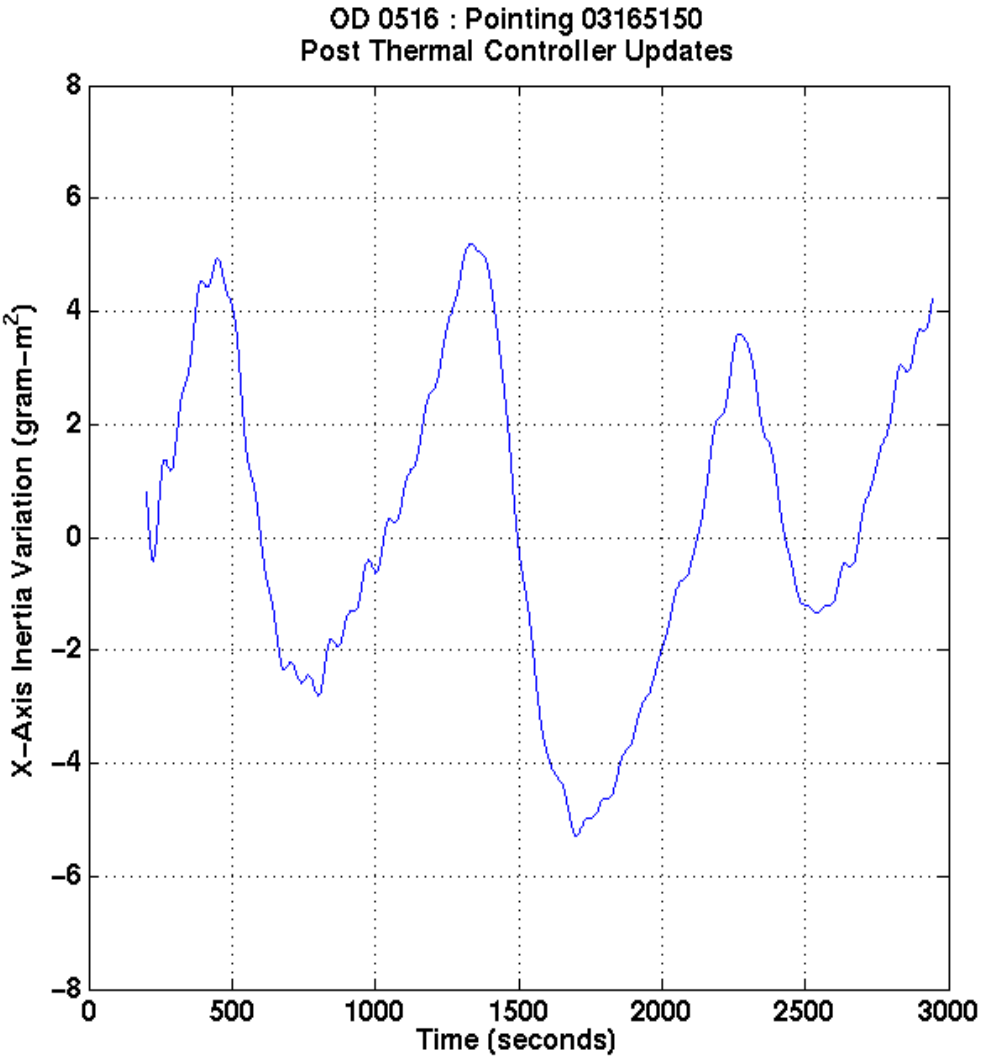

FIGURE 48: Estimate of variation in the principal X-axis moment of inertia

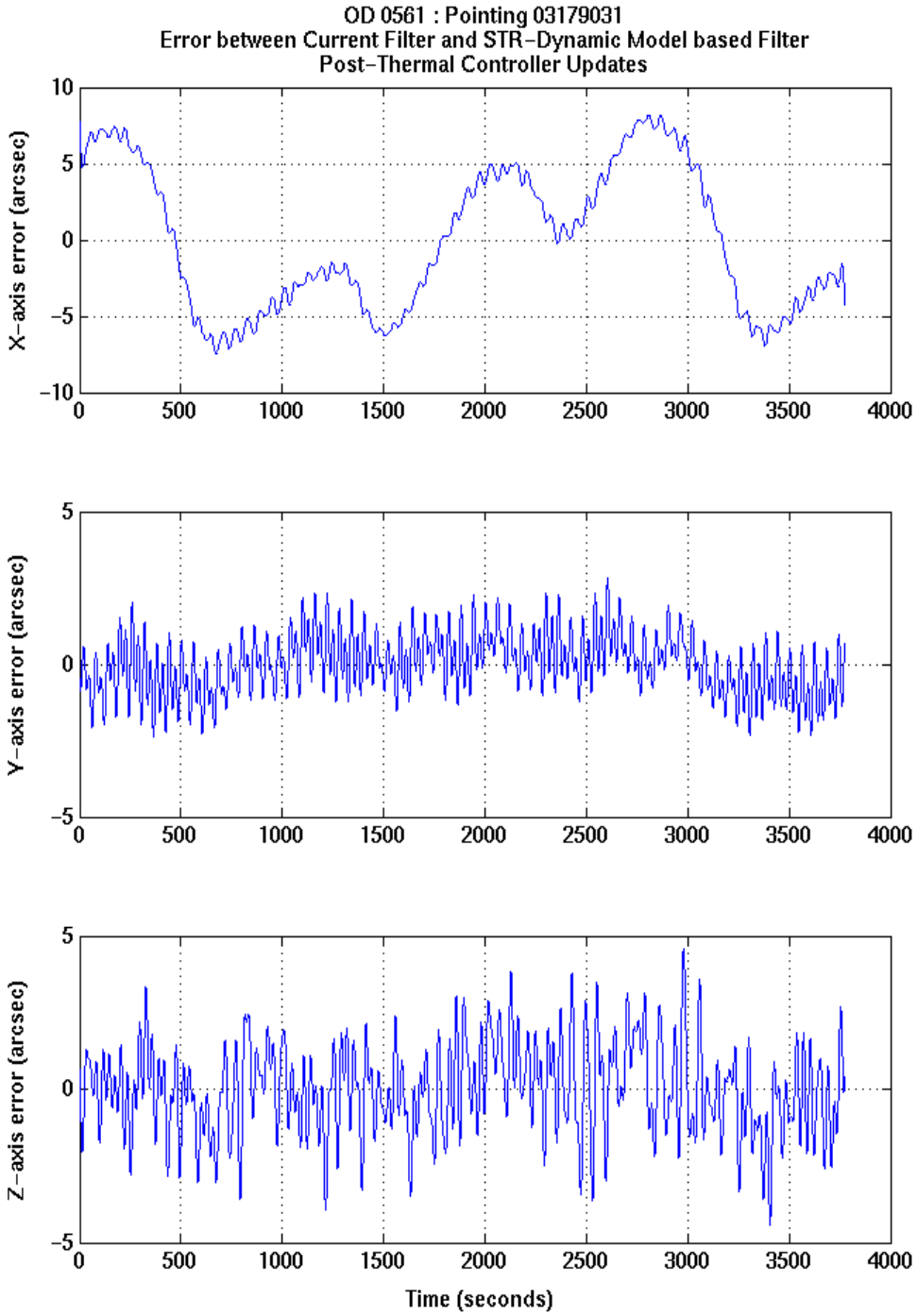

FIGURE 49: Current filter versus STR-Dynamic model based filter comparison: sorption cooler internal disturbances not estimated

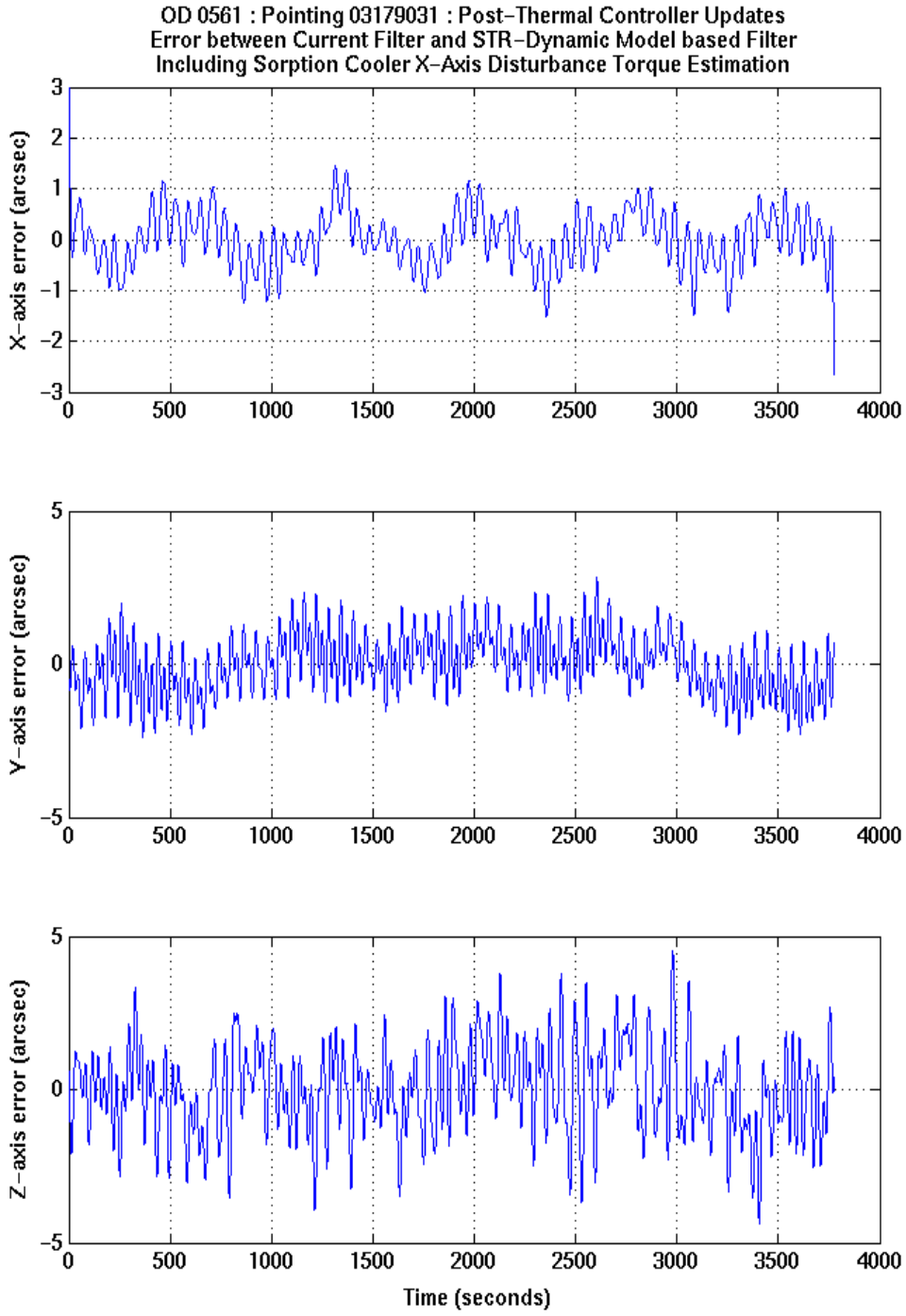

FIGURE 50: Current filter versus STR-Dynamic model based filter comparison: sorption cooler internal disturbances estimated.

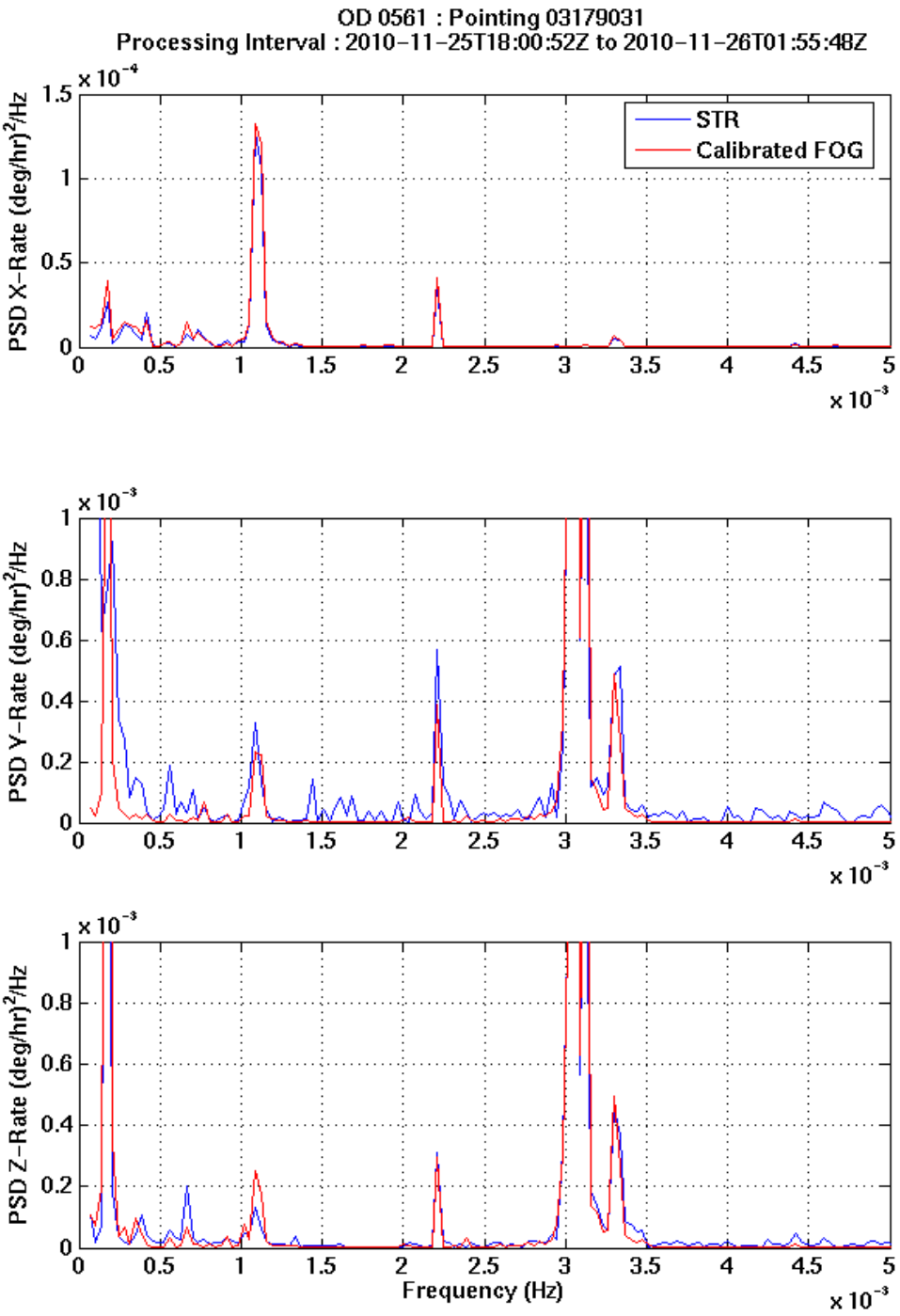

FIGURE 51: STR/FOG Angular Rate PSDs

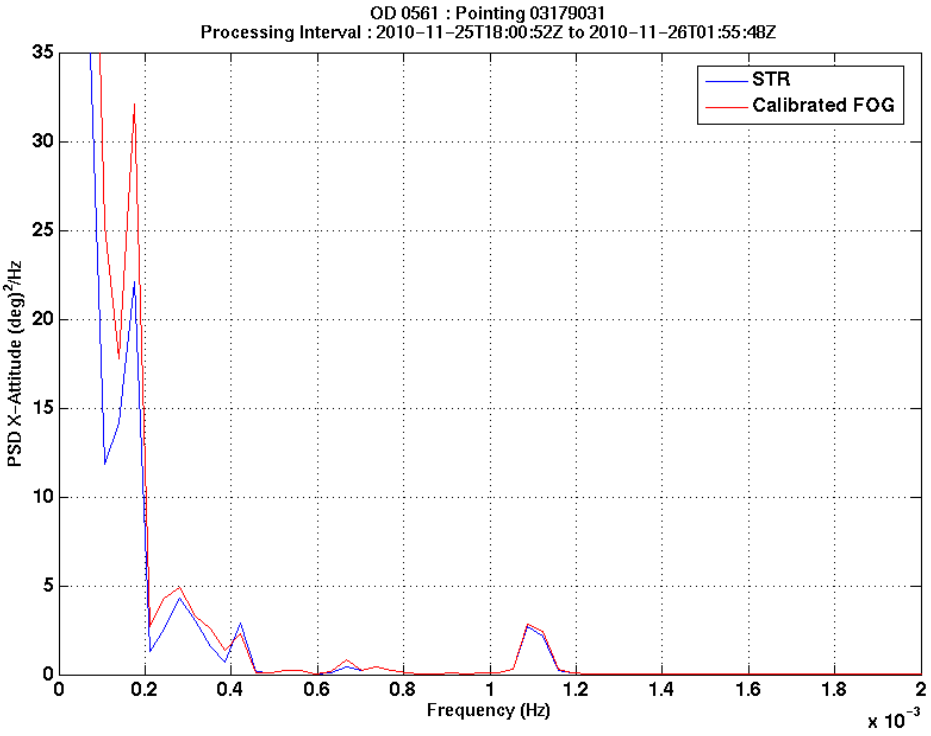

FIGURE 52: STR/FOG X-Axis Integrated Angular Rate PSD

4.3 Nominal Re-orientation Slews - Angular Momentum Control Mode

In this section, the performances of the STR-FOG filter (Section 2.4) and STR-dynamic model based filter (Section 2.5) are assessed based on data processed during a nominal re-orientation slew in OD 0561. Now the current filter can only be used to filter star tracker attitude quaternion data during periods where there are no thruster actuations and so it is not possible to perform the same comparisons of Sections 4.1 and 4.2. It is only possible to make a comparison of filtered versus unfiltered attitude data and a comparison of STR-FOG filter and STR-dynamic model based filter.

The errors between the STR-FOG based filtered and unfiltered data are shown in Figure 53. Also shown in this figure are the 4σ thresholds computed using these residuals.

Figure 54 shows the evolution of the body angular rates that have been determined using calibrated FOG angular rate data.

The errors between the STR-Dynamic Model based filtered and unfiltered data are shown in Figure 55. Also shown in this figure are the 4σ thresholds computed using these residuals.

Figure 56 shows the evolution of the body angular rates that have been determined using raw STR attitude quaternion measurements and calibrated FOG angular rate data.

Finally, a comparison between both STR-FOG and STR-Dynamic Model based filters is shown in Figure 57, which shows that both methods can be used to provide filtered data during nominal slews in HCM.

The algorithm rapidly converged with two iterations, but the dynamic model based filter is quite sensitive to the value of the spacecraft inertia tensor that is used. A further 2 iterations were required to reduce the norm of the state vector correction to below a specified threshold of 1.0E-10. In no cases were there any poorly observable cases where the estimation process diverged.

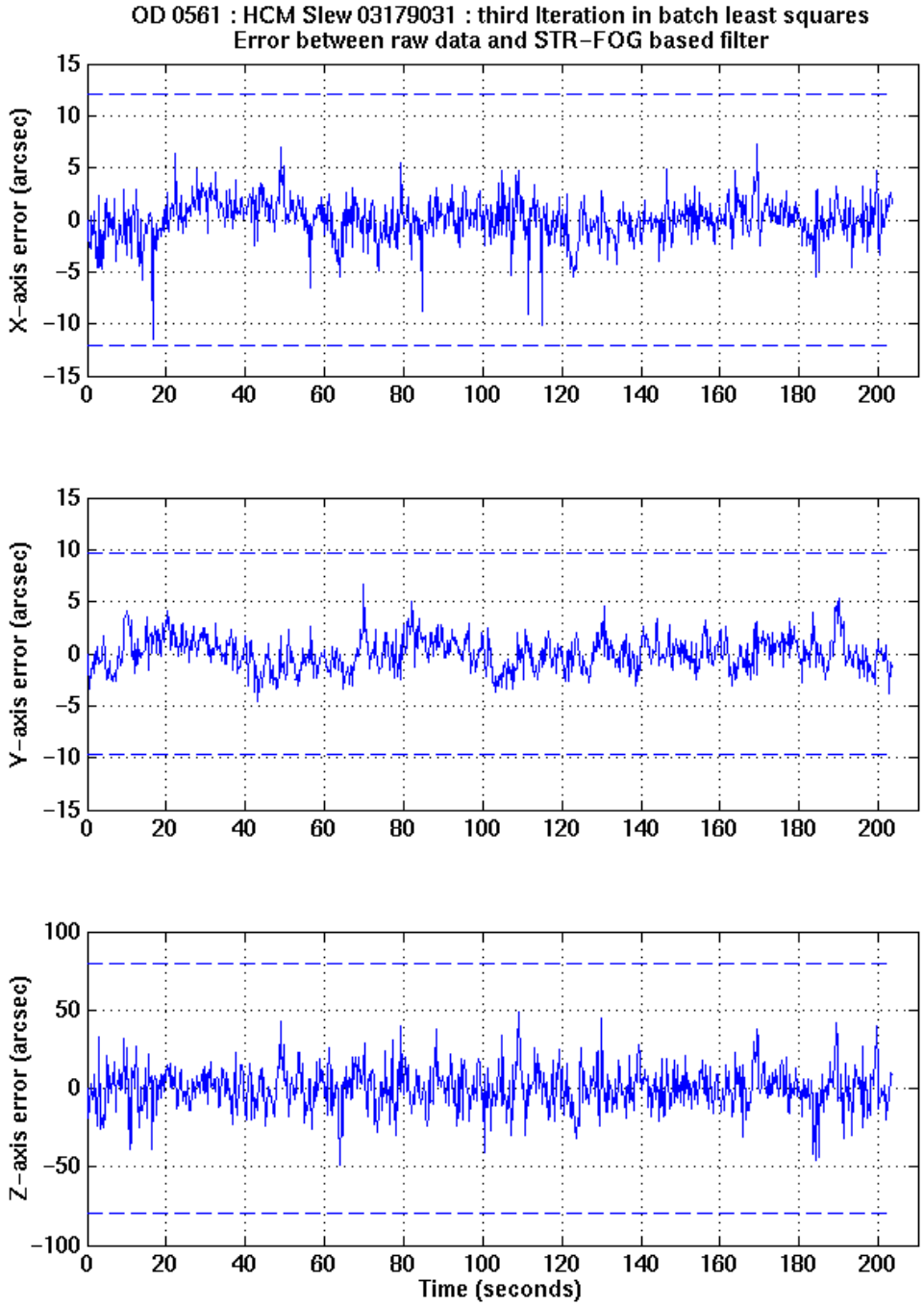

FIGURE 53: STR-FOG based filter versus raw STR attitude quaternion data comparison

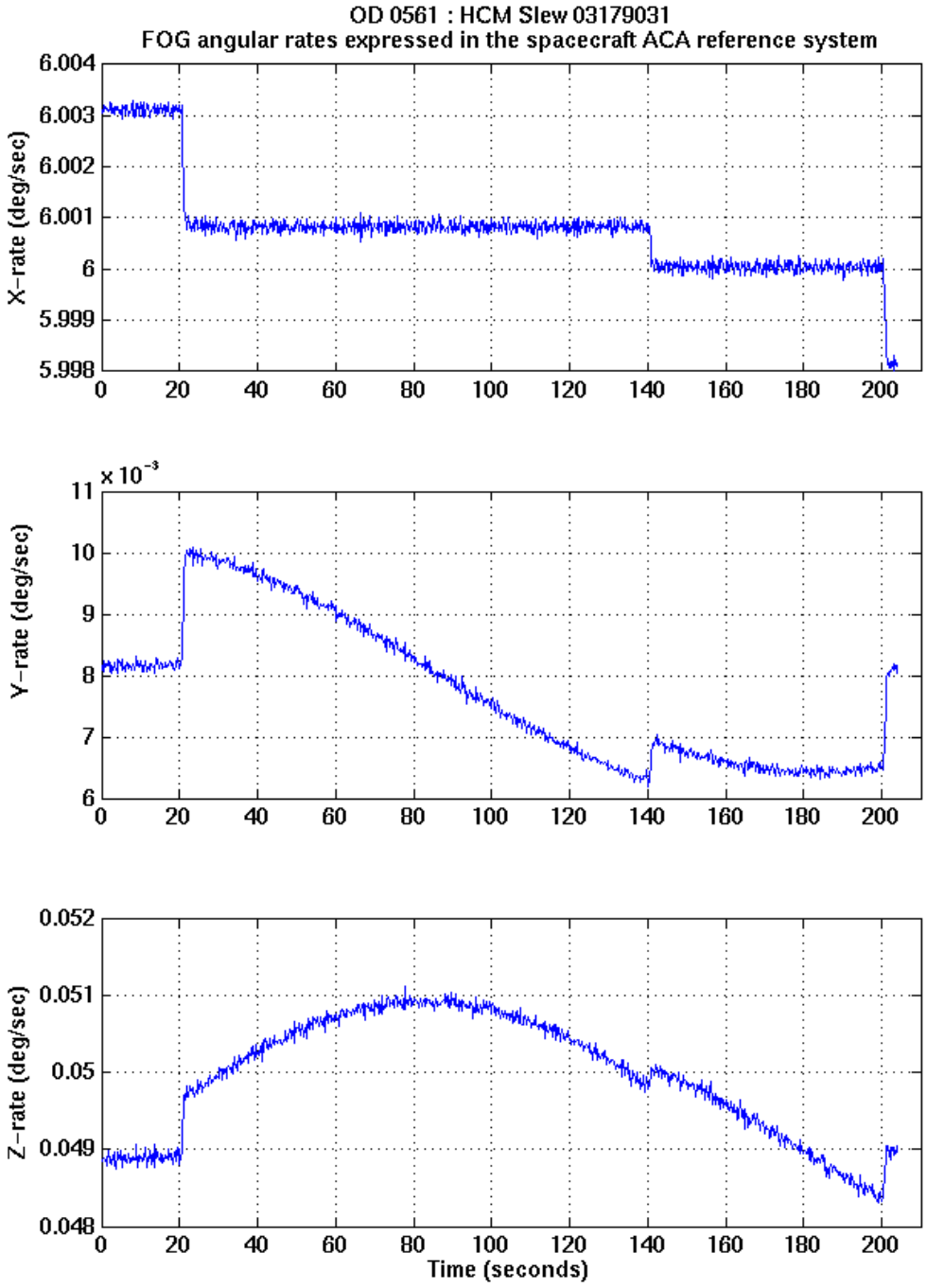

FIGURE 54: Body axis angular rates derived from calibrated FOG angular rate data

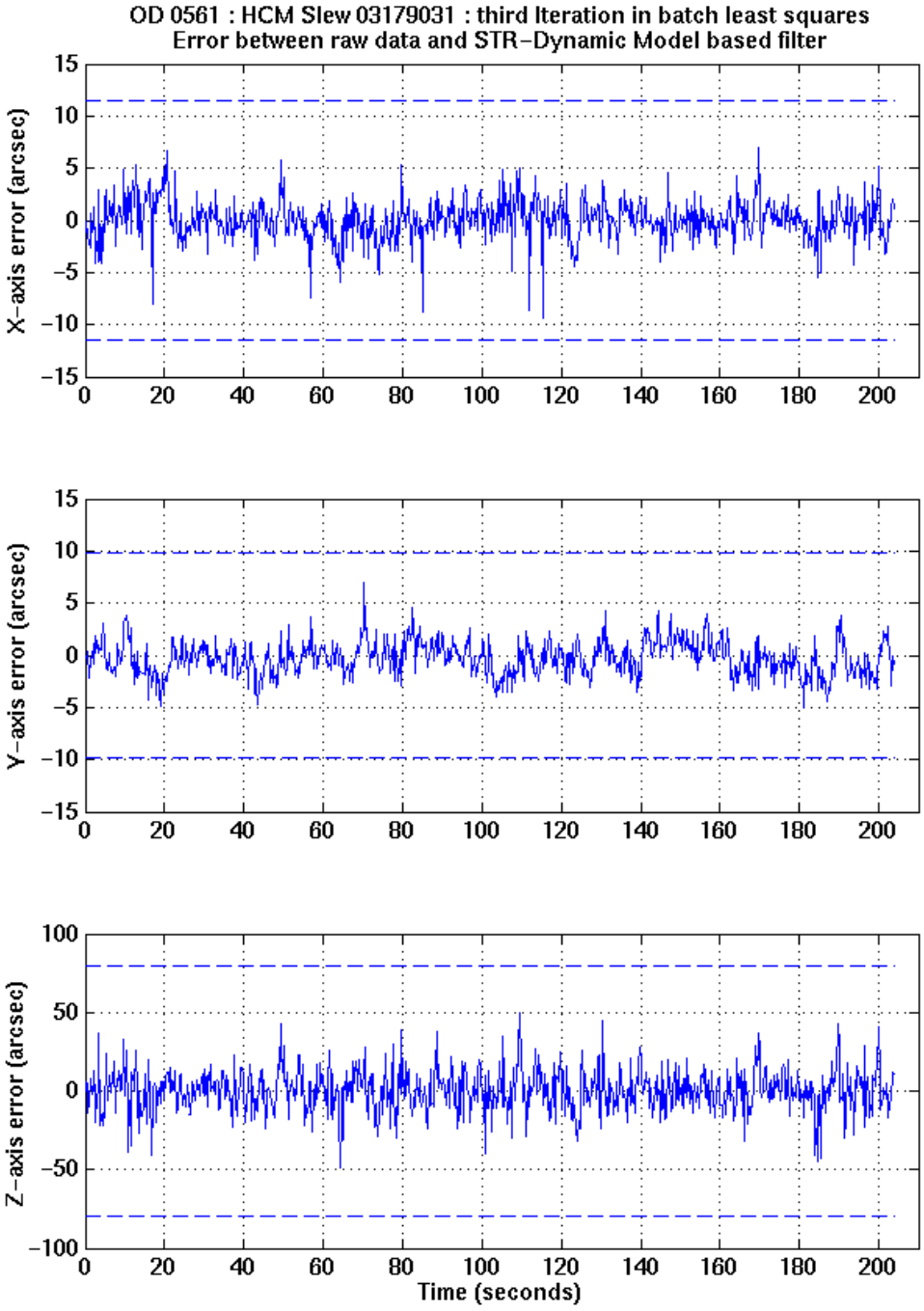

FIGURE 55: STR-Dynamic Model based filter versus raw STR attitude quaternion data comparison

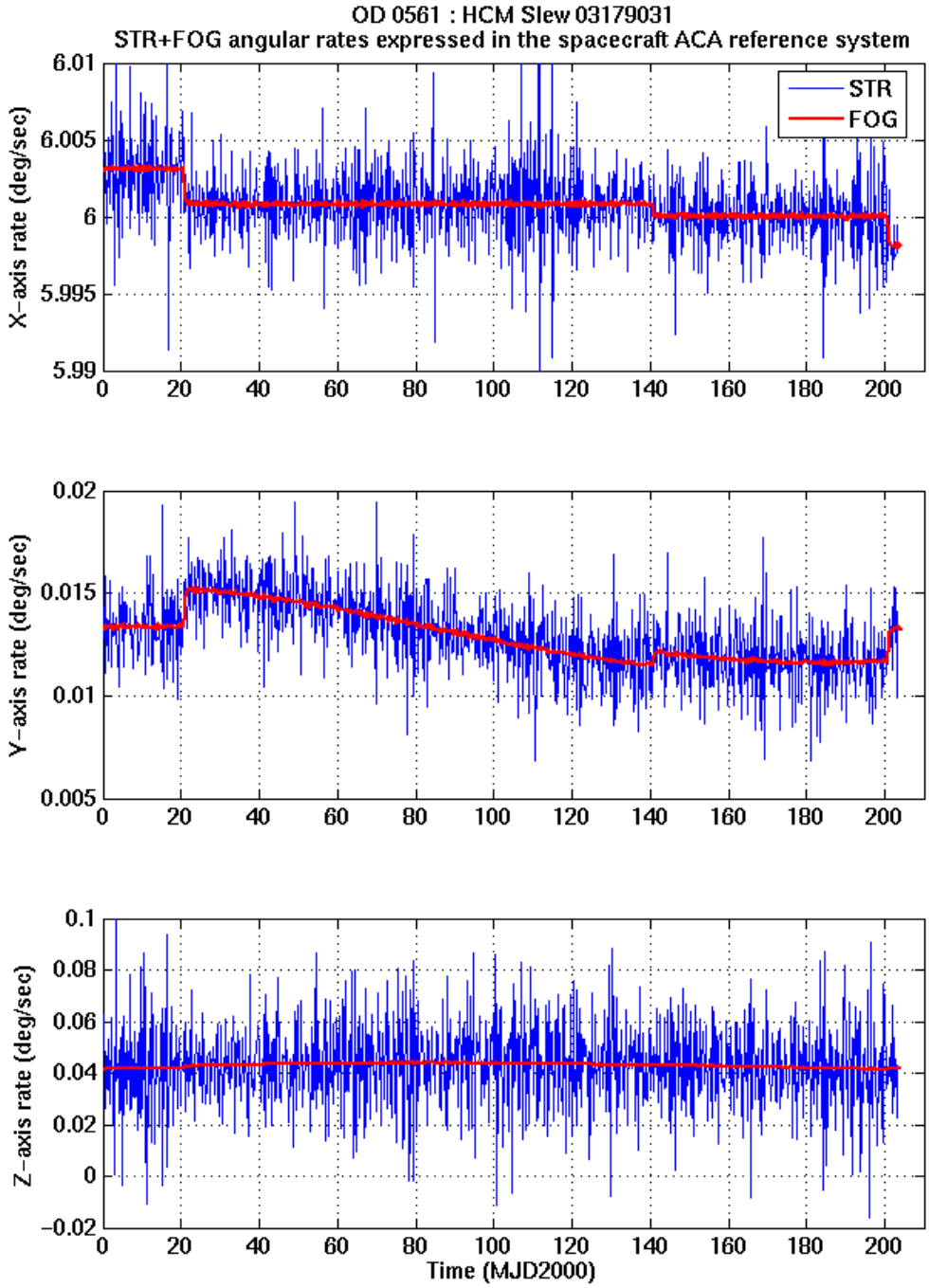

FIGURE 56: Body axis angular rates derived from STR and calibrated FOG angular rate data

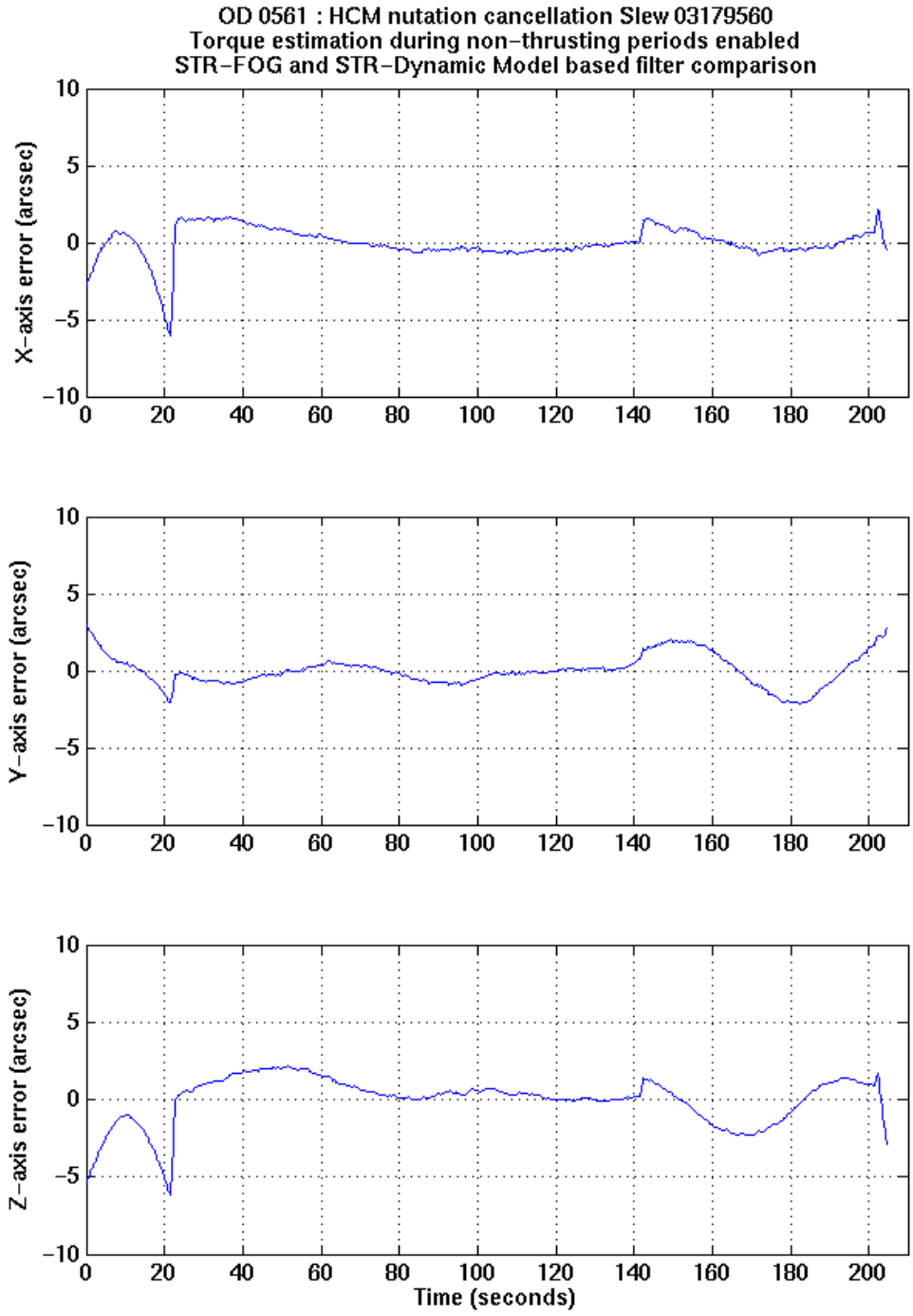

FIGURE 57: STR-FOG based filter versus STR-Dynamic Model based filter comparison

4.4 Pre Thermal Control Updates - Post Delta-V Manoeuvres in OCM

In this section, the performances of the STR-FOG filter from Section 2.2 and the STR-dynamic model based filter from Section 2.7 are assessed based on data processed during free running mode in OCM after the delta-V manoeuvre in OD 0247. This corresponds to a period prior to the thermal controller updates.

4.4.1 Fibre Optic Gyro Based Estimation Algorithm

The errors, $\delta\underline{\theta}$, are shown below in Figure 58. As presented previously for the science mode pointing, it can be seen from these results that the thermal environment of the star tracker affects the consistency between the current filter and the STR-FOG based filter. Again, as for the science mode pointings, it is unclear how much the thermal environment affects the FOG in this case.

4.4.2 Dynamic Model Based Estimation Algorithm

The errors, $\delta\underline{\theta}$, for this case are shown in below Figure 59 and as before for the science mode pointing, a similar periodic signal in the $\delta\theta_x$ error angle, which is not observed in the STR-FOG based filter results is present.

There is a weak correlation observable between the angle errors in Figures 58 and 59. As mentioned for the STR-FOG based filter case of processing the science mode pointing prior to the thermal control updates, that spin frequency components are pre-dominant in the error angle plots of the STR-FOG based filter, which is less so in the case of the STR-dynamic model based filter. This could be due to the fact that the thermal environment is affecting the FOG as well.

A plot of the nutation angle evolution for this case is shown in Figure 60. The variation is due to the fact that we have asymmetric transverse inertias. The relationship between the minimum and maximum nutation angle is given in Appendix A.

The main results of this section are to compare the inertia tensor calibration algorithms. Table 7 shows the initial estimates based on prediction prior to the manoeuvre along with estimated quantities using the current algorithm described in Section 2.2 and estimated quantities based on the algorithm described in Section 2.7. It can be seen that reasonable agreement is achieved between the two methods.

The algorithm rapidly converged with two iterations. A further 5 iterations were required to reduce the norm of the state vector correction to below a specified threshold of 1.0E-10. In no cases were there any poorly observable cases where the estimation process diverged.

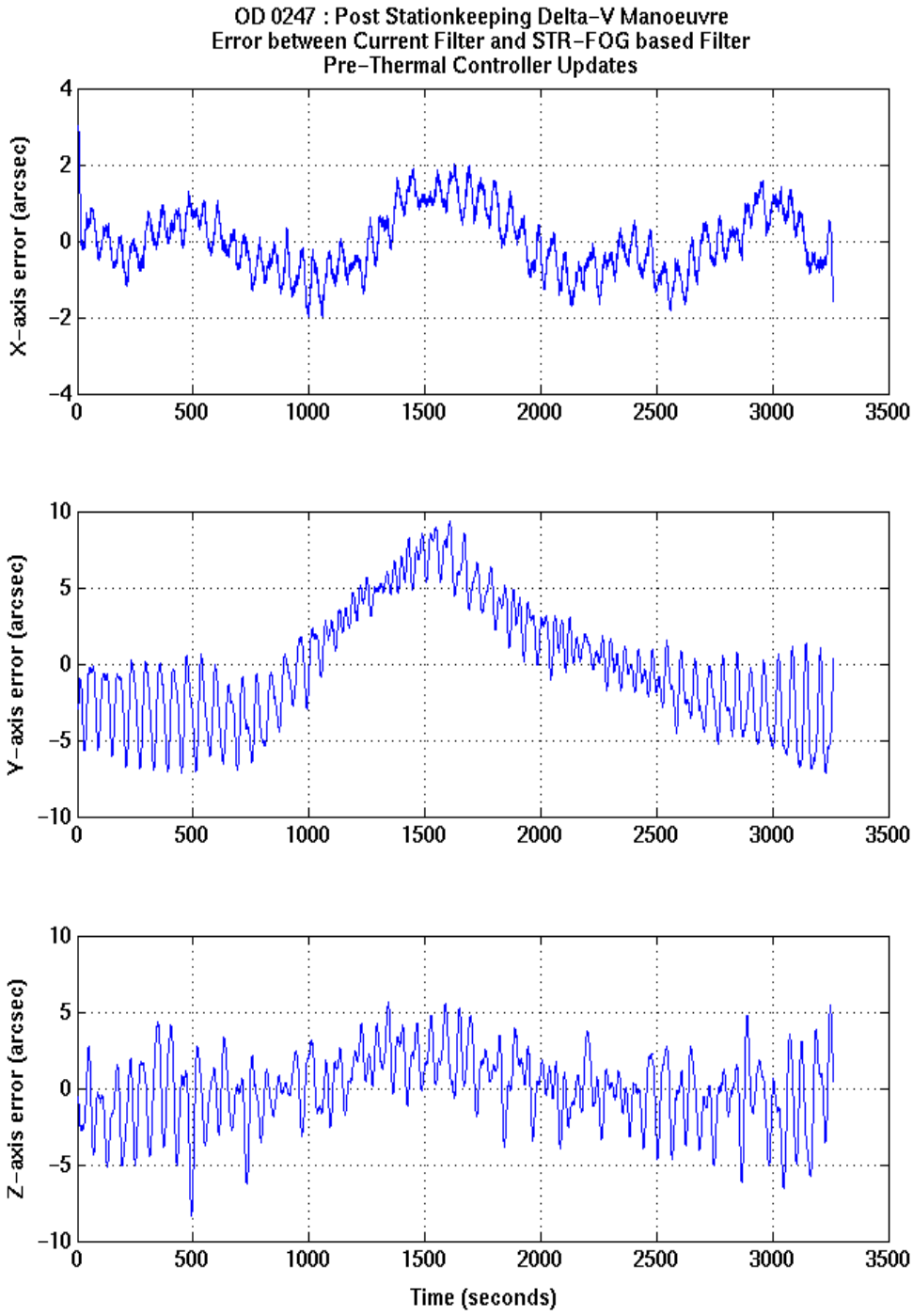

FIGURE 58: Current filter versus STR-FOG based filter comparison

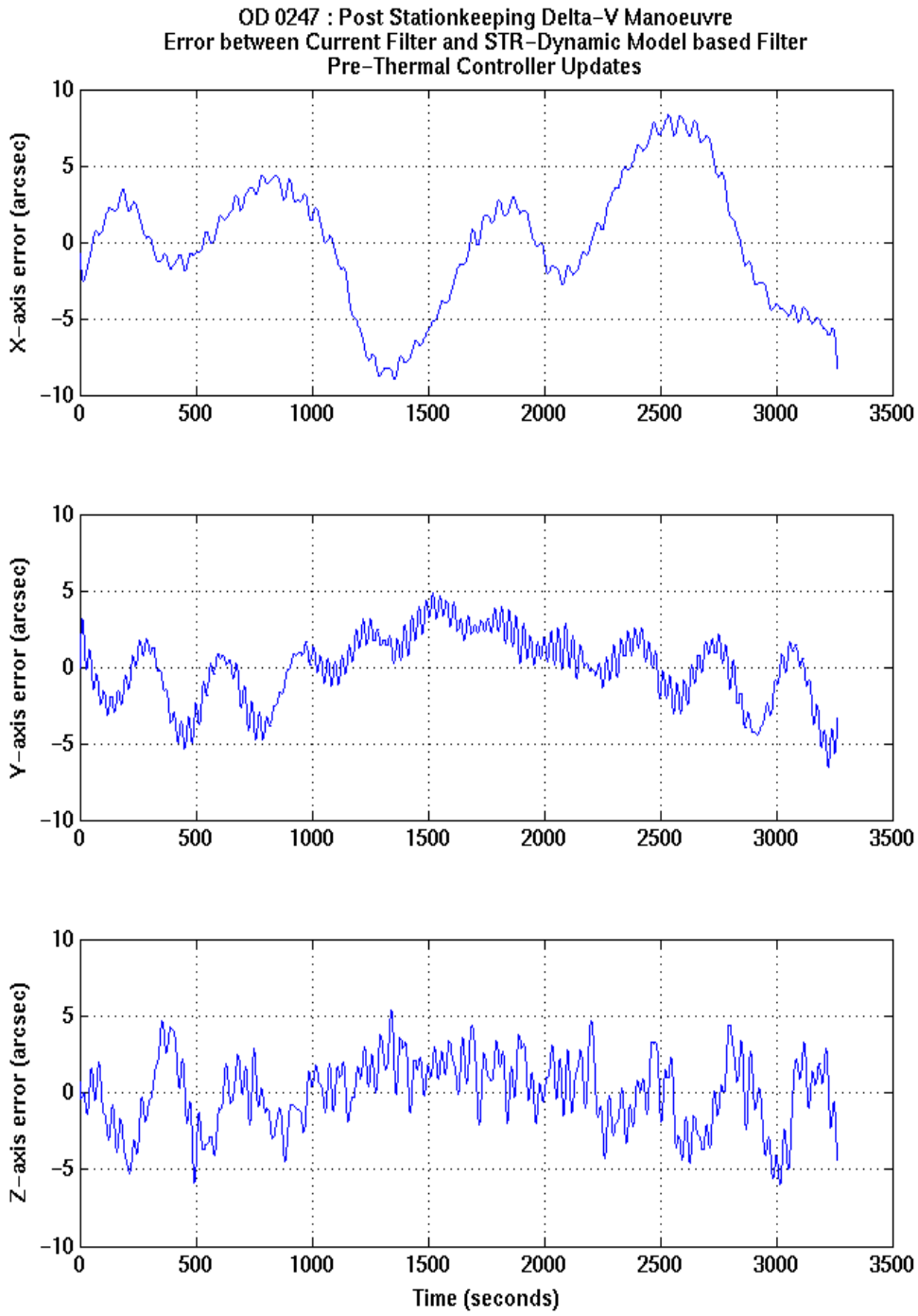

FIGURE 59: Current filter versus STR-Dynamic model based filter comparison

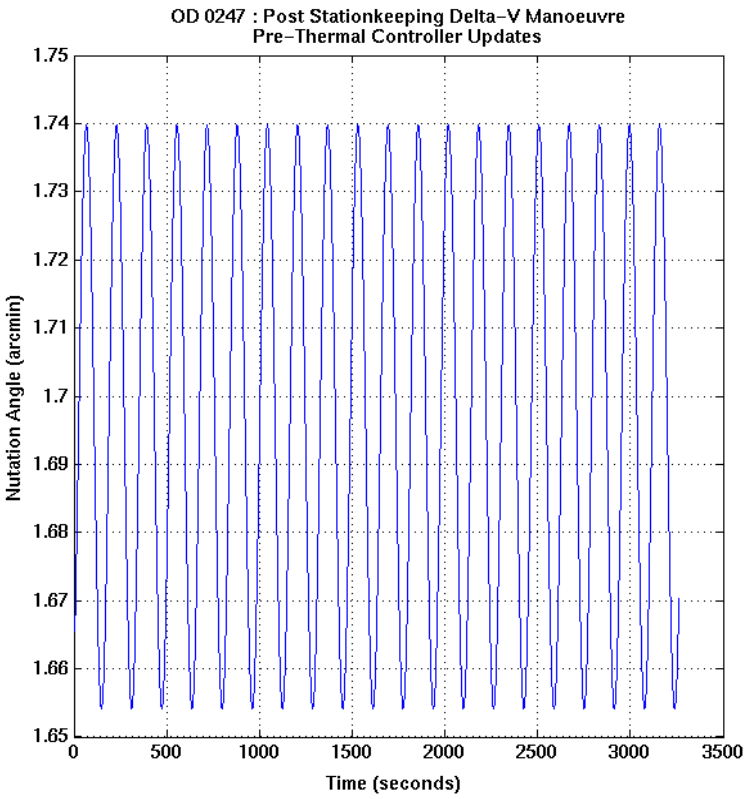

FIGURE 60: OD 0247: Post Delta-V Free Running Mode Nutation Angle

Parameter		Mass Properties Prediction	Current Calibration Algorithm	New Calibration Algorithm
Principal Moments of Inertia	J_1 (kg m^2)	3028.6352	3028.6356	3028.6356
	J_2 (kg m^2)	2579.9910	2577.4007	2577.1821
	J_3 (kg m^2)	2536.8377	2537.8872	2538.4704
Nutation to Spin Ratio	ν_n (-)	0.1836068	0.1839940	0.1839158
Axial Imbalance	Δ (-)	0.0199687	0.0182952	0.0179214
Principal Axis Tilt Angles	ψ_1 (arcmin)	4.513627	4.526050	4.535492
	ψ_2 (arcmin)	-28.334129	-28.296014	-28.269451
	ψ_3 (degree)	25.9219	22.5052	24.1241
Moments of Inertia	J_{xx} (kg m^2)	3028.602	3028.6022	3028.6024
	J_{yy} (kg m^2)	2571.745	2571.6120	2570.7159
	J_{zz} (kg m^2)	2545.117	2543.7092	2544.9698
	J_{xy} (kg m^2)	0.460	0.4866	0.4854
	J_{xz} (kg m^2)	3.963	3.9731	3.9583
	J_{yz} (kg m^2)	16.971	13.9775	14.4449

TABLE 7: Inertia Calibration Comparisons - Pre Thermal Controller Updates

4.5 Post Thermal Control Updates - Post Delta-V Manoeuvres in OCM

In this section, the performances of the STR-FOG and STR-dynamic model based filters are assessed based on data processed during free running mode in OCM after the delta-V manoeuvre in OD 0568. This corresponds to a period after the thermal controller updates.

4.5.1 Fibre Optic Gyro Based Estimation Algorithm

The errors, $\delta\underline{\theta}$, are shown in below Figure 61. As presented previously for the science mode pointing, it can be seen from these results that updates to the thermal controller has improved the consistency between the current filter and the STR-FOG based filter.

4.5.2 Dynamic Model Based Estimation Algorithm

The errors, $\delta\underline{\theta}$, for this case are shown in below Figure 62.

As presented previously for the science mode pointing, a similar periodic signal in the $\delta\theta_x$ error angle, which is not observed in the STR-FOG based filter results is present.

A plot of the nutation angle evolution for this case is shown in Figure 63. The variation is due to the fact that we have asymmetric transverse inertias. The relationship between the minimum and maximum nutation angle is given in Appendix A.

The main results of this section are to compare the inertia tensor calibration algorithms. Table 8 shows the initial estimates based on prediction prior to the manoeuvre along with estimated quantities using the current algorithm described in Section 2.2 and estimated quantities based on the algorithm described in Section 2.7. It can be seen that reasonable agreement is achieved between the two methods.

The algorithm rapidly converged with two iterations. A further 5 iterations were required to reduce the norm of the state correction to below a specified threshold of 1.0E-10. In no cases were there any poorly observable cases where the estimation process diverged.

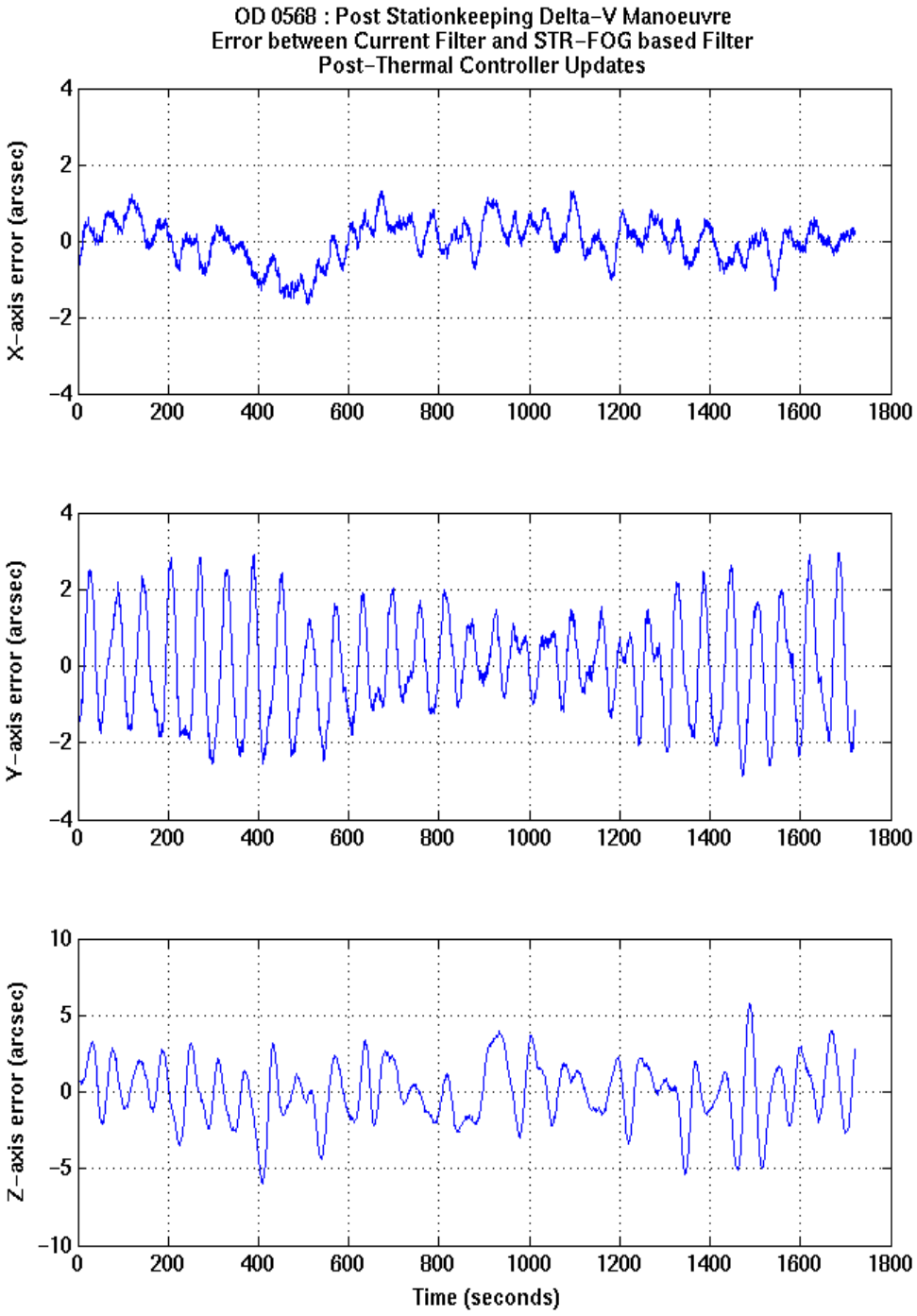

FIGURE 61: Current filter versus STR-FOG based filter comparison

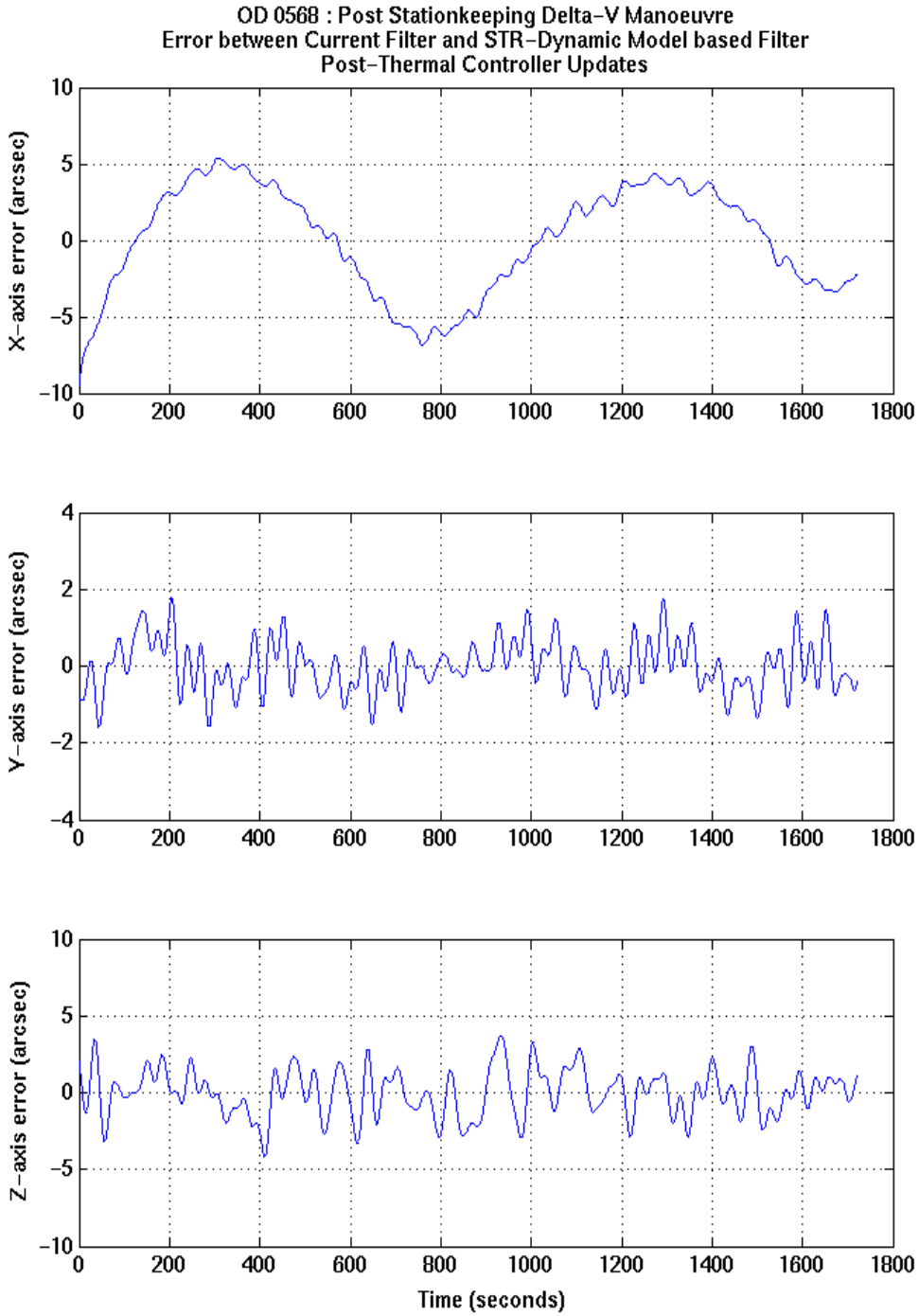

FIGURE 62: Current filter versus STR-Dynamic model based filter comparison

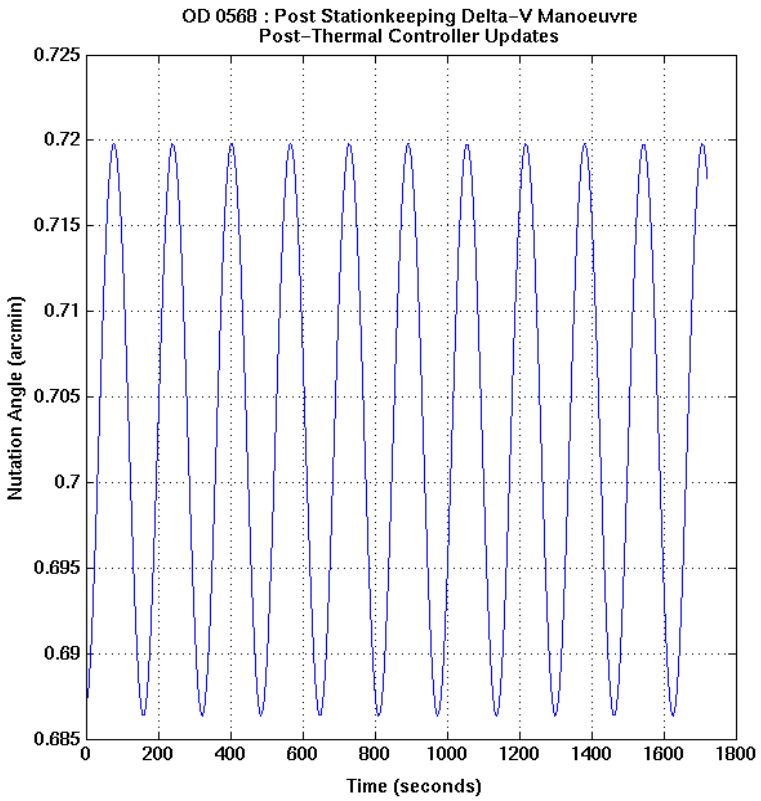

FIGURE 63: OD 0568: Post Delta-V Free Running Mode Nutation Angle

Parameter		Mass Properties Prediction	Current Calibration Algorithm	New Calibration Algorithm
Principal Moments of Inertia	J_1 (kg m^2)	3022.469	3022.4693	3022.4689
	J_2 (kg m^2)	2574.532	2576.3553	2576.7422
	J_3 (kg m^2)	2533.489	2529.6264	2529.66260
Nutation to Spin Ratio	ν_n (-)	0.1832505	0.1836733	0.1835717
Axial Imbalance	Δ (-)	0.0190187	0.0216713	0.0218303
Principal Axis Tilt Angles	ψ_1 (arcmin)	4.533130	4.554814	4.536182
	ψ_2 (arcmin)	-28.257155	-28.240129	-28.257358
	ψ_3 (degree)	27.4958	31.4670	31.5633
Moments of Inertia	J_{xx} (kg m^2)	3022.436	3022.4365	3022.4361
	J_{yy} (kg m^2)	2565.784	2563.6225	2563.8432
	J_{zz} (kg m^2)	2542.270	2542.3921	2542.5944
	J_{xy} (kg m^2)	0.464	0.4370	0.4325
	J_{xz} (kg m^2)	3.925	3.9162	3.9168
	J_{yz} (kg m^2)	16.813	20.8102	21.0021

TABLE 8: Inertia Calibration Comparisons - Post Thermal Controller Updates

5 Conclusions

New batch filtering algorithms have been proposed, developed and tested. The first of these is an STR-FOG based filter, the second and third are STR-dynamic model based filters, that can be used to filter data during nominal re-orientation slews in HCM and stable pointings in SCM, respectively.

The current filter used by the operational AHF generation subsystem and the new filters, have all been prototyped in MATLAB and end-to-end tested. The test data was generated for a complete OD using the Planck HPTDG. Commands were extracted from the APPL/APF for OD 0390. The new filters are able to filter out STR spatial biases significantly better than the current filter. The current filter passes all low frequency STR alignment variations that are within the filter passband. The new filters reject this provided that the period of the variation is less than the period of the stable pointing period in SCM, for the data that is being filtered. If this is not the case, the variations are not filtered by the new filters either. The new STR dynamic model based filter used to filter data during a nominal re-orientation slew in HCM has also been validated using data generated by the HPTDG. The accuracy achieved using this is very good and can be used to provide filtered data during the periods where the spacecraft is performing nominal scanning law slews. Finally a complete end-to-end validation of the current algorithm and the new dynamic model based algorithm, used to estimate the spacecraft inertia tensor, has been performed using HPTDG data. The results obtained for the current and new algorithms are comparable.

The current filtering algorithm and new filters have also been tested using in-flight STR and FOG telemetry data. Due to the similarity of the results obtained by processing simulated and in-flight data, when comparing the current filter with the STR dynamic model based filter (SCM) outputs, it is concluded that certain alignment variations can be filtered out using the new filters. Also, the new filters provide excellent performances with respect to the filtering of STR spatial biases. The new filters have been assessed using data from two science mode pointings, data taken before and after the thermal controller updates. In the case prior to the thermal controller updates, it has been demonstrated that the new filters partially reject the low frequency errors, that result from changes in the STR alignment. The results from the 3 alignment variation cases considered, show similar results to those obtained with the HPTDG simulated data. However, for the STR-FOG based filter, it remains unclear how much the FOG is affected by the pre thermal controller update environment. From the frequency analysis of the angular rates and integrated angular rates, one can see all the attitude disturbances on both transverse and spin axes, with the main frequency correlated to the sorption cooler compressor cycle period. All other frequencies observed are simple multiples of this basic frequency. The variations on the X-axis error, that result from these disturbances, correspond roughly to a variation of 6 gram•m^2 in the X-axis principal moment of inertia. The updates made to the STR dynamic model based filter (SCM), for internal disturbance torque estimation due to the sorption cooler subsystem, show a significant improvement with regards attitude estimation about the spacecraft X-axis. Results are now comparable to those obtained with the STR-FOG based filter. Also shown are the results for nutation angle reconstruction performance, which are completely in line with those obtained using the current filter results.

In the case after the thermal controller updates, there are clear improvements to attitude reconstruction in general. It is also noted that the current filter performances are now comparable with the two new filters and vice-versa.

Also tested using in-flight data are the STR-FOG and STR dynamic model (HCM) based filters by processing data during a nominal re-orientation slew in HCM. Similar performances are achieved to those obtained using the simulated data.

Finally, it has been demonstrated that the dynamic model based spacecraft inertia tensor estimator provides consistent results with the current algorithm used to estimate the spacecraft inertia tensor. This has been tested using in-flight data collected in OCM after a delta-V has been performed. As with the science mode examples, two cases have been considered prior to (OD 0247) and one after (OD 0568) the thermal controller updates. Results with the new filter are close to those obtained using the current algorithm, that is used operationally.

Table 9 gives a summary of the capabilities and deficiencies of each filtering method in turn.

At the time of writing, the new algorithms are being integrated into the operational Planck Flight Dynamics attitude history file generation. If a unified post mission attitude history reconstruction is agreed, it is highly recommended to use the refined algorithms instead of the baseline algorithm for improved science data quality.

.

Disturbances	Subclass	Current filtering algorithm Section 2.1	STR-FOG based filter Section 2.4	STR-dynamic model based filter (SCM) Section 2.6	STR-dynamic model based filter (Inertia tensor) Section 2.7
STR measurement errors	STR noise	+ Filtered	+ Filtered	+ Filtered	+ Filtered
	STR SEUs (glitches)	+ Filtered, but the efficiency is not as good as the new filters.	+ Filtered	+ Filtered	+ Filtered
	STR spatial biases	- Not filtered	+ Filtered	+ Filtered	+ Filtered
FOG measurement errors	FOG bias uncertainty	0 Not applicable	+ Accounted for	0 Not applicable	0 Not applicable
	FOG bias drift	0 Not applicable	+ Accounted for	0 Not applicable	0 Not applicable
	FOG scale factor/alignment uncertainties	0 Not applicable	+ Accounted for	0 Not applicable	0 Not applicable
Thermoelastic distortions	High frequency distortions whereby the period is much shorter than the dwell period in SCM, but the frequency is above the current filter low pass cutoff frequency	+ Filtered	+ Filtered	+ Filtered	+ Filtered
	Low frequency distortions whereby the period is shorter than the dwell period in SCM, but the frequency is below the current filter low pass cutoff frequency	- Not filtered	+ Filtered	+ Filtered	+ Filtered
	Very low frequency distortions whereby the period is longer than the dwell period in SCM and the frequency is below the current filter low pass cutoff frequency	- Not filtered	- Not filtered	- Not filtered	- Not filtered

TABLE 9: Summary of the capabilities and deficiencies of Planck attitude filtering methods on a scale $+ \pm - 0$

Disturbances	Subclass	Current filtering algorithm Section 2.1	STR-FOG based filter Section 2.4	STR-dynamic model based filter (SCM) Section 2.6	STR-dynamic model based filter (Inertia tensor) Section 2.7
External torques	Inertially fixed	+ Accounted for	+ Accounted for since FOG is an excellent dynamic model replacement	+ Accounted for	+ Accounted for
	Body fixed	+ Accounted for	+ Accounted for since FOG is an excellent dynamic model replacement	- Not accounted for	- Not accounted for
Inertia tensor errors and unmodelled dynamics	Inertia ratio uncertainties	- Not accounted for	+ Accounted for since FOG is an excellent dynamic model replacement	- Not accounted for	- Accounted for
	Inertia ratio shifts	- Not accounted for	+ Accounted for since FOG is an excellent dynamic model replacement	- Not accounted for	+/- Accounted for, but it only accounts for variations that are a linear function of time
	Principal axis offsets	+ Accounted for	+ Accounted for since FOG is an excellent dynamic model replacement	- Not accounted for	+ Accounted for.This filter is also used to estimate the principal axis azimuth angle as well
	Principal axis shifts	+ Accounted for, but it only accounts for variations that are a linear function of time.	+ Accounted for since FOG is an excellent dynamic model replacement	- Not accounted for	+ Accounted for but it only accounts for a linear variation
	Propellant slosh	+/- Only accounted for if the slosh frequencies are below the low pass cutoff frequency	+ Accounted for since FOG is an excellent dynamic model replacement	- Not accounted for	+ Accounted for but it only accounts for a linear variation

TABLE 9: Summary of the capabilities and deficiencies of Planck attitude filtering methods on a scale $+ \pm - 0$

Appendix A Current Inertia Tensor Calibration Algorithm

This appendix presents an alternative derivation of the current algorithm used to estimate the spacecraft inertia tensor, that is described in Section 3.3.9 (FCP-P-D-MAINT procedure) of [13]. Annex A of [12] also gives several relevant definitions and conventions.

In the principal axis reference system, it can be shown that for an asymmetric rigid body spinning about it's major principal axis of inertia (X-axis), that the momentum ellipse under torque free motion is given by:-

$$\frac{H_2^2}{H^2\left(\frac{J_1J_2}{J_1-J_2}\right)\left(\frac{2E}{H^2}-\frac{1}{J_1}\right)}+\frac{H_3^2}{H^2\left(\frac{J_1J_3}{J_1-J_3}\right)\left(\frac{2E}{H^2}-\frac{1}{J_1}\right)}=1 \tag{A.1}$$

where

$$\begin{aligned} H^2 &= J_1^2\omega_1^2+J_2^2\omega_2^2+J_3^2\omega_3^2 \\ 2E &= J_1\omega_1^2+J_2\omega_2^2+J_3\omega_3^2 \end{aligned} \tag{A.2}$$

and

J_1, J_2, J_3 are the spacecraft principal axis moments of inertia.

$\omega_1, \omega_2, \omega_3$ are the true angular rates expressed in the principal axis system.

H_1, H_2, H_3 are the true angular momenta in the principal axis reference system.

The angular momenta expressed in the principal axis reference system are given by:-

$$\begin{aligned} H_1 &= J_1\omega_1 \\ H_2 &= J_2\omega_2 \\ H_3 &= J_3\omega_3 \end{aligned} \tag{A.3}$$

Substituting (A.3) into (A.1) yields:-

$$A\omega_2^2+B\omega_3^2=1 \tag{A.4}$$

where

$$\begin{aligned} A &= \frac{J_2(J_1-J_2)}{2EJ_1-H^2} \\ B &= \frac{J_3(J_1-J_3)}{2EJ_1-H^2} \end{aligned} \tag{A.5}$$

The angular rates expressed in the principal axis reference system are related to the pseudo principal axis angular rates as follows:-

$$\begin{aligned} \omega_1 &= \omega_1' \\ \omega_2 &= \omega_2'\cos\psi_3+\omega_3'\sin\psi_3 \\ \omega_3 &= -\omega_2'\sin\psi_3+\omega_3'\cos\psi_3 \end{aligned} \tag{A.6}$$

where ψ_3 is the principal axis azimuth angle. Substituting (A.6) into (A.4) yields:-

$$A'\omega_2'^2+B'\omega_3'^2+C'\omega'_2\omega'_3=1 \tag{A.7}$$

where

$$\begin{aligned} A' &= \frac{1}{2}[(A+B)+(A-B)\cos 2\psi_3] \\ B' &= \frac{1}{2}[(A+B)-(A-B)\cos 2\psi_3] \\ C' &= (A-B)\sin 2\psi_3 \end{aligned} \tag{A.8}$$

The algorithms in Chapter 5 of [8] are then to compute the pseudo principal axis angular rates, from which the principal axis tilts ψ_1, ψ_2 can be computed. Then, using (A.7), an over-determined linear system is constructed, which is then solved to determine the coefficients A', B', C'.

Then from (A.8), the principal axis azimuth angle ψ_3 can be determined as follows:-

$$\psi_3 = \frac{1}{2}\text{atan}2(C', (A' - B')) \tag{A.9}$$

and it can be shown that:-

$$\begin{aligned} A &= \frac{1}{2}[(1+\cos 2\psi_3)A' + (1-\cos 2\psi_3)B' + C'\sin 2\psi_3] \\ B &= \frac{1}{2}[(1-\cos 2\psi_3)A' + (1+\cos 2\psi_3)B' - C'\sin 2\psi_3] \end{aligned} \tag{A.10}$$

where the parameters (A,B) are related to the semi-major/minor axes of the momentum ellipse. So it follows from (A.5) that:-

$$\frac{A}{B} = \frac{J_2(J_1 - J_2)}{J_3(J_1 - J_3)} > 0 \tag{A.11}$$

Also using the algorithm described in Section 3.3.9.4.2 of [13], the nutation to spin rate ratio is estimated, which can be expressed as a function of the principal axis moments of inertia as:-

$$\nu_n = \sqrt{\frac{(J_1 - J_2)(J_1 - J_3)}{J_2 J_3}} \tag{A.12}$$

So the transverse principal axis moments of inertia can be obtained from:-

$$\begin{aligned} J_2 &= J_1\left(\frac{k_2 - 1}{k_1 k_2 - 1}\right) \\ J_3 &= J_2\left(\frac{k_1 - 1}{k_1 k_2 - 1}\right) \end{aligned} \tag{A.13}$$

where

$$\begin{aligned} k_1 &= \nu_n\sqrt{\frac{B}{A}} = \left(\frac{J_1 - J_3}{J_2}\right) > 0 \\ k_2 &= \nu_n\sqrt{\frac{A}{B}} = \left(\frac{J_1 - J_2}{J_3}\right) > 0 \end{aligned} \tag{A.14}$$

The mass properties prediction is used to provide an estimate of the major axis principal moment of inertia J_1.

The complete inertia tensor can then be recovered using the estimated principal axis tilts ψ_1, ψ_2 and the principal axis azimuth angle ψ_3, as follows:-

$$J_B = T_{PB}^{-1} J_P T_{PB} = T_{PB}^{T} \begin{bmatrix} J_1 & 0 & 0 \\ 0 & J_2 & 0 \\ 0 & 0 & J_3 \end{bmatrix} T_{PB} \tag{A.15}$$

where the transformation from the body axis reference system to the principal axis reference system can be represented as a (3-2-1) Euler rotation sequence $[\psi_1, \psi_2, \psi_3]$, where:-

- ψ_1, ψ_2 are the tilt angles of the spin axis w.r.t. the nominal spin axis (X_B)
- ψ_3 is the azimuth angle

The transformation from the body axis reference system to the principal axis reference system can be performed using the following transformation matrix:-

$$T_{PB} = \begin{bmatrix} 1 & 0 & 0 \\ 0 & \cos\psi_3 & \sin\psi_3 \\ 0 & -\sin\psi_3 & \cos\psi_3 \end{bmatrix} \begin{bmatrix} \cos\psi_2 & 0 & -\sin\psi_2 \\ 0 & 1 & 0 \\ \sin\psi_2 & 0 & \cos\psi_2 \end{bmatrix} \begin{bmatrix} \cos\psi_1 & \sin\psi_1 & 0 \\ -\sin\psi_1 & \cos\psi_1 & 0 \\ 0 & 0 & 1 \end{bmatrix} \tag{A.16}$$

From which, the direction of the spin axis (principal X-axis with the absence of nutation) in the body axis reference system is therefore given by:-

$$\overrightarrow{X_P} = \begin{bmatrix} \cos\psi_2 \cos\psi_1 \\ \cos\psi_2 \sin\psi_1 \\ -\sin\psi_2 \end{bmatrix} \tag{A.17}$$

In the absence of nutation, this is aligned with the angular momentum vector.

For a nutating spacecraft, the nutation angle is given by:-

$$\sin\theta = \frac{\sqrt{H_2^2 + H_3^2}}{H} \tag{A.18}$$

where the relationship between the minimum and maximum nutation angles is given as follows:-

$$\sin\theta_{min} = \sqrt{\left(\frac{J_1 J_3}{J_1 - J_3}\right)\left(\frac{2E}{H^2} - \frac{1}{J_1}\right)} \tag{A.19}$$

and

$$\sin\theta_{max} = \sqrt{\left(\frac{J_1 J_2}{J_1 - J_2}\right)\left(\frac{2E}{H^2} - \frac{1}{J_1}\right)} \tag{A.20}$$

From which

$$\sin\theta_{max} = \sqrt{\frac{J_2(J_1 - J_3)}{J_3(J_1 - J_2)}} \sin\theta_{min} \tag{A.21}$$

It follows from (A.21), that for an axisymmetric spacecraft, $(J_2 = J_3)$, the nutation angle is constant.

Appendix B Spacecraft Dynamic Models

This appendix contains a description of the spacecraft dynamic models used within the dynamic model based estimation algorithms. Appendix B.1 describes the model used for the estimation scheme described in Section 2.6 and B.2 describes the model used for the estimation scheme described in Section 2.7.

B.1 Dynamic Model Based Estimation Algorithm (SCM)

In this case, the Planck spacecraft is modelled as a rigid body with a periodic internal torque about the principal X-axis. The equations of motion in the principal axis reference system are given as:-

$$\dot{\underline{\omega}}_P = J_P^{-1}\left(\underline{\tau}_P - \begin{bmatrix}\sum_{i=1}^{5} x_i \\ 0 \\ 0\end{bmatrix} + [[\underline{\omega}_P]]J_P\underline{\omega}_P\right) = f_\omega(\underline{\omega}_P, \underline{\tau}_P, \underline{x}, \omega_{scs}) \tag{B.1}$$

where:-

$\underline{\omega}_P = (\omega_1, \omega_2, \omega_3)$ true angular rate vector expressed in spacecraft principal axes.

$\underline{\tau}_P = (\tau_1, \tau_2, \tau_3)$ true external torque vector expressed in spacecraft principal axes.

$J_P = diag(J_1, J_2, J_3)$ is the principal axis inertia tensor.

x_i is the i^{th} periodic component of the sorption cooler disturbance torque with frequency, $\omega_i = k_i\omega_{scs}$, i=1...5.

ω_{scs} is the compressor cycle frequency.

The sorption cooler disturbance torque periodic components can be expressed as follows:-

$$\begin{aligned} x_i &= A_i\sin(\omega_i t + \varphi_i) \\ \dot{x}_i &= \omega_i A_i\cos(\omega_i t + \varphi_i) \\ \ddot{x}_i &= \omega_i^2 A_i\sin(\omega_i t + \varphi_i) = -\omega_i^2 x_i \end{aligned} \tag{B.2}$$

Linearising (B.1) yields:-

$$\dot{\underline{\omega}}_P = \dot{\hat{\underline{\omega}}}_P + \left(\frac{\partial f_\omega}{\partial \underline{\omega}_P}\right)\delta\underline{\omega}_P + \left(\frac{\partial f_\omega}{\partial \underline{\tau}_P}\right)\delta\underline{\tau}_P + \sum_{i=1}^{5}\left[\left(\frac{\partial f_\omega}{\partial x_i}\right)\delta x_i + \left(\frac{\partial f_\omega}{\partial x_i}\right)\left(\frac{\partial x_i}{\partial \omega_i}\right)\left(\frac{\partial \omega_i}{\partial \omega_{scs}}\right)\delta\omega_{scs}\right] \tag{B.3}$$

where the partial derivatives are computed analytically as:-

$$\begin{aligned} \frac{\partial f_\omega}{\partial \underline{\omega}_P} &= J_P^{-1}([[\underline{\omega}_P]]J_P - [[J_P\underline{\omega}_P]]) \\ \frac{\partial f_\omega}{\partial \underline{\tau}_P} &= J_P^{-1} \end{aligned} \tag{B.4}$$

and

$$\frac{\partial f_\omega}{\partial x_i} = -J_P^{-1}\begin{bmatrix}1\\0\\0\end{bmatrix}$$
$$\frac{\partial x_i}{\partial \omega_i} = tA_i\cos(\omega_i t + \varphi_i) = \frac{t}{\omega_i}\dot{x}_i \quad \text{(B.5)}$$
$$\frac{\partial \omega_i}{\partial \omega_{scs}} = k_i$$

A set of constants k_i have been retained from the frequency analysis of FOG data during a long duration pointing in SCM.

B.2 Dynamic Model Based Inertia Tensor Estimation Algorithm

The Planck spacecraft is modelled as a rigid body with a slowly varying inertia tensor. The equations of motion in the principal axis reference system are given as:-

$$\dot{\underline{\omega}}_P = J_P^{-1}(\nu_n, \Delta)(\underline{\tau}_P + [[\underline{\omega}_P]]J_P(\nu_n, \Delta)\underline{\omega}_P) = f_\omega(\underline{\omega}_P, \underline{\tau}_P, \nu_n, \Delta) \quad \text{(B.6)}$$

where:-

$\underline{\omega}_P = (\omega_1, \omega_2, \omega_3)$ true angular rate vector expressed in spacecraft principal axes

$\underline{\tau}_P = (\tau_1, \tau_2, \tau_3)$ true external torque vector expressed in spacecraft principal axes

$J_P = diag(J_1, J_2, J_3)$ is the principal axis inertia tensor which is a function of the nutation to spin rate ratio, ν_n, and the axial imbalance, Δ.

(B.6) can therefore also be written:-

$$\dot{\omega}_1 = J_1^{-1}(\tau_1 - \omega_2\omega_3(J_3 - J_2))$$
$$\dot{\omega}_2 = J_2^{-1}(\tau_2 - \omega_1\omega_3(J_1 - J_3)) \quad \text{(B.1)}$$
$$\dot{\omega}_3 = J_3^{-1}(\tau_3 - \omega_1\omega_2(J_2 - J_1))$$

The nutation to spin rate ratio is given by:-

$$\nu_n = \frac{\omega_n}{\omega_s} = \sqrt{\left(\frac{J_1}{J_2} - 1\right)\left(\frac{J_1}{J_3} - 1\right)} = \sqrt{\alpha_2\alpha_3} \quad \text{(B.2)}$$

and the axial imbalance, Δ, is a measure of the degree of asymmetry between the two spacecraft transverse principal moments of inertia and is defined as:-

$$\Delta = \frac{J_1}{J_3} - \frac{J_1}{J_2} = \alpha_3 - \alpha_2 \quad \text{(B.3)}$$

In the general case of a nutating asymmetric spacecraft, the spin rate will not be constant, whereby, ω_s, is the maximum spin rate. In the absence of nutation, the spin rate is constant.

The inertia ratios α_2 and α_3 in (B.2) and (B.3) are positive quantities and are defined as:-

$$\begin{aligned} \alpha_2 &= \frac{J_1}{J_2} - 1 \\ \alpha_3 &= \frac{J_1}{J_3} - 1 \end{aligned} \tag{B.4}$$

From (B.2) and (B.3), we obtain the following quadratic equation:-

$$\alpha_2^2 + \Delta\alpha_2 - \nu_n{}^2 = 0 \tag{B.5}$$

Solving (B.5) for α_2, where the root ensuring that α_2 is positive quantity will be taken.

$$\alpha_2 = -\frac{\Delta}{2} + \frac{1}{2}\sqrt{\Delta^2 + 4\nu_n{}^2} \tag{B.6}$$

Rearranging (B.3), it follows that α_3 can be obtained from:-

$$\alpha_3 = \Delta + \alpha_2 \tag{B.7}$$

Rearranging (B.4) and assuming that we know the spin axis principal moment of inertia, J_1, we can solve for the transverse principal moments of inertia as follows:-

$$\begin{aligned} J_2 &= \frac{J_1}{1+\alpha_2} = \frac{2J_1}{(2 - \Delta + \sqrt{(\Delta^2 + 4\nu_n^2)})} \\ J_3 &= \frac{J_1}{1+\alpha_3} = \frac{2J_1}{(2 + \Delta + \sqrt{(\Delta^2 + 4\nu_n^2)})} \end{aligned} \tag{B.8}$$

The axial imbalance is zero for an axial symmetric spacecraft, since the transverse principal moments of inertia are equal.

Linearising (B.6) yields:-

$$\dot{\underline{\omega}}_P = \dot{\hat{\underline{\omega}}}_P + \left(\frac{\partial f_\omega}{\partial \underline{\omega}_P}\right)\delta\underline{\omega}_P + \left(\frac{\partial f_\omega}{\partial \underline{\tau}_P}\right)\delta\underline{\tau}_P + \left(\frac{\partial f_\omega}{\partial \nu_n}\right)\delta\nu_n + \left(\frac{\partial f_\omega}{\partial \Delta}\right)\delta\Delta \tag{B.9}$$

where the partial derivatives are computed analytically as:-

$$\begin{aligned} \frac{\partial f_\omega}{\partial \underline{\omega}_P} &= J_P^{-1}(\nu_n, \Delta)([[\underline{\omega}_P]]J_P(\nu_n, \Delta) - [[J_P(\nu_n, \Delta)\underline{\omega}_P]]) \\ \frac{\partial f_\omega}{\partial \underline{\tau}_P} &= J_P^{-1}(\nu_n, \Delta) \end{aligned} \tag{B.10}$$

Also

$$\begin{aligned} \frac{\partial f_\omega}{\partial \nu_n} &= \left(\frac{\partial f_\omega}{\partial J_2}\right)\left(\frac{\partial J_2}{\partial \nu_n}\right) + \left(\frac{\partial f_\omega}{\partial J_3}\right)\left(\frac{\partial J_3}{\partial \nu_n}\right) \\ \frac{\partial f_\omega}{\partial \Delta} &= \left(\frac{\partial f_\omega}{\partial J_2}\right)\left(\frac{\partial J_2}{\partial \Delta}\right) + \left(\frac{\partial f_\omega}{\partial J_3}\right)\left(\frac{\partial J_3}{\partial \Delta}\right) \end{aligned} \tag{B.11}$$

where

$$\frac{\partial f_\omega}{\partial J_2} = \begin{bmatrix} J_1^{-1}\omega_2\omega_3 \\ -J_2^{-2}(\tau_2 - \omega_1\omega_3(J_1 - J_3)) \\ -J_3^{-1}\omega_1\omega_2 \end{bmatrix}$$
$$\frac{\partial f_\omega}{\partial J_3} = \begin{bmatrix} -J_1^{-1}\omega_2\omega_3 \\ J_2^{-1}\omega_1\omega_3 \\ -J_3^{-2}(\tau_3 - \omega_1\omega_2(J_2 - J_1)) \end{bmatrix} \tag{B.12}$$

and

$$\frac{\partial J_2}{\partial \nu_n} = \frac{-8J_1\nu_n}{(2 - \Delta + \sqrt{(\Delta^2 + 4\nu_n^2)})^2\sqrt{(\Delta^2 + 4\nu_n^2)}}$$
$$\frac{\partial J_3}{\partial \nu_n} = \frac{-8J_1\nu_n}{(2 + \Delta + \sqrt{(\Delta^2 + 4\nu_n^2)})^2\sqrt{(\Delta^2 + 4\nu_n^2)}}$$
$$\frac{\partial J_2}{\partial \Delta} = \frac{-2J_1(\Delta - \sqrt{(\Delta^2 + 4\nu_n^2)})}{(2 - \Delta + \sqrt{(\Delta^2 + 4\nu_n^2)})^2\sqrt{(\Delta^2 + 4\nu_n^2)}} \tag{B.13}$$
$$\frac{\partial J_3}{\partial \Delta} = \frac{-2J_1(\Delta + \sqrt{(\Delta^2 + 4\nu_n^2)})}{(2 + \Delta + \sqrt{(\Delta^2 + 4\nu_n^2)})^2\sqrt{(\Delta^2 + 4\nu_n^2)}}$$

Appendix C Batch Estimator Implementation

This appendix contains an overview of how the batch estimation algorithms have been implemented to filter the measured star tracker attitude quaternion on Planck spacecraft.

Appendix C.1 gives a general overview on how the estimators have been implemented. A flow chart shows exactly the steps and calculations performed.

Appendix C.2 presents the state transition matrices for the various batch estimation algorithms. For purposes of numerical efficiency and speed, the state transition matrices have been partitioned in order to exploit the sparse system dynamics matrix, thereby allowing significant reductions in the order of the matrix differential equations that must be solved using numerical integration. This is important mainly due to the high measurement frequency and hence the small integration step size required to propagate the reference state and the corresponding state transition matrices.

C.1 Generalities

The approach used to implement all batch estimation algorithms described in this article, follows the approach presented in Chapter 4 of [22]. The construction of the coefficient matrix and observation vector is different, which allows the use of numerically superior orthogonalisation methods for the least squares solution of the state vector [23] at a single state epoch, instead of using the method of normal equations.

In general, the dynamics are represented by the following set of non-linear differential equations:-

$$\frac{d\underline{X}}{dt} = \underline{f}(\underline{X}, t),\ \underline{X}(t_k) = \underline{X}_k \tag{C.1}$$

and the observations are represented by the following set of non-linear equations:-

$$\underline{Y}_i = \underline{h}(\underline{X}_i, t_i) + \underline{\varepsilon}_i,\ i = 1, \ldots, l \tag{C.2}$$

where $\underline{\varepsilon}_i$ are the measurement errors.

Given a reference state $\underline{X}^{ref}$ that follows reasonably close to the actual state vector $\underline{X}$, then it is possible to expand the actual state as a Taylor series about the reference state. With the state deviation vector and observation deviation vector defined as follows:-

$$\begin{aligned} \underline{x}(t) &= \underline{X}(t) - \underline{X}^{ref}(t) \\ \underline{y}_i(t) &= \underline{Y}_i(t) - \underline{Y}_i^{ref}(t) \end{aligned} \tag{C.3}$$

Then, assuming the following condition to be satisfied:-

$$\frac{d\underline{X}^{ref}}{dt} = \underline{f}(\underline{X}^{ref}, t),\ \underline{X}^{ref}(t_k) = \underline{X}_k^{ref} \tag{C.4}$$

and

$$\underline{Y}_i^{ref} = \underline{h}(\underline{X}_i^{ref}, t_i) + \underline{\varepsilon}_i,\ i = 1, \ldots, l \tag{C.5}$$

where (C.4) is used to propagate the reference state trajectory throughout the selected batch interval and (C.5) is used to compute the predicted measurements.

Also neglecting terms higher than first order in the Taylor series expansion, then the linearised system dynamics can be found as:-

$$\frac{d\underline{x}}{dt} = F(t)\underline{x}(t) \tag{C.6}$$

where

$$F(t) = \left[\frac{\partial \underline{f}}{\partial \underline{x}(t)}\right]_{\underline{X} = \underline{X}^{ref}} \tag{C.7}$$

and the linearised observation equation for the i^{th} observation can be found as:-

$$\underline{y}_i = \tilde{H}_i \underline{x}_i + \underline{\varepsilon}_i \tag{C.8}$$

where

$$\tilde{H}_i = \left[\frac{\partial \underline{h}}{\partial \underline{x}(t_i)}\right]_{\underline{X}_i = \underline{X}_i^{ref}} \tag{C.9}$$

Now (C.6) is a system of first order linear differential equations with time dependant coefficients. The general solution of this system of equations can be expressed as follows:-

$$\underline{x}(t) = \Phi(t, t_k)\underline{x}_k \tag{C.10}$$

where $\Phi(t, t_k)$ is the state transition matrix, which satisfies the following matrix differential equation:-

$$\frac{d}{dt}\Phi(t, t_k) = F(t)\Phi(t, t_k) \tag{C.11}$$

where (C.11) is used to propagate the elements of the state transition matrix throughout the selected batch interval.

The state transition matrix can therefore be used to reference the measurements back or forward to some arbitrary reference epoch t_k, using (C.8) as:-

$$\underline{y}_i = \tilde{H}_i \underline{x}_i + \underline{\varepsilon}_i = \tilde{H}_i \Phi(t, t_k)\underline{x}_k + \underline{\varepsilon}_i \tag{C.12}$$

A flow chart implementation of the batch processing algorithm, taken from Figure 4.6.1 of [22] with slight additions, is shown in Figure C.1:

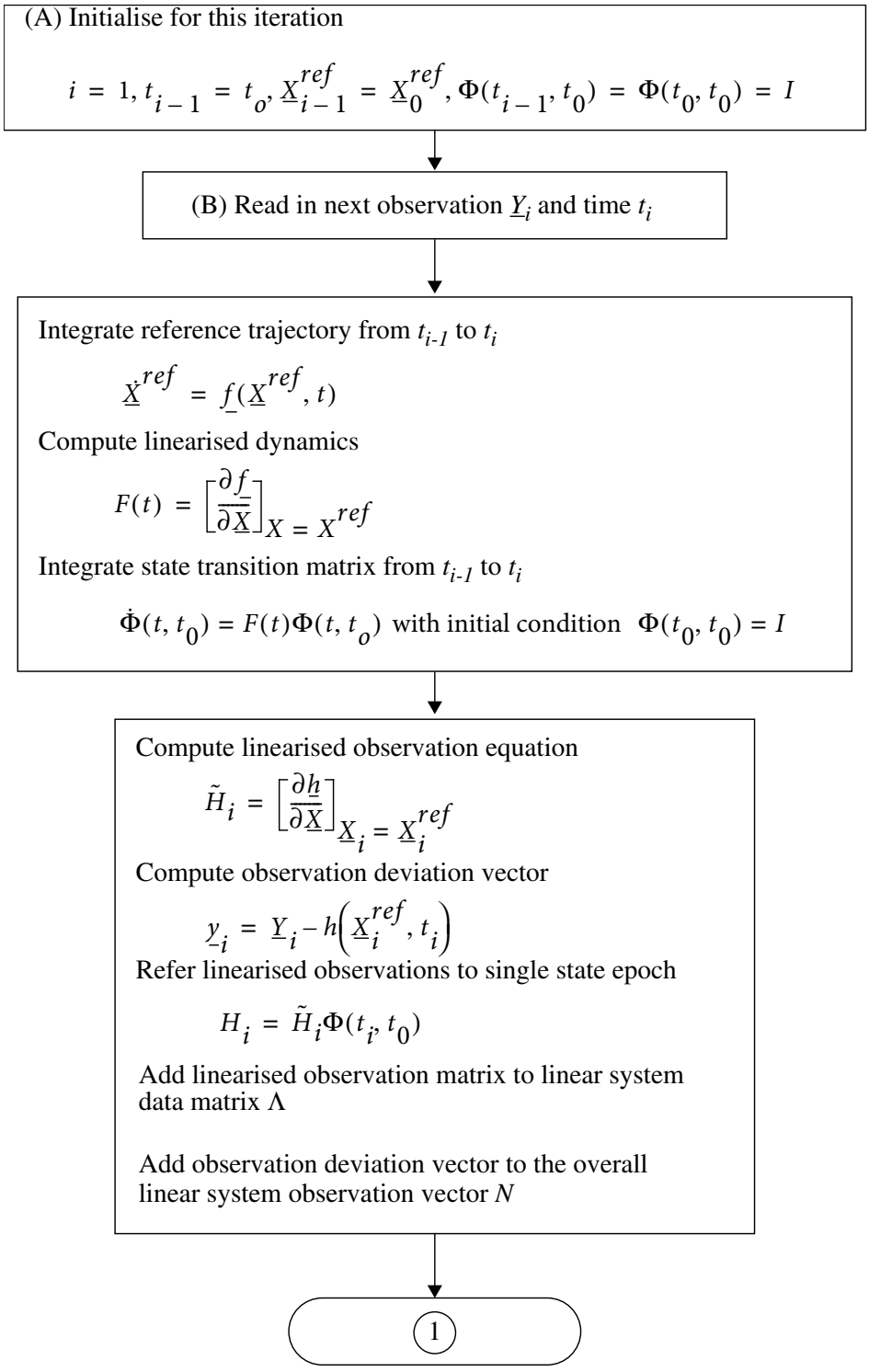

Figure C.1: Batch Estimation Algorithm Implementation

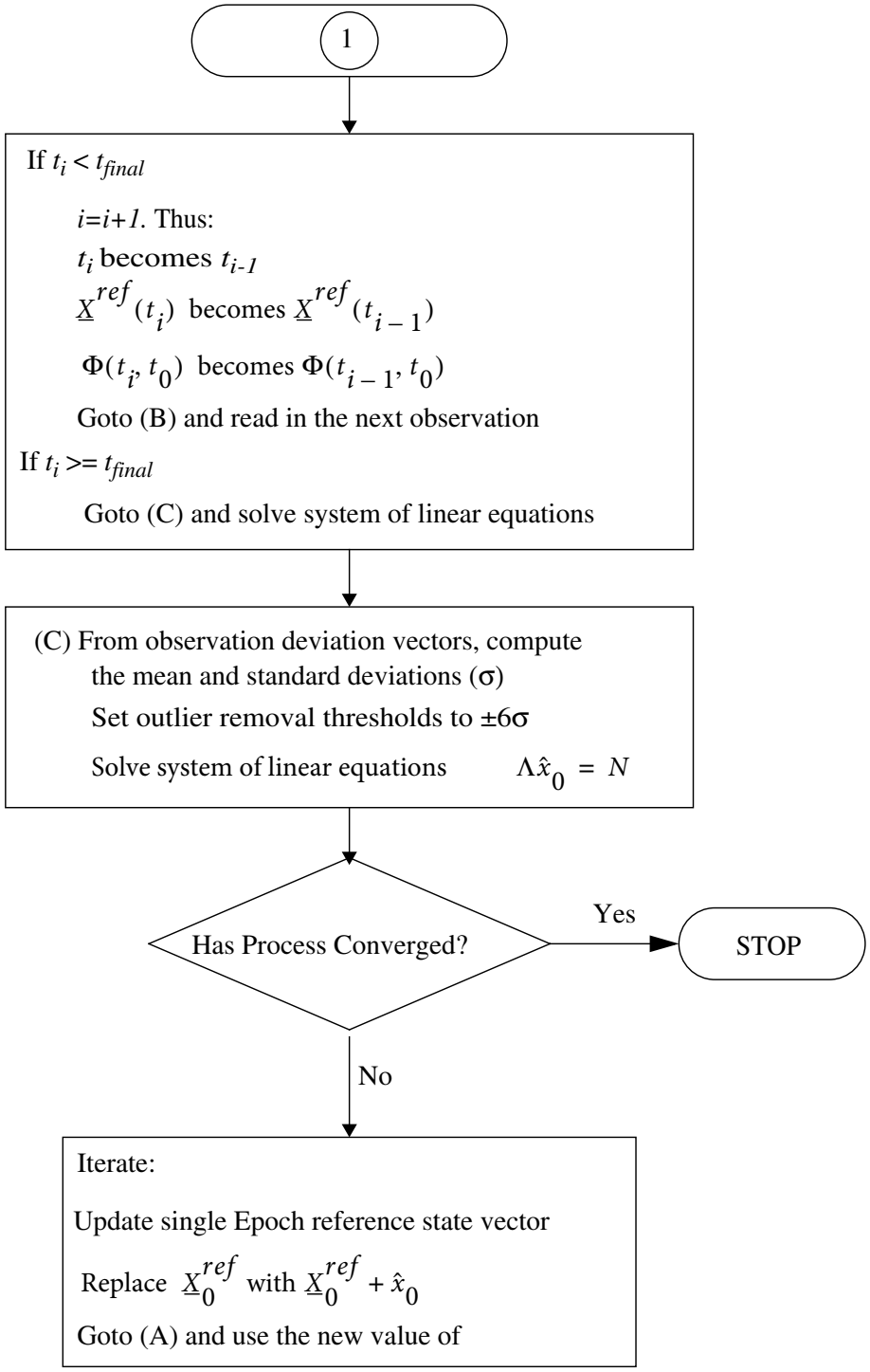

Figure C.1: Batch Estimation Algorithm Implementation

C.2 State Transition Matrix Structure

For the estimation problems formulated in this article, the sparse structure of the system dynamics matrix, $F(t)$, given in (C.6) and (C.7), allows partitioning of the state transition matrix. This partitioning results in a significant reduction in the number of differential equations, that require numerical integration over the selected batch interval. This structure exploitation is recommended in Section 4.2.2 of [22]. The structure of the state transition matrix and the sub-matrix differential equations, that require numerical integration, are presented for the

various estimators in the following sections of this Annex.

C.2.1 STR-FOG based Filter

The system dynamics matrix for this estimator is given by (7) and (8). The state transition matrix for this estimator is therefore given as:-

$$\Phi = \begin{bmatrix} \Phi_{11} & \Phi_{12} & \Phi_{13} \\ 0_{3\times 3} & I_3 & \Phi_{23} \\ 0_{3\times 3} & 0_{3\times 3} & I_3 \end{bmatrix} \tag{C.13}$$

and submatrix differential equations to be numerically integrated are given as follows:-

$$\begin{aligned} \dot{\Phi}_{11} &= F_A\Phi_{11} + F_B\Phi_{21} \qquad \dot{\Phi}_{23} = I_3 \\ \dot{\Phi}_{12} &= F_A\Phi_{12} + F_B\Phi_{22} \\ \dot{\Phi}_{13} &= F_A\Phi_{13} + F_B\Phi_{23} \end{aligned} \tag{C.14}$$

The number of differential equations to be numerically integrated is therefore reduced from 81 to 36, as a result of the partitioning. The partitions of the system dynamics matrix, (F_A, F_B), are defined in (8).

C.2.2 STR-Dynamic Model based Filter (HCM)

The system dynamics matrix for this estimator is given by (16), (18) and (19). The state transition matrix for this estimator is therefore given as:-

$$\Phi = \begin{bmatrix} \Phi_{11} & \Phi_{12} & \Phi_{13} & \Phi_{14} & \Phi_{15} & \Phi_{16} & \Phi_{17} & \Phi_{18} & \Phi_{19} \\ \Phi_{21} & \Phi_{22} & \Phi_{23} & \Phi_{24} & \Phi_{25} & \Phi_{26} & \Phi_{27} & \Phi_{28} & \Phi_{29} \\ 0_{3\times 3} & 0_{3\times 3} & I_3 & 0_{3\times 3} & 0_{3\times 3} & 0_{3\times 3} & 0_{3\times 3} & 0_{3\times 3} & 0_{3\times 3} \\ 0_{3\times 3} & 0_{3\times 3} & 0_{3\times 3} & I_3 & 0_{3\times 3} & 0_{3\times 3} & 0_{3\times 3} & 0_{3\times 3} & 0_{3\times 3} \\ 0_{3\times 3} & 0_{3\times 3} & 0_{3\times 3} & 0_{3\times 3} & I_3 & 0_{3\times 3} & 0_{3\times 3} & 0_{3\times 3} & 0_{3\times 3} \\ 0_{3\times 3} & 0_{3\times 3} & 0_{3\times 3} & 0_{3\times 3} & 0_{3\times 3} & I_3 & 0_{3\times 3} & 0_{3\times 3} & 0_{3\times 3} \\ 0_{3\times 3} & 0_{3\times 3} & 0_{3\times 3} & 0_{3\times 3} & 0_{3\times 3} & 0_{3\times 3} & I_3 & 0_{3\times 3} & 0_{3\times 3} \\ 0_{3\times 3} & 0_{3\times 3} & 0_{3\times 3} & 0_{3\times 3} & 0_{3\times 3} & 0_{3\times 3} & 0_{3\times 3} & I_3 & 0_{3\times 3} \\ 0_{3\times 3} & 0_{3\times 3} & 0_{3\times 3} & 0_{3\times 3} & 0_{3\times 3} & 0_{3\times 3} & 0_{3\times 3} & 0_{3\times 3} & I_3 \end{bmatrix} \tag{C.15}$$

and the submatrix differential equations to be numerically integrated are given as follows:-

$$
\begin{aligned}
\dot{\Phi}_{11} &= F_A\Phi_{11} + F_B\Phi_{21} & \dot{\Phi}_{21} &= F_C\Phi_{21} \\
\dot{\Phi}_{12} &= F_A\Phi_{12} + F_B\Phi_{22} & \dot{\Phi}_{22} &= F_C\Phi_{22} \\
\dot{\Phi}_{13} &= F_A\Phi_{13} + F_B\Phi_{23} & \dot{\Phi}_{23} &= F_C\Phi_{23} + F_1 \\
\dot{\Phi}_{14} &= F_A\Phi_{14} + F_B\Phi_{24} & \dot{\Phi}_{24} &= F_C\Phi_{24} + F_2 \\
\dot{\Phi}_{15} &= F_A\Phi_{15} + F_B\Phi_{25} & \dot{\Phi}_{25} &= F_C\Phi_{25} + F_3 \\
\dot{\Phi}_{16} &= F_A\Phi_{16} + F_B\Phi_{26} & \dot{\Phi}_{26} &= F_C\Phi_{26} + F_4 \\
\dot{\Phi}_{17} &= F_A\Phi_{17} + F_B\Phi_{27} & \dot{\Phi}_{27} &= F_C\Phi_{27} + F_5 \\
\dot{\Phi}_{18} &= F_A\Phi_{18} + F_B\Phi_{28} & \dot{\Phi}_{28} &= F_C\Phi_{28} + F_6 \\
\dot{\Phi}_{19} &= F_A\Phi_{19} + F_B\Phi_{29} & \dot{\Phi}_{29} &= F_C\Phi_{29} + F_7
\end{aligned}
\tag{C.16}
$$

The partitions of the system dynamics matrix, (F_A, F_B, F_C), are defined in (19) and the matrices F_i are defined according to the HCM nominal slew timeline, as given in Figure 1 and the logic in (16). The number of differential equations to be numerically integrated is reduced from 729 to 162, as a result of the partitioning.

C.2.3 STR-Dynamic Model based Filter (SCM)

The system dynamics matrix for this estimator is given by (26) and (27). The state transition matrix for this estimator is therefore given as:-

$$
\Phi = \begin{bmatrix}
\Phi_{11} & \Phi_{12} & \Phi_{13} & \Phi_{14} & \Phi_{15} & \Phi_{16} & \Phi_{17} & \Phi_{18} & \Phi_{19} & \Phi_{1A} & \Phi_{1B} & \Phi_{1C} & \Phi_{1D} & \Phi_{1E} & \Phi_{1F} & \Phi_{1G} \\
\Phi_{21} & \Phi_{22} & \Phi_{23} & \Phi_{24} & \Phi_{25} & \Phi_{26} & \Phi_{27} & \Phi_{28} & \Phi_{29} & \Phi_{2A} & \Phi_{2B} & \Phi_{2C} & \Phi_{2D} & \Phi_{2E} & \Phi_{2F} & \Phi_{2G} \\
\Phi_{31} & \Phi_{32} & \Phi_{33} & \Phi_{34} & \Phi_{35} & \Phi_{36} & \Phi_{37} & \Phi_{38} & \Phi_{39} & \Phi_{3A} & \Phi_{3B} & \Phi_{3C} & \Phi_{3D} & \Phi_{3E} & \Phi_{3F} & \Phi_{3G} \\
0_{2\times3} & 0_{2\times3} & 0_{2\times3} & I_2 & \Phi_{45} & 0_{2\times1} & 0_{2\times1} & 0_{2\times1} & 0_{2\times1} & 0_{2\times1} & 0_{2\times1} & 0_{2\times1} & 0_{2\times1} & 0_{2\times1} & 0_{2\times1} & 0_{2\times1} \\
0_{2\times3} & 0_{2\times3} & 0_{2\times3} & 0_{2\times2} & I_2 & 0_{2\times1} & 0_{2\times1} & 0_{2\times1} & 0_{2\times1} & 0_{2\times1} & 0_{2\times1} & 0_{2\times1} & 0_{2\times1} & 0_{2\times1} & 0_{2\times1} & 0_{2\times1} \\
0 & 0 & 0 & 0 & 0 & \Phi_{66} & \Phi_{67} & 0 & 0 & 0 & 0 & 0 & 0 & 0 & 0 & \Phi_{6G} \\
0 & 0 & 0 & 0 & 0 & \Phi_{76} & \Phi_{77} & 0 & 0 & 0 & 0 & 0 & 0 & 0 & 0 & \Phi_{7G} \\
0 & 0 & 0 & 0 & 0 & 0 & 0 & \Phi_{88} & \Phi_{89} & 0 & 0 & 0 & 0 & 0 & 0 & \Phi_{8G} \\
0 & 0 & 0 & 0 & 0 & 0 & 0 & \Phi_{98} & \Phi_{99} & 0 & 0 & 0 & 0 & 0 & 0 & \Phi_{9G} \\
0 & 0 & 0 & 0 & 0 & 0 & 0 & 0 & 0 & \Phi_{AA} & \Phi_{AB} & 0 & 0 & 0 & 0 & \Phi_{AG} \\
0 & 0 & 0 & 0 & 0 & 0 & 0 & 0 & 0 & \Phi_{BA} & \Phi_{BB} & 0 & 0 & 0 & 0 & \Phi_{BG} \\
0 & 0 & 0 & 0 & 0 & 0 & 0 & 0 & 0 & 0 & 0 & \Phi_{CC} & \Phi_{CD} & 0 & 0 & \Phi_{CG} \\
0 & 0 & 0 & 0 & 0 & 0 & 0 & 0 & 0 & 0 & 0 & \Phi_{DC} & \Phi_{DD} & 0 & 0 & \Phi_{DG} \\
0 & 0 & 0 & 0 & 0 & 0 & 0 & 0 & 0 & 0 & 0 & 0 & 0 & \Phi_{EE} & \Phi_{EF} & \Phi_{EG} \\
0 & 0 & 0 & 0 & 0 & 0 & 0 & 0 & 0 & 0 & 0 & 0 & 0 & \Phi_{FE} & \Phi_{FF} & \Phi_{FG} \\
0 & 0 & 0 & 0 & 0 & 0 & 0 & 0 & 0 & 0 & 0 & 0 & 0 & 0 & 0 & 1
\end{bmatrix}
\tag{C.17}
$$

and the submatrix differential equations to be numerically integrated are given as follows:-

$$
\begin{aligned}
\dot{\Phi}_{11} &= F_A\Phi_{11} + F_B\Phi_{21} \\
\dot{\Phi}_{12} &= F_A\Phi_{12} + F_B\Phi_{22} \\
\dot{\Phi}_{13} &= F_A\Phi_{13} + F_B\Phi_{23} \\
\dot{\Phi}_{14} &= F_A\Phi_{14} + F_B\Phi_{24} + F_C \\
\dot{\Phi}_{15} &= F_A\Phi_{15} + F_B\Phi_{25} + F_C\Phi_{45} \\
\dot{\Phi}_{16} &= F_A\Phi_{16} + F_B\Phi_{26} \\
\dot{\Phi}_{17} &= F_A\Phi_{17} + F_B\Phi_{27} \\
\dot{\Phi}_{18} &= F_A\Phi_{18} + F_B\Phi_{28} \\
\dot{\Phi}_{19} &= F_A\Phi_{19} + F_B\Phi_{29} \\
\dot{\Phi}_{1A} &= F_A\Phi_{1A} + F_B\Phi_{2A} \\
\dot{\Phi}_{1B} &= F_A\Phi_{1B} + F_B\Phi_{2B} \\
\dot{\Phi}_{1C} &= F_A\Phi_{1C} + F_B\Phi_{2C} \\
\dot{\Phi}_{1D} &= F_A\Phi_{1D} + F_B\Phi_{2D} \\
\dot{\Phi}_{1E} &= F_A\Phi_{1E} + F_B\Phi_{2E} \\
\dot{\Phi}_{1F} &= F_A\Phi_{1F} + F_B\Phi_{2F} \\
\dot{\Phi}_{1G} &= F_A\Phi_{1G} + F_B\Phi_{2G}
\end{aligned}
\qquad
\begin{aligned}
\dot{\Phi}_{21} &= F_D\Phi_{21} + F_E\Phi_{31} \\
\dot{\Phi}_{22} &= F_D\Phi_{22} + F_E\Phi_{32} \\
\dot{\Phi}_{23} &= F_D\Phi_{23} + F_E\Phi_{33} \\
\dot{\Phi}_{24} &= F_D\Phi_{24} + F_E\Phi_{34} \\
\dot{\Phi}_{25} &= F_D\Phi_{25} + F_E\Phi_{35} \\
\dot{\Phi}_{26} &= F_D\Phi_{26} + F_E\Phi_{36} + F_F\Phi_{66} \\
\dot{\Phi}_{27} &= F_D\Phi_{27} + F_E\Phi_{37} + F_F\Phi_{67} \\
\dot{\Phi}_{28} &= F_D\Phi_{28} + F_E\Phi_{38} + F_F\Phi_{88} \\
\dot{\Phi}_{29} &= F_D\Phi_{29} + F_E\Phi_{39} + F_F\Phi_{89} \\
\dot{\Phi}_{2A} &= F_D\Phi_{2A} + F_E\Phi_{3A} + F_F\Phi_{AA} \\
\dot{\Phi}_{2B} &= F_D\Phi_{2B} + F_E\Phi_{3B} + F_F\Phi_{AB} \\
\dot{\Phi}_{2C} &= F_D\Phi_{2C} + F_E\Phi_{3C} + F_F\Phi_{CC} \\
\dot{\Phi}_{2D} &= F_D\Phi_{2D} + F_E\Phi_{3D} + F_F\Phi_{CD} \\
\dot{\Phi}_{2E} &= F_D\Phi_{2E} + F_E\Phi_{3E} + F_F\Phi_{EE} \\
\dot{\Phi}_{2F} &= F_D\Phi_{2F} + F_E\Phi_{3F} + F_F\Phi_{EF} \\
\dot{\Phi}_{2G} &= F_D\Phi_{2G} + F_E\Phi_{3G} + F_I \\
&\quad + F_F(\Phi_{6G} + \Phi_{8G} + \Phi_{AG} + \Phi_{CG} + \Phi_{EG})
\end{aligned}
$$

$$
\begin{aligned}
\dot{\Phi}_{31} &= F_J\Phi_{21} + F_K\Phi_{31} \\
\dot{\Phi}_{32} &= F_J\Phi_{22} + F_K\Phi_{32} \\
\dot{\Phi}_{33} &= F_J\Phi_{23} + F_K\Phi_{33} \\
\dot{\Phi}_{34} &= F_J\Phi_{24} + F_K\Phi_{34} \\
\dot{\Phi}_{35} &= F_J\Phi_{25} + F_K\Phi_{35} \\
\dot{\Phi}_{36} &= F_J\Phi_{26} + F_K\Phi_{36} \\
\dot{\Phi}_{37} &= F_J\Phi_{27} + F_K\Phi_{37} \\
\dot{\Phi}_{38} &= F_J\Phi_{28} + F_K\Phi_{38} \\
\dot{\Phi}_{39} &= F_J\Phi_{29} + F_K\Phi_{39} \\
\dot{\Phi}_{3A} &= F_J\Phi_{2A} + F_K\Phi_{3A} \\
\dot{\Phi}_{3B} &= F_J\Phi_{2B} + F_K\Phi_{3B} \\
\dot{\Phi}_{3C} &= F_J\Phi_{2C} + F_K\Phi_{3C} \\
\dot{\Phi}_{3D} &= F_J\Phi_{2D} + F_K\Phi_{3D} \\
\dot{\Phi}_{3E} &= F_J\Phi_{2E} + F_K\Phi_{3E} \\
\dot{\Phi}_{3F} &= F_J\Phi_{2F} + F_K\Phi_{3F} \\
\dot{\Phi}_{3G} &= F_J\Phi_{2G} + F_K\Phi_{3G}
\end{aligned}
\qquad
\begin{aligned}
\dot{\Phi}_{66} &= \Phi_{76} \qquad \dot{\Phi}_{76} = F_L\Phi_{66} \\
\dot{\Phi}_{67} &= \Phi_{77} \qquad \dot{\Phi}_{77} = F_L\Phi_{67} \\
\dot{\Phi}_{88} &= \Phi_{98} \qquad \dot{\Phi}_{98} = F_N\Phi_{88} \\
\dot{\Phi}_{89} &= \Phi_{99} \qquad \dot{\Phi}_{99} = F_N\Phi_{89} \\
\dot{\Phi}_{AA} &= \Phi_{BA} \qquad \dot{\Phi}_{BA} = F_P\Phi_{AA} \\
\dot{\Phi}_{AB} &= \Phi_{BB} \qquad \dot{\Phi}_{BB} = F_P\Phi_{AB} \\
\dot{\Phi}_{CC} &= \Phi_{DC} \qquad \dot{\Phi}_{DC} = F_R\Phi_{2G} \\
\dot{\Phi}_{CD} &= \Phi_{DD} \qquad \dot{\Phi}_{DD} = F_R\Phi_{2G} \\
\dot{\Phi}_{EE} &= \Phi_{FE} \qquad \dot{\Phi}_{FE} = F_T\Phi_{EE} \\
\dot{\Phi}_{EF} &= \Phi_{FF} \qquad \dot{\Phi}_{FF} = F_T\Phi_{EF}
\end{aligned}
\tag{C.18}
$$

The partitions of the system dynamics matrix,

$$(F_A, F_B, F_C, F_D, F_E, F_F, F_I, F_J, F_K, F_L, F_M, F_N, F_O, F_P, F_Q, F_R, F_S, F_T, F_U)$$

are defined in (27). The number of differential equations to be numerically integrated is reduced from 576 to 246,

as a result of the partitioning.

C.2.4 Dynamic Model Based Inertia Tensor Estimation Algorithm

The system dynamics matrix for this estimator is given by (33) and (34). The state transition matrix for this estimator is therefore given as:-

$$\Phi = \begin{bmatrix} \Phi_{11} & \Phi_{12} & \Phi_{13} & \Phi_{14} & \Phi_{15} & \Phi_{16} & \Phi_{17} & \Phi_{18} & \Phi_{19} \\ \Phi_{21} & \Phi_{22} & \Phi_{23} & \Phi_{24} & \Phi_{25} & \Phi_{26} & \Phi_{27} & \Phi_{28} & \Phi_{29} \\ \Phi_{31} & \Phi_{32} & \Phi_{33} & \Phi_{34} & \Phi_{35} & \Phi_{36} & \Phi_{37} & \Phi_{38} & \Phi_{39} \\ 0_{2\times3} & 0_{2\times3} & 0_{2\times3} & I_2 & \Phi_{45} & 0_{2\times1} & 0_{2\times1} & 0_{2\times1} & 0_{2\times1} \\ 0_{2\times3} & 0_{2\times3} & 0_{2\times3} & 0_{2\times2} & I_2 & 0_{2\times1} & 0_{2\times1} & 0_{2\times1} & 0_{2\times1} \\ 0_{1\times3} & 0_{1\times3} & 0_{1\times3} & 0_{1\times2} & 0_{1\times2} & 1 & \Phi_{67} & 0 & 0 \\ 0_{1\times3} & 0_{1\times3} & 0_{1\times3} & 0_{1\times2} & 0_{1\times2} & 0 & 1 & 0 & 0 \\ 0_{1\times3} & 0_{1\times3} & 0_{1\times3} & 0_{1\times2} & 0_{1\times2} & 0 & 0 & 1 & 0 \\ 0_{1\times3} & 0_{1\times3} & 0_{1\times3} & 0_{1\times2} & 0_{1\times2} & 0 & 0 & 0 & 1 \end{bmatrix} \tag{C.19}$$

and the submatrix differential equations to be numerically integrated are given as follows:-

$$\begin{aligned}
\dot{\Phi}_{11} &= F_A\Phi_{11} + F_B\Phi_{21} & \dot{\Phi}_{21} &= F_E\Phi_{21} + F_F\Phi_{31} \\
\dot{\Phi}_{12} &= F_A\Phi_{12} + F_B\Phi_{22} & \dot{\Phi}_{22} &= F_E\Phi_{22} + F_F\Phi_{32} \\
\dot{\Phi}_{13} &= F_A\Phi_{13} + F_B\Phi_{23} & \dot{\Phi}_{23} &= F_E\Phi_{23} + F_F\Phi_{33} \\
\dot{\Phi}_{14} &= F_A\Phi_{14} + F_B\Phi_{24} + F_C & \dot{\Phi}_{24} &= F_E\Phi_{24} + F_F\Phi_{34} \\
\dot{\Phi}_{15} &= F_A\Phi_{15} + F_B\Phi_{25} + F_C\Phi_{45} & \dot{\Phi}_{25} &= F_E\Phi_{25} + F_F\Phi_{35} \\
\dot{\Phi}_{16} &= F_A\Phi_{16} + F_B\Phi_{26} & \dot{\Phi}_{26} &= F_E\Phi_{26} + F_F\Phi_{36} + F_G \\
\dot{\Phi}_{17} &= F_A\Phi_{17} + F_B\Phi_{27} & \dot{\Phi}_{27} &= F_E\Phi_{27} + F_F\Phi_{37} + F_G\Phi_{67} \\
\dot{\Phi}_{18} &= F_A\Phi_{18} + F_B\Phi_{28} & \dot{\Phi}_{28} &= F_E\Phi_{28} + F_F\Phi_{38} + F_H \\
\dot{\Phi}_{19} &= F_A\Phi_{19} + F_B\Phi_{29} + F_D & \dot{\Phi}_{29} &= F_E\Phi_{29} + F_F\Phi_{39}
\end{aligned}$$

$$\begin{aligned}
\dot{\Phi}_{31} &= F_I\Phi_{21} + F_J\Phi_{31} & & \\
\dot{\Phi}_{32} &= F_I\Phi_{22} + F_J\Phi_{32} & \dot{\Phi}_{38} &= F_I\Phi_{28} + F_J\Phi_{38} \\
\dot{\Phi}_{33} &= F_I\Phi_{23} + F_J\Phi_{33} & \dot{\Phi}_{39} &= F_I\Phi_{29} + F_J\Phi_{29} \\
\dot{\Phi}_{34} &= F_I\Phi_{24} + F_J\Phi_{34} & \dot{\Phi}_{45} &= I_2 \\
\dot{\Phi}_{35} &= F_I\Phi_{25} + F_J\Phi_{35} & \dot{\Phi}_{67} &= 1 \\
\dot{\Phi}_{36} &= F_I\Phi_{26} + F_J\Phi_{36} & & \\
\dot{\Phi}_{37} &= F_I\Phi_{27} + F_J\Phi_{37} & &
\end{aligned} \tag{C.20}$$

The partitions of the system dynamics matrix, $(F_A, F_B, F_C, F_D, F_E, F_F, F_G, F_H, F_I, F_J)$, are defined in (34).

The number of differential equations to be numerically integrated is reduced from 289 to 158, as a result of the partitioning.

Appendix D Glossary of Terms

ACA:	Planck Attitude Control Axes
ACC:	Attitude Control Computer
ACMS:	Attitude Control and Measurement System
AHF:	Attitude History File
ALOS:	About Line Of Sight of the STR
AME:	Absolute Measurement Error
APF:	Attitude Parameter File
APPL:	Augmented Programmed Pointing List file
ASW:	ACC Application Software
BSW:	ACC Basic Software
CPV:	Commissioning and Performance Verification Phase
DCM:	Direction Cosine Matrix
DFT:	Discrete Fourier Transform
DPU:	HFI Data Processing Unit
DTCP:	Daily Telecommunications Contact Period
ESOC:	European Space Operations Centre
FD:	Flight Dynamics
FDDB:	Flight Dynamics Database
FOG:	Fibre Optic Gyro
FOV:	Field Of View
HCM:	Planck Angular Momentum Control Mode
HPTDG:	Planck High Precision Test Data Generator developed by FD TVA
ICD:	Interface Control Document
LOS:	Line Of Sight of the STR
LSQ:	Least Squares
LUT:	Look-Up Table
OBDB:	ACC On-board Database
OCM:	Planck Orbit Control Mode
OD:	Operational Day (counted from launch L=2009-05-14T13:12Z)
PSD:	Power Spectral Density
REBA:	Radiometer Electronics Box Assembly
SCM:	Planck Science Mode
SCE:	Sorption Cooler Electronics
SCS:	Sorption Cooler Sub-system
STR:	Star Tracker
TV:	Test and Validation section of the Flight Dynamics division
TVA:	Test and Validation (Attitude)

References

[1] M.D. Shuster, A Survey of Attitude Representations, Journal of Astronautical Sciences, Vol. 41, No. 4, pp. 439-517, 1993.

[2] U. Feucht, G. Gienger, Launch and early operations of Herschel and Planck. Acta Astronautica 68, pp. 1283-1291, doi:10.1016/j.actaastro.2010.09.003

[3] Planck Collaboration, Planck early results. I. The Planck mission, A&A 536, A1 (2011), doi: 10.1051/0004-6361/201116464

[4] Planck operations www.esa.int/esaMI/Operations/SEM45HZTIVE_0.html [retrieved 2011-12-14].

[5] A. Zacchei et al., Planck early results. V. The Low Frequency Instrument Data Processing, A&A 536, A5 (2011), doi: 10.1051/0004-6361/201116484

[6] Planck HFI Core Team et al., Planck early results. VI. The High Frequency Instrument Data Processing, A&A 536, A6 (2011), doi: 10.1051/0004-6361/201116462

[7] L. Tarabini, T. Prieto Llanos, J.S. Llorente, Planck Attitude Determination Algorithms, Proceedings of the 6th International ESA Conference on Guidance, Navigation and Control Systems, Loutraki, Greece, 17-20 October 2005, ESA SP-606, 2006.

[8] J. S. Llorente et al., Planck Attitude Determination Algorithms Description, H-P-4-SEN-TN-0002, Issue 2.3, 2006.

[9] D. Zorita, A. Agenjo, S. Llorente, G. Chlewicki, A. Cocito, P. Rideau, S. Thuerey, C. Watson, A. McDonald, M. Mück, J. de Bruin, How Planck AOCS behaved: Commissioning Early Orbit and Pointing Manoeuvres, Proceeding of 8th International ESA Conference on Guidance and Navigation Control Systems, Karlovy Vary, 6.-10.6.2011.

[10] G. Hinshaw et al., First Year Wilkinson Microwave Anisotropy Probe (WMAP) Observations: Data Processing Methods and Systematic Error Limits, Astrophys. J. Suppl. Series 148:63-95, 2003.

[11] L. Tucci et. al., Applications of a High-Precision Emulation Tool in Support of the Herschel Mission at ESOC Flight Dynamics, 21st International Symposium on Space Flight Dynamics, Toulouse, France, 2009.

[12] M. J.Tuttlebee, Planck Attitude History File Interface Control Document, PT-PMOC-FD-ICD-2110-OPS-GFT, Issue 2.6, 2009.

[13] D. Zorita, A. Agenjo-Diaz, Herschel/Planck ACMS User Manual Flight Control Procedures for the Planck Spacecraft, H-P-4-SEN-MA-001, Issue 4, 2009.

[14] M.J.Tuttlebee, Planck - Calibration of the Fibre Optic Gyro package with respect to the Star Tracker, PT-PMOC-FD-TN-2722-OPS-GFE, Issue 2.0, 2010.

[15] E. Lefferts et al., Kalman Filtering for Spacecraft Attitude Estimation, J. Guidance and Control, Vol. 5, No. 5, pp. 417-429, 1982.

[16] Dutch Space design team, D. Zorita., Herschel-Planck ACMS Design Report, H-P-4-DS-TN-011, Issue 6.1, 31.07.2007.

[17] LFI - Project System Team, Sorption Cooler System User Manual, PL-LFI-PST-MA-002, Issue 3.0, 2009.

[18] M. Oort, A. Agenjo-Diaz, ACMS Simulator Model Specification, H-P-4-DS-SP-0024, Issue 2 Rev. 5, 2006.

[19] M.J. Haye, ACMS Model Design and Interfaces, H-P-4-DS-DD-003, Issue 1 Rev. 6, 2007.

[20] J. R. Wertz (ed.), Spacecraft Attitude Determination and Control, D. Reidel Publishing Company, ISBN 90-277-0959-9, 1978.

[21] A. Bacchetta, G. Chlewicki, D. Oddenino, Attitude Control and Measurement Subsystem Requirements Specification, H-P-SP-AI-0011, Issue 06, 2005.

[22] B. D. Tapley et. al., Statistical Orbit Determination, Elsevier Academic Press, ISBN 0-12-683630-2, 2004.

[23] G. H. Golub and C. F. Van Loan, Matrix Computations, John Hopkins University Press, 3rd Edition, ISBN 0-8018-5413-X,1996.